RES

DOE/ER-0046/25

Damage Analysis and Fundamental Studies

Quarterly Progress Report
January-March 1986

May 1986

U.S. Department of Energy
Office of Energy Research
Office of Fusion Energy
Washington, DC 20545

B&R No. AT-15-02-03-04

Hanford Engineering Development Laboratory

Operated by
Westinghouse
Hanford Company
for the U.S. DOE

A Subsidiary of
Westinghouse Electric
Corporation

Contract No.
DE-AC06-76FF02170

P.O. Box 1970
Richland, WA 99352

DISCLAIMER

Printed in the United States of America
Available from
U.S. Department of Commerce
National Technical Information Service
5285 Port Royal Road
Springfield, VA 22161

NTIS price codes
Printed copy: A 07
Microfiched copy: A01

DOE/ER-0046/25
UC-20-20c

Damage Analysis and Fundamental Studies

Quarterly Progress Report
January-March 1986

May 1986

U.S. Department of Energy
Office of Energy Research
Office of Fusion Energy
Washington, DC 20545

B&R NO. AT-1502-03-04

FOREWORD

This report is the thirty-third in a series of Quarterly Technical Progress Reports on *Damage Analysis and Fundamental studies* (DAFS), which is one element of the Fusion Reactor Materials Program, conducted in support of the Magnetic Fusion Energy Program of the U.S. Department of Energy (DOE). The first eight reports in this series were numbered DOE/ET-0065/1 through 8. Other elements of the Fusion Materials Program are:

- Alloy Development for Irradiation Performance (ADIP)
- Plasma-Materials Interaction (PMI)
- Special Purpose Materials (SPM).

The DAFS program element is a national effort composed of contributions from a number of National Laboratories and other government laboratories, universities, and industrial laboratories. It was organized by the Materials and Radiation Effects Branch, DOE/Office of Fusion Energy, and a Task Group on *Damage Analysis and Fundamental Studies.* which operates under the auspices of that branch. The purpose of this series of reports is to provide a working technical record of that effort for the use of the program participants, the fusion energy program in general, and the DOE.

This report is organized along topical lines in parallel to a Program Plan of the same title so that activities and accomplishments may be followed readily, relative to that Program Plan. Thus, the work of a given laboratory may appear throughout the report. A chapter has been added on Reduced Activation Materials to accommodate work on a topic not included in the early program plan. The Contents is annotated for the convenience of the reader.

This report has been compiled and edited by N. E. Kenny under the guidance of the Chairman of the Task Group on *Damage Analysis and Fundamental studies,* D. G. Doran, Hanford Engineering Development Laboratory (HEDL). Their efforts, those of the supporting staff of HEDL, and the many persons who made technical contributions are gratefully acknowledged. T. C. Reuther, Fusion Technologies Branch, is the DOE counterpart to the Task Group Chairman and has responsibility for the OAFS program within OOE.

G. M. Haas, Chief
Fusion Technologies aranch
Office of Fusion Energy

CONTENTS

CONTENTS (Cont'd)

CONTENTS (Cont'd)

CHAPTER 1

IRRADIATION TEST FACILITIES

D. W. Short and D. W. Heikkinen (Lawrence Livermore National Laboratory)

1.0 Objective

The objectives of this work are operation of RTNS-II (a 14-MeV neutron source facility), machine development, and support of the experimental program that utilizes this facility. Experimenter services include dosimetry, handling, scheduling, coordination, and reporting. RTNS-II is supported jointly by the U.S. and Japan and is dedicated to materials research for the fusion power program. Its primary use is to aid in the development of models of high-energy neutron effects. Such models are needed in interpreting and projecting to the fusion environment, engineering data obtained in other spectra.

2.0 Summary

Irradiations were performed on seven different experiments during this quarter. The sixth U.S.-Japan Steering Committee Meeting was held February 6-7, 1986 at RTNS-II.

3.0 Program

Title: RTNS-II operations (WZJ-16)
Principal Investigator: D. W. Short
Affiliation: Lawrence Livermore National Laboratory

4.0 Relevant DAFS Program Plan Task/Subtask

TASK II,A,2,3,4,
TASK II,B,3,4
TASK II,C,1,2,6,11,18,

5.0 Irradiation

During this quarter, irradiations (both dedicated and add-on) were done for the following people.

Experimenter	P OR A*	Sample Irradiated
K. Kawamura	A	Li_2O-PbF_2 - tritium production
E. Goldberg (LLNL)	A	Al - ^{24}Na calibration source
M. Sugisaki (Kyushu)	P	Al-Mg-Li - tritium production
N. Itoh/K. Tanimura (Nagoya)	P	$MgAl_2O_3$, Al_2O_3 & MgO - volume change
T. Yoshiie (Hokkaido/ H. Kawanishi (Tokyo) K. Miyahara (Tokyo) M. Kiritani (Hokkaido) A. Kohyama (Tokyo) R. Oshima (Osaka)	P	Metals - displacement damage & mechanical properties. Ceramics - neutron damage - irradiated at 200% and 450%

Experimenter	P or A*	Sample Irradiated
H. Yoshida (Kyoto) K. Abe (Tohoku) H. Matsui (Tohoku) H. Kayano (Tohoku) H. Kawanishi (Tokyo) Y. Shimomura (Hiroshima) N. Yoshida (Kyushu) S. Ishino (Tokyo) H. Takahashi (Hokkaido) C. Kinoshita (Kyushu) K. Kamata (Nagoya) K. Saka (Nagoya) M. Iseki (Nagoya) K. Hirata (Osaka) T. Kino (Hiroshima) H. Heinisch (HEDL) F. Clinard (LANL)		
R. Borg (LLNL)	A	NiZr, NiNb & NiHf - TEM, phase transformation
L. Hansen (LLNL)	A	Mo - activation products

* P = primary, A = add-on

5.1 RTNS-II Stat - W. Short and D. W. Heikkinen

The Sixth U.S.-Japan Steering Committee Meeting was held February 6–7, 1986 at RTNS-II.

Both neutron sources operated on a near 24-hour, five-day week schedule.

6.0 Future Work

Irradiations will be continued for T. Yoshiie (Hokkaido)/H. Kawanishi (Tokyo) et al., G. Goldberg (LLNL) and R. Borg (LLNL). Also during this period, irradiations for Y. Shimomura (Hiroshima) et al., M. Guinan/J. Huang (LLNL), D. Neff (Rockwell) and C. Smith (LLNL) will be initiated.

Operations will begin to be reduced toward the end of this quarter.

CHAPTER 2

DOSIMETRY AND DAMAGE PARAMETERS

EXPERIMENTS IN THE OMEGA WEST REACTOR (LANL)

L. R. Greenwood (Argonne National Laboratory)

1.0 Objective

To characterize material irradiation experiments in terms of neutron fluence. spectra, and damage parameters (dpa, gas production).

2.0 Summary

Results are reported for fusion-fission correlation experiments in the Omega West Reactor (Los Alamos National Laboratory). Three short irradiations were performed from August to October 1985 with neutron fluences between $5.2\text{-}54 \times 10^{18}$ n/cm^2. The status of all fusion dosimetry is summarized in Table 1.

Table 1. Status Of Dosimetry Experiments

Facility/Experiment		Status/Comments
ORR	- MFE 1	Completed 12/79
	- MFE 2	Completed 06/81
	- MFE 4A1	Completed 12/81
	- MFE 4A2	Completed 11/82
	- MFE 4B	Completed 04/84
	- MFE 4A3, 4B2	Samples received 11/85
	- TBC 07	Completed 07/80
	- TRIO-Test	Canpleted 07/82
	- TRIO-I	Completed 12/83
	- HF Test	Completed 03/84
	- J6 Test	Completed 07/85
	- J6, J7	Irradiations in Progress
HFIR	- CTR 32	Completed 04/82
	- CTR 31, 34, 35	Completed 04/83
	- T2, RB1	Completed 09/83
	- T1, CTR 39	Completed 01/84
	- CTR 40-45	Completed 09/84
	- CTR 30. 36. 46	Ccmpleted 03/85
	- RB2	Completed 06/85
	- CTR 47-56	Irradiations in Progress
	- JP1, JP3	Completed 12/85
	- JP 2-8	Irradiations in Progress
	- Hf Spectral Analysis	Completed 09/85
	- Hf Test	Completed 12/85
Omega West	- Spectral Analysis	Completed 10/80
	- HEDL1	Cunpleted 05/81
	- HEDL2	Completed 01/86
	- HEDL3	Samples received 03/86
	- LANL 1	Completed 08/84
BSR	- Spectral Analysis	Planned for 05/86
EBR II	- X287	Completed 09/81
IPNS	- Spectral Analysis	Completed 01/82
	- LANL 1 (Hurley)	Completed 06/82
	- Hurley	Completed 02/83
	- Coltman	Completed 08/83

3.0 Program

Title: Dosimetry and Damage Analysis
Principal Investigator: L. R. Greenwood
Affiliation: Argonne National Laboratory

4.0 Relevant DAFS Program Plan Task/Subtask

Task II.A.1 Fission Reactor Dosimetry

5.0 Accomplishments and Status

Dosimetry measurements have been completed for an ongoing series of experiments by Howard Heinisch/HEDL in the Omega West Reactor at Los Alamos National Laboratory.[1,2] The purpose of these elevated temperature experiments is to compare materials damage in the WR with that in the 14-MeV flux at the Rotating Target Neutron Source II at Lawrence Livermore National Laboratory. These fission-fusion correlations Can then be used to relate damage measured in fission reactors to future fusion reactors.

The three present experiments were conducted from August 16-September 12. 1985 far 671.2 MWH; October 15-18, 1985 for 173.6 MWH: and on October 21-22, 1985 for 64.0 MWH. All three experiments were operated at the full reactor power of 8 MW at an average temperature of 90°C.

Dosimetry packages containing Fe, Ni, Ti, and 0.1% Co-A1 wires were inserted in each irradiation capsule. Following the irradiation, these wires were analyzed at ANL by gamma spectroscopy and the measured activation rates are listed in Table 2.

Table 2. Activation Rates for Omega West Reactor
Values are normalized to 8 MW;
uncertainty ±2%

Reaction	FPH[a] =	activity (atoms/atom-sec) 83.9	21.6	8.0
$^{59}Co(n,\gamma)^{60}Co$ (10^{-9})		2.26	2.30	2.22
$^{58}Fe(n,\gamma)^{59}Fe$ (10^{-11})		6.73	7.31	7.00
$^{54}Fe(n,p)^{54}Mn$ (10^{-12})		2.80	2.86	2.81
$^{58}Ni(n,p)^{58}Co$ (10^{-12})		3.56	3.73	3.67
$^{46}Ti(n,p)^{46}Sc$ (10^{-13})		3.67	3.95	3.82

[a]Full power hours at 8 MW power level.

The activities in Table 2 were used to adjust the neutron spectrum measured previously in the Omega West Reactor[1,2] using the STAY'SL computer code. The present results are in good agreement with previous measurements. The thermal flux is about 5% higher and the fast flux about 3% lower than in our previous measurement. The adjusted fluences are listed in Table 3.

Damage rates for this position have been reported previously[1,2] and damage for the current runs can be easily scaled according to the neutron fluences.

Further measurements are in progress in the OWR and we expect to receive dosimeters shortly.

6.0 References

1. L. R. Greenwood, Damage Analysis and Fundamental Studies Quarterly Prowess Report, DOE/ER-0046/4, p. 15 (1981).

2. L. R. Greenwood, Damage Analysis and Fundamental Studies Puarterlv Prom-ess Report, DOE/ER-0046/6, p. 17 (1981).

Table 3. Neutron Fluences for Omega West Reactor
Estimated Uncertainty ±10%

Energy	FPH[a] =	Neutron Fluence, x 10^{18} n/cm^2 83.9	21.6	8.0
Total		54.2	14.41	5.18
Thermal[b]		22.9	6.06	2.16
0.5 eV-0.1 MeV		14.7	3.92	1.41
>0.1 MeV		16.6	4.43	1.60

[a]Full power hours (8 MW).
[b]Thermal flux below 0.5 eV.

7.0 Future Work

Analysis is in progress from the MFE4A and 4B spectral-tailoring experiments in ORR. We are planning to characterize the new low temperature facility in the BSR.

8.0 Publications

The fallowing papers have been submitted to the International Conference on Fusion Reactor Materials (ICFRM2) in Chicago, April 13-17, 1986:

1. L. R. Greenwood, New Ideas in Dosimetry and Damage Calculations for Fusion Materials Irradiations.

2. D. W. Kneff. L. R. Greenwood, B. M. Oliver, and R. P. Skouranski, Helium Production in HFIR-Irradiated Pure Elements.

3. W. A. Coghlan, F. W. Clinard, Jr., N. Itah, and L. R. Greenwood, Swelling of Spinel after Low-Dose Neutron Irradiation.

Two papers have also been submitted to the Symposium on the Effects of Radiation on Materials, Seattle, June 23-25, 1986:

4. L. R. Greenwood, Recent Research in Neutron Dosimetry and Damage Analysis for Materials Irradiations.

5. D. R. Davidson, R. C. Reedy, L. R. Greenwood, W. F. Sommer. and M. S. Wechsler, Additional Measurements of the Radiation Environment at the Los Alamos Spallation Radiation Effects Facility at LAMPF.

DEVELOPMENT OF THE SPECOMP COMPUTER CODE

L. R. Greenwood (Argonne National Laboratory)

1.0 Objective

To determine displacement damage for alloys, insulators, and breeder materials.

2.0 Summary

A new computer code, SPECOMP, has been developed to calculate displacement damage for compounds rather than just for pure elements as is done in our SPECTER code. Examples are shown for $LiAlO_2$ where we find 20-40% more damage in the compound than would be expected from a combination of elements using SPECTER. Other alloy, insulator and breeder materials are now being studied.

3.0 Program

Title: Dosimetry and Damage Analysis
Principal Investigator: L. R. Greenwood
Affiliation: Argonne National Laboratory

4.0 Relevant DAFS Program Plan Task/Subtask

Task II.B.1 Calculation of Defect Production Cross Section

5.0 Accomplishments and Status

A new computer code SPECOMP is being developed to calculate radiation damage for compound materials. Our SPECTER' code routinely calculates damage for 38 pure elements; however, it does not handle compounds and there are no other existing codes which fill this need. Consequently, we have developed SPECOMP.

Fortunately, SPECOMP can make use of the recoil atom energy distributions in SPECTER. Hence, it is not necessary to return to the basic neutron cross sections in ENDF/B-V and recalculate these data. This greatly reduces the size and scope of the code as well as the effort needed to develop the code and the cost to run it.

SPECTER already contains recoil atom energy distributions for each element at 100 neutron energies on a 100-paint recoil energy grid. SPECOMP only needs to access these distributions, combine them according to the alloy or compound of interest, and to integrate over the appropriate secondary damage function for each combination of recoil atom and matrix atom. The secondary displacement model uses the same rescription as SPECTER. relying on the Lindhard partition of the stopping energy and the Robinson model.' Hence, the SPECOMP code is relatively small consisting of subroutines which access the SPECTER data files, calculate the appropriate secondary displacements, and integrate over the recoil spectra at each neutron energy.

Although the code is still undergoing testing, sample calculations are shown for a fusion breeder material $LiAlO_2$ in Fig. 1. As can be seen at low energies, damage is due to the $^6Li(n,\alpha)t$ reaction. At higher energies the displacement damage predicted by SPECOMP is 20-40% higher than would be predicted by taking a simple average of the results from SPECTER. Integral dpa rates for $LiAlO_2$ are 26-28% higher for a fusion first wall or fast reactor spectra and 7% higher in a mixed-spectrum reactor like HFIR due to the dominance of the ^6Li damage.

Although we have not had time to study SPECOMP predictions in detail. it is clear from early runs that the prediction of Parkin and Coulter[3] holds up, namely, that in cases where the mass differences are small SPECOMP will differ only slightly from a linear sum of the elements in SPECTER. On the other hand, when the masses involved are quite different, then the calculated displacements, from SPECOMP may differ substantially from SPECTER. In the Present case we find that calculations for SiO_2 and Al_2O_3 agree within 5% of the linear sum from SPECTER whereas Li_2O, $LiAlO_2$, and TaO disagree by 20-40% over the energy range from 0.1 to 20 MeV.

6.0 References

1. L. R. Greenwood and R. K. Smither, SPECTER: Neutron Damage Calculations for Material? Irradiations, ANL/FPP-TM-197, 1985.

2. G. R. Odette and D. R. Dorian, Nucl. Technol. 29, 346 (1976).

3. D. M. Parkin and C. A. Coulter. J. Nucl. Mater. 103, 1315-1318 (1981).

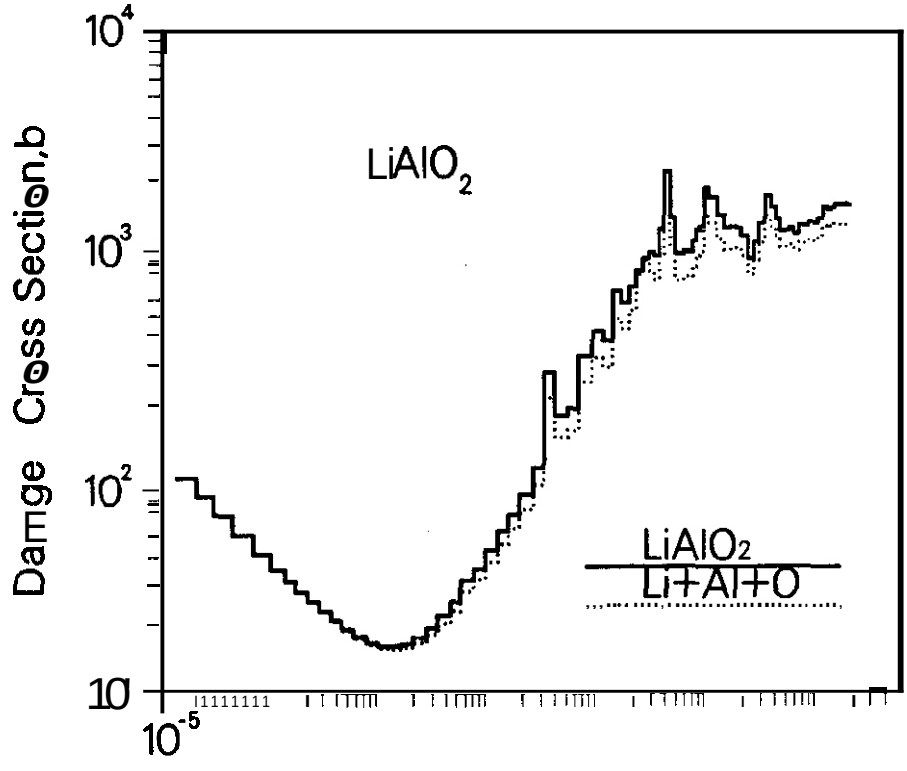

Fig. 1. Displacement Damage Cross Sections are Compared for $LiAlO_2$ using SPECOMP and a Linear Combination of the Elements in SPECTER. Damage is due to the $^6Li(n,\alpha,t)$ Reaction at Low Energies.

7.0 Future Work

We plan to perform calculations for other compounds and to release the displacement cross sections for routine use in SPECTER. Hence, it will become easy to routinely predict displacement damage in a number of compounds (alloys, insulators, breeder materials) of interest to the fusion program, Of course, one major remaining problem is that the threshold energies for each species in a compound are not well-known and may differ substantially from elemental values. Hence, further research is needed to establish the appropriate values for each compound of interest.

8.0 Publications

None.

MEASUREMENT OF ^{91}Nb, ^{94}Nb, AND ^{95}Nb FROM Mo BY 14.5-14.8 MeV NEUTRONS

L. R. Greenwood (Argonne National Laboratory)

1.0 Objective

To develop nuclear data and dosimetry techniques for high-energy neutron facilities and fusion reactors.

2.0 Summary

Samples of natural Mo and ^{94}Mo were irradiated at the Rotating Target Neutron Source II (Lawrence Livermore National Laboratory) and production cross sections were determined for the long-lived isotope ^{94}Nb (20,300 y) to be about 56 mb from ^{94}Mo and 7.9 mb from natural Mo near 14.6 MeV. The cross section for the production of ^{91g}Nb (700 y) from natural Mo is about 45 mb. These data can be used to calculate the production of these isotopes in a fusion reactor.

3.0 Program

Title: Dosimetry and Damage Analysis
Principal Investigator: L. R. Greenwood
Affiliation: Argonne National Laboratory

4.0 Relevant DAFS Program Plan Task/Subtask

Task II.A.2 High-Energy Neutron Dosimetry
Task II.A.7 MFR Dosimetry

5.0 Accomplishments and S——

We have been engaged in a program to measure the production cross sections for long-lived isotopes in fusion materials. Previously we have reported measurements for ^{26}Al (7.2x10^{5}y)[1] and ^{53}Mn (3.7x10^{6}y).[2] Cross sections to 22 shorter-lived reactions have also been reported recently.[3] In the present report, measurements are given for various reactions of Mo with particular interest in ^{94}Nb (2.03x10^{4}y). Data are also reported for the ^{95}Mo (n,p)^{95}Nb, ^{92}Mo(n,x)^{91m}Nb, and ^{98}Mo(n,α)^{95}Zr reactions. ^{91m}Nb is also of interest in fusion material3 since this isomer decays to the long-lived ground state ^{91g}Nb (700 y).

Enriched ^{94}Mo and natural Mo specimens were irradiated at the Rotating Target Neutron Source II at Laurence Livermore National Laboratory in collaboration with Don Doran and Howard Heinisch (Hanford Engineering Development Laboratory). Due to the low-flux levels. and RTNS II operating schedule. the specimens were irradiated for a total of 81 days over a period of seven months. The neutron spectra were calculated[3] for each sample position and the fluence was determined by mapping the response of iron fails located at 113 different positions around the target. This fluence map allows us to determine the relative fluence on our samples to within ±5%; however, the absolute fluence is only known to about ±7%.

The presence of ^{94}Nb in the irradiated samples was determined by gamma spectroscopy. The two natural Mo and two ^{94}Mo (92%), specimens were counted at six different decay times over a period of 16 months. Such a long time was needed to reduce the background due to shorter-lived activities. ^{91m}Nb and ^{95}Zr activities were also determined from these counts. The ^{95}Zr activity had to be corrected for the decay of ^{95}Nb both during and after the irradiation. Corrections were also made for the isotopic ratios in the enriched and ^{94}Mo samples to separate reactions from different isotopes.

The resulting cross sections are listed in Table 1. Although there are few measurements for these reactions, the present results are in satisfactory agreement. There are no reported activation measurements for ^{94}Nb and our results provide the only means of measuring the production of this isotope in Mo. As an example, assuming a neutron wall load of 1 MW/m^2 in an operating fusion reactor, the production of ^{94}Nb (20,300 y) in Mo would be about 1.9 μCi/g after 1 year or 38 μCi/g after 20 years. Using our estimates for the production of ^{91g}Nb (700 y) gives 35 mCi/g after 1 year and 7 Ci/g after 20 years. Of course. ^{91g}Nb decays by electron capture producing only low-energy x-rays and hence is not as difficult to handle as ^{94}Nb which has a much longer half-life and 2 high energy gammas (702 and 871 keV).

We should note that Mo also produces other long-lived isotopes such as ^{93}Mo (3500 y), ^{93}Zr (1.5x10^{6}y), and ^{92}Nb (3.7x10^{7}y) and we plan to measure the production cross sections for these as well as other long-lived isotopes in other materials in the future.

Table 1. Measured Cross Sections (mb) for Mo

Reaction	Neutron Energy, MeV 14.55	14.60	14.78	14.80	±% [a]
$^{94}Mo(n,p)\ ^{94}Nb$	57.2	-	53.1	-	11
$^{Nat}Mo(n,x)\ ^{94}Nb$ [b]	-	7.9	-	7.8	12
$^{95}Mo(n,x)\ ^{94}Nb$ [c]	-	16.3	-	18.3	16
$^{95}Mo(n,x)\ ^{95}Nb$	40.4	-	37.1	-	9
$^{92}Mo(n,x)\ ^{91m}Nb$ [d]	157.	153.	145.	145.	10
$^{98}Mo(n,\alpha)\ ^{95}Zr$	6.56	6.56	6.24	6.21	8
$^{92}Mo(n,x)\ ^{91g}Nb$	≈300				
$^{Nat}Mo(n,x)\ ^{91g}Nb$	≈ 45				

[a] Major sources of uncertainty include neutron fluence (7%), ^{94}Nb half-life (8%), efficiency (1.5%), statistics (1%), deconvolution of (12%) for ^{94}Nb, (2%) for ^{95}Nb.
[b] sum reactions from $^{94,95,96}Mo$
Sum of (n,d + np + pn) reactions.
Sum of (n,2n + d + np + pn) reactions.

6.0 References

1. R. K. Smither and L. R. Greenwood, J. Nucl. Mater. 122, 1071-1077, 1984

2. R. K. Smither and L. R. Greenwood, Damage Analysis and Fundamental Studies Quarterly Progress Report, DOE/ER-0046/17, pp. 11-13, May 1984.

3. L. R. Greenwood, M. W. Guinan, and D. W. Kneff. Damage Analysis and Fundamental Studies Quarterly Progress Report, DOE/ER-0046/21, pp. 15-18. May 1985.

7.0 Future Work

Further irradiations are being planned at RTNS II and we plan to measure production cross Sections for many other long-lived isotopes.

8.0 Publications

A paper has been drafted and will be submitted to Nuclear Science and Engineering.

HELIUM PRODUCTION IN MIXED SPECTRUM REACTOR-IRRADIATED PURE ELEMENTS

D. W. Kneff, B. M. Oliver, and R. P. Skowronski (Rockwell International)

1.0 Objective

The objectives of this work are to apply helium accumulation neutron dosimetry to the measurement of neutron fluences and energy spectra in mixed-spectrum fission reactors utilized for fusion materials testing, and to measure helium generation rates of materials in these irradiation environments.

2.0 Summary

Helium generation measurements have been made for several Fe, Cu, Ti, Nb, Cr, and Pt samples irradiated in the mixed-spectrum High Flux Isotope Reactor (HFIR) and Oak Ridge Research Reactor (ORR) at the Oak Ridge National Laboratory. The results have been used to integrally test the ENDF/B-V Gas Production File, by comparing the measurements with helium generation predictions made by Argonne National Laboratory using ENDF/B-V cross sections and adjusted reactor spectra. The comparisons indicate consistency between the helium measurements and ENDF/B-V for iron, but cross section discrepancies exist for helium production by fast neutrons in Cu, Ti. Nb, and Cr (the latter for ORR). The Fe. Cu, and Ti work updates and extends previous measurements.

3.0 Program

Title: Helium Generation in Fusion Reactor Materials
Principal Investigators: D. W. Kneff and H. Farrar IV
Affiliation: Rockwell International

4.0 Relevant OAFS Program Plan Task/Subtask

Task II.A.1	Fission Reactor Dosimetry
Task II.A.4	Gas Generation Rates
Subtask II.A.5.1	Helium Accumulation Monitor Development

5.0 Accomplishments and Status

Helium generation measurements have been made for the pure elements Fe, Cu, Ti, Nb, Cr, and Pt in the mixed-spectrum reactors HFIR and ORR. The results have been compared with helium predictions in order to integrally test helium production cross sections from the ENDF/B-V Gas Production File in this energy region. This work is part of a joint Rockwell-Argonne National Laboratory (ANL) program to measure total helium production rates over the range of fission reactor neutron spectra and fluences used for fusion materials testing, and to use the results to test helium production cross section evaluations used in damage calculations.

Pure element samples were irradiated in HFIR as part of experiments CTR30, CTR31, CTR32, and the spectral characterization irradiation RB/HF, and in ORR as part of experiments MFE2, MFE4A2, and MFE4B. Most of the samples were irradiated as bare wire segments, and were used both for helium accumulation and radiometric dosimetry measurements. The irradiated samples were first counted radiometrically at ANL. They were then sent to Rockwell, where they were etched, to remove any helium recoil effects, and segmented for ^4He analysis. The ^4He analyses were performed by high-sensitivity isotope-dilution gas mass spectrometry, (1) and included multiple analyses for most sample locations. The absolute uncertainties in most of the

analyses were ±1-2%. Selected samples from each irradiation were also analyzed for ^{3}He, which is formed from the decay of tritium often found in reactor environments. The ^{3}He concentrations were generally found to be less than 1 appb (10^{-9} atom fraction) for Fe, Cu, Cr, and Pt, and somewhat higher (~2 to 170 appb) for the CTR and MFE Ti and Nb samples.

The analyzed samples are listed in Tables 1-5. These tables also give the samples' irradiation locations, neutron fluences, measured helium concentrations, and comparisons between the measurements and predictions. Some of these measurements have been reported previously,[2-5] but the corresponding helium predictions have been updated here for integral cross section testing (see below). Analyses are continuing for some additional samples of these materials from these irradiation experiments.

The predictions are based on radiometric dosimetry measurements and calculated helium production concentrations by L. R. Greenwood,[6-11] using ENDF/B-V cross section evaluations. Since the purpose of the present work is to integrally test the ENDF/B-V Gas Production File, some adjustments have been made to the published predictions. These adjustments include a change from the ENDF/B-V General Purpose File used for MFE2 and MFE4A2 to the Gas Production File, and a modification of some reactor gradients used in the calculations. The prediction of generated helium at a given sample location has generally been performed by calculating the helium generation at the peak flux position in the experimental volume, and then scaling the helium generation at other locations by the average flux gradient derived from the radiometric dosimeters. However, the reactor flux gradients are not identical for the fast and thermal neutron components, with helium generated in most cases by fast neutrons. For the present work, the helium predictions at the various sample locations were determined using the calculated fast-neutron gradients or, where possible, ratios of ANL-measured fast-reaction activation data at the samples' locations. The most direct gradient data were obtained for the Fe and Ti samples, for which the measured $^{54}Fe(n,p)^{54}Mn$ and $^{46}Ti(n,p)^{46}Sc$ reaction rates were used. Final spectrum plus gradient uncertainties are estimated to be about ±10%.

Comparisons between the measured and predicted helium generation in the analyzed samples are given in the last column of Tables 1-5, where they are expressed as ratios of the calcirlated (predicted) to experimental values (C/E). The average ratios are summarized in Table 6. The C/E ratios provide a test of the spectrum-integrated ENDF/B-V cross sections for the neutron energy spectra seen by the samples, and an indicator of any high-fluence effects on helium generation rates. (See, for example, Ref. 5 and 12 for the copper three-stage reaction with thermal neutrons.) Examination of Table 6 indicates that the ENDF/B-V cross sections, coupled with the unfolded neutron energy spectra, provide generally good agreement (within the ±10% uncertainties) for Fe (ORR and HFIR) and Cr (HFIR only). However, the comparisons for Cu, Ti, Nh, and Cr (ORR) indicate significant discrepancies in the ENDF/B-V cross sections for helium production by fast neutrons.

For iron (Tahle 1), the HFIR C/E values exhibit a decreasing trend with increasing neutron fluence. This suggests a small, nonlinear increase in helium production with neutron fluence at high fluences, due to burnup and multiple-step reactions. The lower-fluence C/E values thus provide a better comparison for testing ENDF/B-V fast-neutron cross sections. At the lower fluences, the HiIR C/E values are systematicallv higher than the ORR values. This difference is attributed to spectral differences that are not reflected in the calculations.

Helium production in copper for the reported experiments (Table 2) is dominated by fast neutrons because of the relatively low neutron fluences. Corrections[12] to the calculations for helium production in HFIR by the thermal three-stage mechanism in copper were negligible for the Hf-covered samples and 3-4% for the bare samples. No three-stage contributions have been included in the ORR calculations, because our measured cross sections[12] for the three-stage reaction are soecifically for the HFIR spectrum. However, they are estimated to be -3-6% of the fast contribution for #E2 and MFE4A2, and ~7-9% for MFE4B. This would produce a small increase in the C/E values. The average C/E values measured for the copper samples from ORR 10.65 ± 0.04), HFIR-RB (0.58 ± 0.02), and HFIR-PTP 10.76 ± 0.05, Ref. 12) have systematic differences, which are again attributed to spectral differences between the irradiation environments that are not reflectel in the calculations. The same assumption is made about the systematic differences observed between the C/E values from ORR and HiIR for Nb (Tables 4 and 61, and for bare and Hf-covered Ti from the HFIR-RB position (Tables 3 and 61.

The chromium C/E values (Table 5) show large discrepancies between the ORR- and HFIR-irradiated samples. Only one reactor location has been analyzed to date for each reactor, and further measurements are required. Additional work is in progress.

There is no ENDF/B-V helium production evaluation for platinum (Table 5), which was analyzed as an encapsulating material for selected samples. The helium measurement results confirm its relatively small helium production cross section.

TABLE 1 HELIUM PRODUCTION MEASUREMNTS FOR REACTOR-IRRADIATED IRON

Experiment	Sample	Core Height[a] (cm)	Total Fluence (10^{22} n/cm^2)	^{4}He Concentration (appm)[b] Measured	^{4}He Concentration (appm)[b] Calculated[c]	Calculated/Measured (C/E)
ORR-MFE4A2	Fe-5B	- 6.27 inner	1.76	1.62	1.58 (d)	0.98
	Fe-88	- 6.27 outer	1.88	1.80	1.65 (d)	0.92
	Fe-LI	-10.96 inner	1.72	1.56	1.55	0.99
	Fe-M2	-11.43 outer	1.83	1.65	1.61	0.98
	Fe-48	-14.69 outer	1.76	1.58	1.55 (d)	0.98
	Fe-1B	-14.84 inner	1.64	1.54	1.47 (d)	0.96
ORR-MFE4B	Fe-38	-14.53 inner	1.71	1.60	1.60	1.00
	Fe-4B	-14.53 outer	1.77	1.58	1.59	1.01
HFIR-CTR32	Fe-25	+17.61	3.48	2.24	2.37	1.06
	Fe-3	+ 4.41	4.81	3.12	3.25 (d)	1.04
	Fe-E8	- 7.38	4.60	2.99	3.14	1.05
HFIR-CTR31	Fe-1	+21.07	5.57	3.66	3.68 (d)	1.01
	Fe-3	+ 4.41	9.67	6.76	6.39 (d)	0.95
	Fe-5	-12.26	8.30	5.73	5.64 (d)	0.98
HFIR-CTR30	Fe-1	+21.07	11.05	8.17	7.64	0.94
	Fe-3	+ 4.41	19.16	14.69	12.95	0.88
	Fe-5	-12.26	16.45	12.36	10.99	0.89

(a) Distance above core midplane
(b) Atomic parts per million (10^{-6} atom fraction)
(c) L. R. Greenwood, Refs. 7-10
(d) Revision of previously reported values (see text)

TABLE 2. HELIUM PRODUCTION MEASUREMENTS FOR REACTOR-IRRADIATED COPPER

Experiment	Sample	core Height[a] (cm)	Neutron Fluence (10^{22} n/cm^2) Thermal	Neutron Fluence (10^{22} n/cm^2) Total	^{4}He Concentration (appm)[b] Measured	^{4}He Concentration (appm)[b] Calculated[c]	Calculated/Measured (C/E)
ORR-WE2	Cu-1	+14.67	0.31	1.18	1.24	0.76 (d)	0.61
	cu-2	+ 7.84	0.38	1.42	1.52	0.91 (d)	0.60
	cu-4	+ 1.13	0.42	1.58	1.68	1.02 (d)	0.61
	cu-3	- 5.81	0.45	1.68	1.82	1.08 (d)	0.59
ORR-MFE4A2	Cu-Y4	- 3.65 inner	0.45	1.75	1.97	1.35 (d)	0.69
	cu-5	- 5.40 inner	0.45	1.76	2.02	1.36 (d)	0.67
	Cu-8	- 5.41 outer	0.49	1.88	2.16	1.44 (d)	0.67
	cu-4	-13.82 outer	0.47	1.78	2.03	1.37 (d)	0.67
	Cu-1	-13.97 inner	0.43	1.66	1.88	1.29 (d)	0.69
ORR-MFE4B	Cu-3	-13.64 inner	0.54	1.76	2.03	1.45 (d)	0.71
	cu-4	-13.64 outer	0.58	1.81	1.99	1.38 (d)	0.69
HFIR-RB/HF (Hf-covered)	Cu-72	+20.24	0.0091	0.095	0.072	0.039	0.54
	Cu-75	- 3.88	0.0162	0.170	0.117	0.070	0.60
	cu-77	-13.41	0.0127	0.132	0.0%	0.055	0.57
HFIR-RB/HF (bare)	Cu-83	+11.51	0.139	0.384	0.113	0.069 (e)	0.61
	cu-85	- 3.73	0.158	0.435	0.136	0.079 (e)	0.58
	cu-87	-12.62	0.127	0.351	0.110	0.063 (e)	0.57

(a) Distance above core midplane
(b) Atomic parts per million (10^{-6} atom fraction)
(c) L. R. Greenwood, Refs. 6,7,9,11
(d) Revision of previously reported values (see text); omits thermal three-stage reaction contribution
(e) Prediction includes 0.002-0.003 appm thermal contribution

TABLE 3. HELIUM PROOUCTION MEASUREMENTS FOR REACTOR-IRRAOIATEO TITANIUM

Experiment	Sample	Core Height(a) (cm)	Total Fluence (10^{22} n/cm^2)	^{4}He Concentration (appm)(b) Measured	^{4}He Concentration (appm)(b) Calculated(c)	Calculated/Measured (C/E)
ORR-MFE2	Ti-1	t14.67	1.18	0.78	1.75 (d)	2.24
	Ti-2	+ 7.84	1.42	0.94	2.11 (d)	2.24
	Ti-3	- 5.81	1.68	1.09	2.49 (d)	2.28
ORR-MFE4A2	Ti-M5	- 3.02 inner	1.75	1.16	2.73	2.36
	Ti-5	- 4.22 inner	1.76	1.16	2.74 (d)	2.36
	Ti-8	- 4.22 outer	1.88	1.23	2.89 (d)	2.35
	Ti-V5	-12.23 inner	1.70	1.12	2.66	2.37
	Ti-4	-12.62 outer	1.81	1.18	2.79 (d)	2.36
	Ti-1	-12.78 inner	1.69	1.13	2.64 (d)	2.34
ORR-MFE4B	Ti-3	-11.73 inner	1.84	1.20	2.96	2.47
	Ti-4	-11.73 outer	1.89	1.20	2.96	2.47
HiIR-CTR32	Ti-3	+ 4.57	4.80	2.17	5.52 (d)	2.54
HFIR-CTR31	Ti-1	t21.23	5.51	2.52	6.04 (d)	2.40
	Ti-3	+ 4.57	9.65	4.29	10.49 (d)	2.45
	Ti-5	-12.10	8.34	3.90	9.46 (d)	2.42
HiIR-CTR30	Ti-1	+21.23	10.92	5.27	12.27	2.33
	Ti-3	+ 4.57	19.14	8.49	21.44	2.52
	Ti-5	-12.10	16.53	7.67	18.67	2.43
HFIR-RB/HF (Hf-covered)	Ti-74	- 0.08	0.174	0.086	0.210	2.44
	Ti-77	-12.78	0.136	0.064	0.160	2.50
	Ti-78	-19.76	0.086	0.046	0.114	2.50
HFIR-RB/HF (bare)	Ti-82	t20.72	0.233	0.068	0.132	1.93
	Ti-84	- 0.07	0.446	0.106	0.234	2.21
	Ti-86	- 7.69	0.408	0.096	0.209	2.17
	Ti-88	-18.81	0.241	0.067	0.130	1.93

(a) Distance above core midplane
(b) Atomic parts per million (10^{-6} atom fraction)
(c) L. R. Greenwood, Refs. 6-11
(d) Revision of previously reported values (see text)

TABLE 4. HELIUM PRODUCTION MEASUREMENTS FOR REACTOR-IRRAOIATEO NIOBIUM

Experiment	Sample	Core Height(a) (cm)	Total Fluence (10^{22} n/cm^2)	4He Concentration (appm)(b) Measured	4He Concentration (appm)(b) Calculated(c)	Calculated/Measured (C/E)
ORR-MFE2	Nb-1	+15.37	1.15	0.286	0.165	0.58
	Nb-2	+ 8.54	1.40	0.335	0.202	0.60
	Nb-3	- 5.11	1.67	0.400	0.241	0.60
ORR-MFE4A2	Nbl-1	-13.38 inner	1.68	0.511	0.286	0.56
	Nbl-4	-13.22 outer	1.80	0.544	0.296	0.54
HFIR-CTR32	Nb-3	+ 4.73	4.79	0.78	0.59	0.75
HFIR-CTR31	Nb-1	+21.39	5.44	0.90	0.66	0.73
	Nb-3	+ 4.73	9.64	1.54	1.18	0.76
	Nb-5	-11.94	8.38	1.43	1.02	0.71
HiIR-CTR30	Nb-1	t21.39	10.79	1.93	1.32	0.68
	Nb-3	+ 4.73	19.11	3.09	2.33	0.75
	Nb-5	-11.94	16.60	2.69	2.03	0.75

See Table 3 for footnotes.

TABLE 5. HELIUM PRODUCTION MEASUREKNTS FOR REACTOR-IRRADIATED CHROMIUM AND PLATINUM

Material	Experiment	Core Height[a] (cm)	Total Fluence (10^{22} n/cm^2)	^{4}He Concentration (appm)[b] Measured	^{4}He Concentration (appm)[b] Calculated[c]	Calculated/Measured (C/E)
Chromium	ORR-MFE4A2	- 3.02 outer	1.87	0.701	0.96	1.37
	HFIR-RB/HF (Hf-covered)	- 8.89	0.155	0.049	0.052	1.06
Platinum	ORR-MFE4A2	- 3.02 outer	1.87	0.0041	--	--
	HFIR-CTR30	-16.34	14.13	0.032	--	--
		-24.67	7.39	0.015	--	--

(a) Distance above core midplane
(b) Atomic parts per million (10^{-6} atom fraction)
(c) L. R. Greenwood, Refs. 7,10,11

TABLE 6. SUMMARY OF CALCULATION/EXPERIMENT (C/E) VALUES FOR ANALYZED MATERIALS

Material	Reactor	C/E Value	Comments
Iron	ORR	0.98 ± 0.03	
	HFIR-PTP	0.98 ± 0.07	PTP position; some fluence dependence observed
Copper	ORR	0.65 ± 0.04	Fast neutron calc., thermal effect adds ~3-9%
	HFIR-RB	0.57 ± 0.03	Hf-covered samples, RB position; fast neutrons
		0.59 ± 0.02	Bare samples, RB position; fast neutrons
Titanium	ORR	2.35 ± 0.08	
	HFIR-PTP	2.44 ± 0.07	PTP position
	HFIR-RB	2.48 ± 0.03	Hf-covered samples, RB position
		2.06 ± 0.15	Bare samples, RB position
Niobium	ORR	0.58 ± 0.03	
	HFIR-PTP	0.73 ± 0.03	PTP position
Chromium	ORR	1.37	Single comparison only
	HFIR-RB	1.06	Hf-covered RB position; single comparison only

In general, the results demonstrate the ability to use energy-spectrum and helium generation measurements in mixed-spectrum reactors to test spectrum-integrated helium production cross section evaluations. They point out the presence of discrepancies in some ENDF/B-V cross sections, and our previous work has also demonstrated[12] the presence of unexpected high-fluence effects that can contribute significantly to helium production. The high-fluence effects can be used advantageously, such as by doping copper alloys with zinc (an intermediate product of the copper three-stage reaction), to simulate fusion reactor helium generation in mixed-spectrum fission reactors. The cross section discrepancies point out the importance of performing direct helium measurements for all materials of interest in fusion test environments, over the full range of applicable neutron fluences. The measurements provide direct data for the interpretation of materials effects and tests for helium predictions. The combination of measurements and predictions can then be used to provide accurate helium estimates for materials irradiations.

6.0 References

1. B. M. Oliver, J. G. Bradley, and H. Farrar IV, "Helium Concentration in the Earth's Lower Atmosphere," Geochim. Cosmochim. Acta, 48, 1759 (1984).

2. B. M. Oliver, D. W. Kneff, and R. P. Skowronski, "Helium Generation Measurements for EBR-II and ORR," in Uamage Analysis and Fundamental Studies, Quarterly Progress Report January-March 1984, DOE/ER-0046717, U.S. Uepartment of Energy, 14 (1984).

3. D. W. Kneff. B. M. Oliver. and R. P. Skowronski. "Helium Generation Measurements for Iron from HFIR," in Damage Analysis and Fundamental Studies, Quakerly Progress Report July-September 1984, DOE/ER-0046/19, U.S. Department of Energy, 9 (1984).

4. D. W. Kneff, B. M. Oliver, R. P. Skowronski, and L. R. Greenwood. "Helium Production in Reactor-Irradiated Copper and Titanium, and Evidence for a Copper Three-Stage Reaction," in Damage Analysis and Fundamental Studies, Quarterly Progress Report October-December 1984, DOE/ER-0046/20, U.S. Department of Energy, 13 (1985).

5. D. W. Kneff, B. M. Oliver, and R. P. Skowronski, "Helium Production in Reactor-Irradiated Copper," in Damage Analysis and Fundamental Studies, Quarterly Progress Report January-March 1985, DOE/ER-0046/21, U.S. Department of Energy, 37 119851.

6. L. R. Greenwood, "Fission Reactor Dosimetry" [ORR-MFE2], in Damage Analysis and Fundamental Studies, Quarterly Progress Report April-June 1981, DOE/ER-0046/6, U.S. Department of Energy, 17 (1981); and personal comnunications.

7. L. R. Greenwood. "Dosimetry and Damaae Analvsis for the MFE4A Soectral Tailoring Experiment in ORR." in Damage Analysis and Fundamental Studies, Quarterly Progress Report October-December 1982, DOE/ER-6/12, U.S. Uepartment of Energy, 15 (1983); and personal comnunications.

8. L. R. Greenwood, "Fission Reactor Dosimetry - HFIR - CTR 31, 32, 34, and 35," in Damage Analysis and Fundamental Studies, Quarterly Progress Report April-June 1983, DOE/ER-0046/14, U.S. Department of Energy, 9 (1983); and personal comnunications.

9. L. R. Greenwood and R. K. Smither. "Dosimetry Measurements and Damage Calculations for the ORR-MFE4B Experiment, in Damage Analysis and Fundamental Studies, Quarterly Progress Report April-June 1984, DOE/ER-0046/18, U.S. Department of Energy, 5 (1984).

10. L. R. Greenwood, "Fission Reactor Dosimetry - HFIR-CTR 30, 36, 46," in Damage Analysis and Fundamental Studies, Quarterly Progress Report January-March 1985, DOE/ER-0046/21, U.S. Department of Energy, 5 1985); and personal communications.

11. L. R. Greenwood. "Dosimetry and Damaae Analysis for the Hafnium Full-Power Test, JP1, and JP3 Experiments in HFIR," in Damage Analysis and Fundamental Studies, Quarterly Progress Report October-December 1985, DOE/ER-0046/24, U.S. Department of Energy, 5 (1986); and personal communications.

12. D. W. Kneff, L. R. Greenwood, and E. L. Callis, "Helium Production in Copper by a Thermal Three-Stage Reaction," in Damage Analysis and Fundamental Studies, Quarterly Progress Report April-June 1985, DOE/ER-0046/22, U.S. Uepartment ot tnergy, 8 (1985).

7.0 Future Work

Work is continuing to integrally test helium generation predictions for new materials that have been, and will be, irradiated in mixed-spectrum reactor experiments. Helium production measurements in progress include Al, V, Zn, and Mo. Comparisons between the results and calculations will be used to improve helium generation predictions for fusion materials irradiations.

8.0 Publications

D. W. Kneff (Rockwell), L. R. Greenwood (ANL), B. M. Oliver, and R. P. Skowronski (Rockwell), "Helium Production in HFIR-Irradiated Pure Elements," presented at the Second International Conference on Fusion Reactor Materials, Chicago, April 1986 and submitted for publication in J. Nucl. later.

D. W. Kneff, B. M. Oliver, H. Farrar IV (Rockwell), and L. R. Greenwood (ANL), "Helium Production in Pure Elements, Isotopes, and Alloy Steels by 14.8-MeV Neutrons," Nucl. Sci. Eng., 92, 491 (1986).

CHAPTER 3

REDUCED ACTIVATION MATERIALS

PROSPECTS FOR REDUCED ACTIVATION ALLOYS

D. G. Doran (Hanford Engineering Development Laboratory), A. F. Rowcliffe (Oak Ridge National Laboratory), and F. M. Mann (Hanford Engineering Development Laboratory)

1.0 Objective

The objective of this work is to review the status of efforts to reduce the activation of first wall materials to qualify them for near-surface waste disposal.

2.0 *Summary*

A description is given of the framework within which the development of alloys exhibiting reduced activation is being pursued in the U.S. The current status and future prospects of this effort is briefly reviewed. The goal is to reduce activation to a level precluding the need for geologic disposal in order to help make fusion power environmentally and economically attractive. Initial efforts at reducing activation are aimed at replacing problem elements -- especially Nb, Mo, and Ni -- with more benign elements in analogues of structural alloys such as Ti-modified 316 stainless steel, the ferritic/martensitic steels containing 9-12% Cr, and the lower Cr (2%) ferritic/bainitic steels. The intrinsically low activation vanadium alloys are also under study; these are not common structural materials, so a data base is only slowly accumulating. Although this work is at an early stage, it provides evidence for optimism that the goal can be met.

3.0 Program

Title: Irradiation Effects Analysis
Principal Investigator: D. G. Doran
Affiliation: Westinghouse Hanford Company

4.0 Relevant OAFS Program Plan Task/Subtask

No tasks on reduced activation were identified in the original OAFS Program Plan.

5.0 Accomplishments and Status

5.1 Introduction

The purpose of this report is two-fold. One is to examine the framework within which the development of alloys exhibiting reduced activation is being pursued. The second is to survey the current status and future prospects of this development effort.

The U.S. Magnetic Fusion Materials Program has adopted as a major objective the reduction of the activation of fusion reactor components. The general objective *is,* of course, to help make fusion power environmentally and economically attractive, hence increasing both public and utility acceptance. More specifically, reduced activation can (1) decrease the cost and environmental impact of disposing of activated wastes, (2) simplify maintenance and other tasks requiring handling of irradiated materials, (3) decrease personnel exposures, (4) decrease the consequences of certain types of accidents, and (5) increase the potential for recycling of critical or expensive materials. Current thinking is that the greatest impact can be made in the area of waste management.[1] The minimum goal is to reduce activation to a level consistent with near-surface burial, thus precluding the need for geologic disposal. We will not discuss the other potential benefits further, except to point out that the role of half-life and type of radioactive emissions is different for each, hence each leads to different restrictions on material compositions.[2]

5.2 Materials Design Guidelines

The materials designer needs quantitative guidelines on acceptable constituents. To provide these requires, first of all, predictions of the radioactivity induced in all potential reactor materials for the range of neutron fields each may encounter in a fusion device. Although many such calculations have been performed, there is still a need to reduce uncertainties in some cases (as illustrated below) and to broaden the range of flux-spectra examined. Secondly, a basis is needed for deciding on

acceptable levels of activation. The U.S. Nuclear Regulatory Commission (NRC) has established concentration limits (Ci/m^3) for several radionuclides of importance in waste streams from fission reactors and medical applications, viz., the long-lived Ni-59, Nb-94, Tc-99, and C-14 and the shorter-lived Co-60, Ni-63, and H-3. These limits, published in the U.S. Code of Federal Regulations (10CFR61), define whether a material containing one or more of them qualifies for near-surface burial. The role of the NRC is to regulate operations so as to ensure that standards are met. The standards themselves are set by the U.S. Environmental Protection Agency (EPA). The EPA is currently preparing a standard on "low level waste" (irradiated metals at any level of activation are low level wastes by EPA definition) which will probably be expressed in terms of personnel exposures. It is expected that they will be consistent with those used by the NRC in preparing 10CFR61.

Using reasoning similar to that of the NRC, the 10CFR61 list has been augmented [3,4] to cover other radionuclides important for fusion applications. Some of these are given in Table 1, along with the composition limits they imply for two conceptual reactor first wall spectra. The STARFIRE and MARS spectra were chosen because the former, being water cooled, has a significant number of low energy neutrons that are absent in the latter. The six-year exposure corresponds to 21.6 $MW-y/m^2$ in STARFIRE and 25.8 $MW-y/m^2$ in MARS; the cooling period is negligible for the radioisotopes listed. Several points can be made with reference to Table 1. Comparison with earlier calculations [4,5] for a shorter exposure shows that Ni, Nb, and Mo activation is roughly proportional to the fluence (actually increases somewhat less rapidly than the fluence because of burnout). Tungsten activation, on the other hand, varies as the sixth power of the fluence as a result of the six neutrons that must be absorbed to produce Ir-192. The dependence of activation on the first wall neutron spectrum can be large if (n,gamma) reactions dominate, because the cross section is generally high at low neutron energy. This dependence is enhanced in the case of tungsten by the high sensitivity to fluence.

TABLE 1
RECENT ACTIVATION CALCULATIONS WITH EXPANDED DATA BASE
(Six Years, 3000 Day Cooling)

Element	Product	Halflife (Years)	Disposal Limit (Ci/m^3)[1]	Acceptable Concen. Limit/Activation STARFIRE	MARS
N	C-14	5,730	80	~150 wppm	~190 wppm
Ni	Ni-59	76,000	220	.024	.041
	Ni-63	100	7000	.0044	.021
Nb	Nb-94	20,000	0.2	2 ppm	2 ppm
Mo	Nb-94	20,000	0.2	280 ppm	120 ppm
	MO-93	3,500	30 est.[2]	270 ppm	500 ppm
W	Ir-192*	241	1 est.[3]	>0.2 ppm[4]	>>1
	Pt-193	50	$2x10^5$ est.[3]	0.04	>>1

---

1. 10CFR61 Class C
2. Estimated by Kennedy [3]
3. Estimated by authors
4. Could be low by a factor of 1000 or more--cross sections must be evaluated. Varies as $(fluence)^6$.

The results in Table 1 were obtained with a greatly expanded data base [6] and relatively fine time steps in order to achieve completeness. To create such a data base required the estimation of many cross sections. The new emergence of tungsten as a potential activation-limited element is presented here primarily to illustrate why additional calculations were deemed necessary. The next step with tungsten, and several other elements, is to review the relevant nuclear data and perform evaluations where necessary, then recalculate the activation. The estimated disposal limit will also be reviewed prior to proposing any new composition restrictions.

It is important at present that composition limits such as those in Table 1 be used only as guidelines in selecting candidate materials for study.[7] The limits depend, of course, on the assumed component lifetime. The actual concentration of radioactivity at the time of disposal will depend on the dilution that results from the manner of decommissioning. (On the other hand, dilution is not a panacea because the total volume of waste may become unacceptable.) Furthermore, the field of low level waste disposal is in a state of evolution. For example, simple near-surface burial in trenches is yielding to engineered structures, hence acceptable concentrations, particularly of activated metals, may change. And of course there are widely differing opinions on what the public perception of radwastes will be in the next century.

The approach in the U.S., therefore, is to develop the data base necessary for future decisions. This includes evaluating the potential for reducing the activation of materials through elemental tailoring, isotopic tailoring, and impurity control.

5.3 Reduced Activation Alloy Studies

The fusion reactor structure that will achieve the highest level of radioactivity is the inner blanket region, especially the first wall. Therefore initial efforts at reducing activation are on potential first wall alloys. The straightforward approach being taken is to try to replace the problem elements with more benign elements in those structural alloys for which there is an extensive data base. These are the austenitic steels such as Ti-modified **316,** the ferriticlmartensitic steels containing 9-12% Cr, and the lower Cr ferritic/bainitic steels. A parallel effort is the examination of the intrinsically low activation vanadium alloys.

5.3.1 Reduced Activation Austenitics

In the austenitics, the immediate objective is to decrease the major constituent nickel to, at most, a minor constituent. There is a considerable commercial history of replacing nickel with manganese in stainless steels in order to conserve nickel. Since Mn is only about half as effective as Ni in stabilizing the FCC austenite phase, it is necessary to compensate by increasing the concentration of other stabilizers such as N or C. Nitrogen is by far the most effective solute strengthener, inhibits the formation of delta ferrite, and strongly depresses the martensite transition temperature. The substitution of Mn for Ni increases the solubility of N in austenite, thus making possible the development of high-nitrogen steels with enhanced strength such as the AISI 200 series stainless steels. Steels based on the 200 series have been developed that have good strength and toughness at cryogenic temperatures. Similar properties can be achieved in low nitrogen steels if the Cr concentration is reduced to a few percent and the C concentration increased. These materials find application as structural components in superconducting magnets and a good technological base exists for melting, fabricating, machining and welding these high Mn alloys. [8]

The commercial Mn steels do not necessarily provide a sound basis for the development of low activation alloys. They were not designed for phase stability and mechanical strength at elevated temperatures. The nitrogen levels of most of them considerably exceed the current guidelines. Furthermore, in the lower nitrogen alloys, the Cr concentration is too low to confer adequate corrosion resistance. Nevertheless. in order to provide some insiaht into the radiation resoonse of these steels, a limited number of commercial alloys (see Table 2) ire being irradiated in the FFTF. Swelling, hardening and ductility measurements will be made on TEM disk specimens.

The possibility of developing a new set of Mn steels for first wall and blanket applications is being explored in the U.S. fusion materials program. A strategy for the development of low activation austenitics has been described by Klueh and Bloom.[9] Existing phase diagrams and the Schaeffler diagram provide the initial basis for selecting compositions in a stable austenite region. This leads to Cr concentrations ranging from 10 to 20 %, Mn from 15 *to* 20 % and C from 0.1 to 0.4 % (allowing for the considerable uncertainty in the multiplying factor for Mn). The first step is to find compositions that remain austenitic after cold working or aging to 800°C. This will be followed by appropriate alloying to eliminate unwanted intermetallic phases and to promote strengthening through carbide and phosphide dispersions.

TABLE 2
COMPOSITION OF COMMERCIAL Fe-Cr-Mn AUSTENITIC STAINLESS STEELS (WT%)

Designation	Vendor	Cr	Mn	Ni	Si	Mo	Cu	Al	N	C	P
Nitronic 32	ARMCO	18	12	1.5	0.6	0.2	0.2	--	0.4	0.1	0.02
18/18 Plux	CARTECH	18	18	0.5	0.6	1.1	1.0	--	0.4	0.1	0.02
ARCR 0033	CREUSOT-MARREL	10	18	0.7	0.6	--	--	--	0.6	0.2	--
EP-838	U.S.S.R.	12	14	4.2	0.4	0.9	0.1	0.7		0.02	--
NMF-3	CREUSOT-MARREL	4	19	0.2	0.7	--	--	--	0.09	0.60	0.02
Nonmagne 30	KOBE	2	14	2.0	0.3	--	--	--	0.02	0.60	0.02

In parallel with this work on the physical metallurgy of the Fe-Cr-Mn-C system, the compositional dependence of swelling in the Fe-Cr-Hn system is being investigated by Garner et al.[10] It is well established that maximum swelling resistance, characterized by a long incubation period, is exhibited in the Fe-Cr-Ni system for Ni in the 35-45 % range and Cr held below 15 %., i.e., the Invar region in which many physical properties exhibit anomalous behavior. Since Fe-Cr-Mn also exhibits anomalous properties at 35 % Mn, the composition range from 15 to 35 % Hn is being explored. Early results from irradiations in FFTF indicate that this system is prone to phase instabilities not observed in the corresponding Fe-Cr-Ni system. Density changes depend only weakly on composition and appear to be due to ferrite formation and segregation-induced changes in the lattice parameter, as well as void swelling.

Some exploratory irradiations are in progress to determine the effects of various solutes on the swelling resistance.[11]

A major impediment to the successful development of manganese steels for fusion applications may be the ease with which Mn is transported across surfaces. The high evaporation rate at 600°C has frustrated the performance of heavy-ion irradiations of Fe-Cr-Mn alloys. Corrosion studies on these alloys indicate high transport rates of Mn into liquid metals.[12]

The prospects for developing reduced-activation austenitic steels are still very uncertain. Substantial progress has been made in defining a region in the Fe-Cr-Mn-C system within which the austenite phase is stable under cold working or short-term aging at 800°C.[13] Such a region would provide a promising basis for an alloy with swelling resistance and mechanical properties at least equivalent to the current nickel-bearing PCA. On the other hand, no intrinsically low-swelling region has been found for the Fe-Cr-Hn system. The substitution of Mn for Ni increases corrosion rates in liquid metals, thus narrowing the temperature range of application. The effects of the substitution on corrosion rates in water are unknown to the authors.

5.3.2 Reduced Activation Ferritic/Martensitic/Bainitic Steels

The bainitic and martensitic steels containing between 2-1/2 and 12 wt% Cr possess some distinct advantages over the austenitic stainless steels, such as their excellent resistance to void swelling, lower corrosion rates in liquid metals and higher thermal stress resistance. A further advantage is that a much greater range of metallurgical options is available for trying to achieve well balanced compositions exhibiting reduced activation. As with the austenitics, the initial approach is to develop alloys which do not rely on the presence of Cu, N, Ni, Nb or Mo for their engineering properties. Neither Cu nor N are essential elements. Although small amounts of Ni (-0.5 wt%) are sometimes used to eliminate delta-ferrite in high Cr steels, other elements such as Mn or C can be used. Niobium is an important ingredient of at least one ferritic steel (Mod 9Cr-1Mo Nb-V), but its function could possibly be served by Ta or Ti. The main challenge facing the alloy designer is to replace Mo satisfactorily. It is an important element in that it confers hardenability and strengthening, both from solid solution effects and from carbide precipitation. Fortunately, both V and W are potential substitutes for Mo -- both elements are carbide formers and both restrict the gamma-phase field. However, there are significant differences between W and V in their influence on hardenability, their effectiveness as ferrite stabilizers, their role in carbide forming reactions, and their diffusivity. And, as noted earlier, W may be less benign radioactively than previously thought.

The emphasis in the U.S. Fusion Materials Program is on HT-9 (12% Cr), reflecting in part the extensive irradiation experience gained with this alloy in the Liquid Metal Reactor Cladding and Duct Program. However, for fusion applications, it is not clear that Cr contents as high as 12 wt% are necessary; indeed, lower Cr steels may well have some attractive properties such as lower DBTTs and better weldability. Consequently, the U.S. program to develop reduced activation materials encompasses a wide composition field. Chromium contents ranging from 2-112 to 12 wt% are being explored. producing structures ranging from fully bainitic to fully martensitic, including duplex ferrite-containing structures. A central thrust of the program is to explore the metallurgy of both bainitic (2-112 wt% Cr) and martensitic (9 wt% Cr) steels in which a) vanadium is varied between 0.25 and 1.5 wt%, and b) vanadium is fixed at 0.25 wt% while tungsten is varied between 1.0 and 2.5 wt%. In the 12 wt% Cr class, vanadium is also fixed at 0.25 wt% and tungsten varied between 1.0 and 2.5 wt%; Mn concentrations up to 6.0 wt% are required to suppress delta-ferrite formation.

The current program seeks to develop alloys analogous to the commercial 2-1/4 Cr - 1Mo, 9Cr - 1Mo VN-b and 12Cr-1Mo W-V in terms of tensile properties, DBTT characteristics and long-term thermal stability. The work is at an early stage. Based upon tempering and microstructural studies, an initial survey of tensile properties, and some data on the effects of low dose neutron irradiation on precipitation strengthening, several alloys at each Cr level have been identified with properties approaching those of the corresponding Mo-bearing conventional alloys. The current status of these efforts is reviewed by Klueh, Gelles, and Lechtenberg.[14] From these initial results, the prospects appear to be favorable for the development of bainitic/martensitic steels that do not rely on the presence of Cu, Ni, Mo, Nb or N for their properties.

Once the initial series of optimizations is complete and a firm metallurgical basis established, larger heats of material will be obtained to address the areas of weldability, corrosion behavior and

radiation response in parallel. The correction of serious problems in any one of these areas will probably affect performance in the other two. As for radiation effects, swelling is unlikely to be a major problem, but the effects of radiation on hardening at temperatures <450°C and on segregation and precipitation at higher temperatures may be significant. These phenomena can lead to major changes in fracture mode and to reductions in toughness. Other important phenomena are thermal and radiation-enhanced coarsening of the microstructure leading to significant reductions in creep strength. At present, our limited understanding of these phenomena can only provide minimal guidance in developing radiation damage-resistant compositions and microstructures. The successful develooment of reduced activation alloys depends heavily on current efforts to relate property changes to composition and microstructure in the conventional alloys.

The effects of helium on the performance of ferritic steels is largely unknown. This area is being approached by using Ni-doping, including isotopic tailoring, to generate helium during HFIR irradiations in order to study the effects of helium on void swelling, tensile and Charpy impact properties.[15,16] The isotopes ^{58}Ni and ^{59}Ni are utilized to produce helium and the isotope ^{60}Ni (which does not produce helium) is used for control purposes. If this work shows that conventional ferritic steels are susceptible to helium effects, then similar strategies for exploring helium effects will have to be applied to the reduced activation steels.

5.3.3 Vanadium Alloys

From the point of view of reduced activation, alloys systems based on vanadium have a distinct advantage over the ferritic and austenitic steels. Useful alloys already exist based upon ternary and binary systems of V with Cr, Ti and Si -- all elements that have favorable activation characteristics with respect to waste requirements, hence need not be replaced. The major problem is with impurity control, particularly with regard to Nb, which must be restricted to levels of the order of 1 appm. (This restriction applies equally, of course, to ferritic and austenitic stainless steels.)

Vanadium alloys have several other advantages over stainless steels. The higher thermal conductivity and lower thermal expansion coefficient allows vanadium alloys to accommodate higher thermal heat fluxes. The tensile and creep strengths of vanadium alloys are retained at much higher temperatures and offer the potential for operation at temperatures in the region of 700°C. In common with many BCC materials, vanadium alloys possess good resistance to void swelling. Finally, nuclear heating and hydrogen and helium generation rates are all substantially lower than in stainless steels.

The U.S. program is currently devoting some 15-20% of its alloy development efforts to explore further the potential advantages of the vanadium alloys. Useful data exists on alloys that were studied during the 1960's for breeder reactor applications; these alloys, V-15Cr-5Ti, V-20Ti, VANSTAR 7, together with V-3Ti-1Si (developed by KFK Karlsruhe), form the starting point of the current program. Because of limited resources, four main areas are receiving attention: a) the effects of neutron irradiation on tensile and swelling properties, b) corrosion and interstitial mass transfer in Li and Pb-Li, c) the influence of C, N, O and S on mechanical properties, and d) ion-irradiation studies to explore the effects of various interstitial and substitutional solutes, and helium, on microstructural evolution and swelling. Because vanadium alloys have potential advantages for application in high heat flux components, some effort is also being devoted to water corrosion studies.

Recent radiation effects studies of vanadium alloys have benefited from several improvements in technique. The encapsulation of vanadium alloys in lithium-filled TZM capsules has been shown to prevent the pick-up of interstitial elements C and N at temperatures up to 750°C. The application of the "tritium trick" [17] has allowed limited studies of helium effects in vanadium alloys. Temperature-controlled facilities in FFTFIMOTA, which can achieve 30 dpa per year at temperatures >390°C, have been utilized. The exploration of radiation effects at low temperature and low doses will require the use of the spectrally-tailored facilities which are now being planned for the HFIR RB* positions.[18] Recent results from the irradiation program are reviewed by Braski.[19] Measurements at neutron doses up to 40 dpa, both with and without helium, have confirmed the swelling resistance of three of the four alloys (VANSTAR 7 is the exception).

Two potential areas of irradiation embrittlement have been identified. Post-irradiation tensile testing showed that one of the alloys, V-15Cr-5Ti, was susceptible to a brittle, cleavage-type failure at ~400°C following irradiation to 10 dpa. A second type of low ductility failure, helium-assisted intergranular embrittlement, was observed in the same alloy following irradiation to 40 dpa at temperatures >500°C. No indications of these phenomena were observed in the V-20Ti and V-3Ti-1Si alloys which remained ductile at all temperatures. However, VANSTAR 7 showed signs of both phenomena at 520°C. Clearly it is important to understand the embrittlement mechanisms and to determine which regions of the V-Cr-Ti composition space are susceptible to them. Impurity content and thermo-mechanical treatments are also important variables yet to be studied. The ductile behavior of the V-20Ti and V-3Ti-1Si alloys at 40 dpa is very encouraging and indicates that embrittlement phenomena can be delayed to higher fluences or even eliminated through manipulation of alloy composition.

Corrosion measurements in both capsules and in forced circulation loops have demonstrated the resistance of vanadium to both dissolution and penetration by Li. However, a major concern regarding the applicability of vanadium alloys in fusion systems centers on the mass transfer of the elements C and Ni in a bi-metallic system. (Oxygen is not considered to be a potential source of embrittlement since it tends to transfer from vanacium into the lithium.] C and N levels of the order of 2000-4000 appm can raise the DBTT for vanadium up to room temperature. Furthermore, corrosion rates can be increased by the formation of non-adherent carbide or nitride layers. Present indications are that, in order to maintain adequate corrosion performance and mechanical integrity, C and N concentrations in a Li coolant would have to be maintained at levels on the order of 5-10 appm. Current experiments are aimed at obtaining more information on the thermodynamics and kinetics of interstitial mass transfer, the influence of coolant velocity and temperature gradient, and on effects related to alloy composition. Work is also in progress on corrosion effects in Pb-17Li.

Corrosion studies in pressurized water at 288°C indicate that, provided the Cr content is high enough to allow the formation of a passive oxide layer, corrosion rates are sufficiently low for vanadium alloys to be utilized in water-cooled components.[20]

Many areas of vanadium alloy metallurgy remain *to* be examined, e.g. fabrication and welding, hydrogen compatibility, crack growth, creep-rupture, irradiation creep and radiation effects at temperatures <400°C. It is clear already that none of the four principal alloys has the optimum combination of properties needed to meet the varied requirements of the fusion first wall and blanket environment. In this regard, a review of the effects of substitutional solutes and interstitial impurities on the mechanical properties of vanadium alloys, and of possible new directions for alloy development, has been prepared by Diercks and Loomis.[21] The prospects appear favorable for producing alloys with good swelling resistance, superior high strength and adequate toughness, from starting stock with adequate control of Nb impurity to meet the requirements for near-surface burial. Impurity control during fabrication and welding will pose problems which can probably be overcome with current technology. The major objection to the use of vanadium is the difficulty of preventing contamination by interstitial mass transfer in liquid metal systems. This problem could possibly be alleviated *to* some extent through alloy development. However, the principal solution to the problem lies in developing an adequate impurity control system, a situation somewhat analogous to that facing the breeder program in the 1960's in regard to controlling oxygen levels in large sodium systems.

5.4 Conclusions

Studies of low activation alloys are at an early stage in the US fusion materials program. Emphasis is on understanding the necessary elemental tailoring of commercial iron-based alloys and on building a foundation of knowledge of vanadium alloys.

The only low activation substitute for Ni in the austenitic steels identified to date is Mn. The high mobility of this, element suggests that Mn steels, in the absence of protective coatings, will be more restricted in their application than the nickel-bearing steels.

The prospects are favorable for a reduced activation ferriticlmartensitic alloy that is as good as the current leading "high-activation" candidates. However, little is known about how these alloys will respond to high helium levels. Early data on HT-9 shows that voids are nucleated in the presence of high helium production rates. A further potential complication is that tungsten may prove to be an unsatisfactory substitute for Mo, although vanadium may be used instead.

The vanadium alloys perhaps remain the most attractive for the long term, particularly if the current view that the Nb impurity can be adequately controlled is correct. This apparent attractiveness may diminish, of course, as the slim data base is expanded.

Only when the current scoping studies are further advanced and actual alloy design has begun will it be necessary to firm up the guidelines on compositional limits. In the meantime, more information is needed to make the guidelines meaningful. This includes reactor decommissioning scenarios, including waste management and recycling, and classifications for and limitations on waste disposal that will be applicable in the future.

5.5 Acknowledgments

The authors gratefully acknowledge assistance with this overview from numerous ICFRM-2 authors in advance of the conference. This work was sponsored by the U.S. Department of Energy.

6.0 References

1. R. W. Conn, et al. "Report of the DOE Panel on Low Activation Materials for Fusion Applications," UCLA School of Engineering and Applied Sciences Report, UCLA/PPG-728, June 1983.

2. See, for example, O. N. Jarvis, "Low Activity Materials: Reuse and Disposal," Harwell Report AERE-10860, July 1983.

3. W. E. Kennedy, Jr., and F. M. Mann, Trans. Am. Nucl. Soc. 45 (1983) 51.

4. F. M. Mann, Fusion Technol. 6 (1984) 273.

5. H. L. Heinisch, F. M. Mann, and D. G. Doran, Fusion Technol. 8 (1985) 2704.

6. F. M. Mann, O. E. Lessor, and J. S. Pintler, "REAC Nuclear Data Libraries," in Proc. Intl. Conf. Nuclear Data for Pure and Applied Sciences, Sante Fe, NM, 1985 (to be published in Radiation Effects).

7. D. G. Doran, H. L. Heinisch, and F. M. Mann, J. Nucl. Mat. 133 and 134 (1985) 892.

8. *See* the proceedings *of* the International Cryogenic Materials Conference, Colorado Springs, CO, U.S.A., August 15-19, 1983.

9. R. L. Klueh and E. E. Rloom, "Alloy Development for Fast Induced-Radioactivity Decay for Fusion Reactor Applications," ADIP Semiannual Progress Report, DOE/ER/0045/1 (1983) 11-20.

10. F. A. Garner, H. R. Brager, D. S. Gelles, and J. M. McCarthy, "Comparative Neutron Irradiation of Simple Fe-Mn, Fe-Cr-Mn and Fe-Cr-Ni Alloys," Proceedings of the Second International Conference on Fusion Reactor Materials, to be published in J. Nucl. Mat., 1986.

11. H. R. Brager, "High Fluence Neutron Irradiation of Commercial and Developmental Fe-Cr-Mn Austenitic Alloys for Reduced Activation Materials," Proceedings of the Second International Conference on Fusion Reactor Materials, to be published in J. Nucl. Mat., 1986.

12. P. F. Tortorelli and G. H. DeVan, "Corrosion of Fe-Cr-Mn Alloys in Thermally Convective Lithium," Proceedings of the Second International Conference on Fusion Reactor Materials. to be published in J. Nucl. Mat., 1986.

13. P. J. Maziasz and R. L. Klueh, "Phase Stability During Annealing and Aging in Low Activation Fe-Cr-Mn Austenitic Stainless Steels," ADIP Semi-Annual Progress Report DOE/ER-0045/15 (Sept. 1985) 54-60.

14. R. L. Klueh, D. Gelles, and T. Lechtenberg, "Development of Ferritic Steels for Reduced Activation: The U.S. Program," Proceedings of the Second International Conference on Fusion Reactor Materials, to be published in J. Nucl. Mat., 1986.

15. R. L. Klueh, P. J. Maziasz, and J. M. Vitek, "Post-Irradiation Tensile Behavior of Ni-Doped Ferritic Steels," Proceedings of the Second International Conference on Fusion Reactor Materials, to be published in J. Nucl. Mat., 1986.

16. P. J. Maziasz, R. L. Klueh, and J. M. Vitek, "Void Formation in Ni Doped and Un-Doped Ferritic Steels Irradiated in HFIR," Proceedings of the Second International Conference on Fusion Reactor Materials, to be published in J. Nucl. Mat., 1986.

17. D. N. Braski and D. W. Ramey, in ADIP Semi-Annual Progress Report, (Mar. 31, 1984) DOE/ER-0045/12.

18. C. D. West, "HFIR Irradiation Facilities Improvements - The MIFI Project," Proceedings of the Second International Conference on Fusion Reactor Materials, to be published in J. Nucl. Mat., 1986.

19. D. N. Braski, "The Effects of Neutron Irradiation on Vanadium Alloys," Proceedings of the Second International Conference on Fusion Reactor Materials, to be published in J. Nucl. Mat., 1986.

20. D. R. Diercks and D. L. Smith, "Corrosion Behavior of Vanadium-Based Alloys in Pressurized Water at 288°C," Proceedings of the Second International Conference on Fusion Reactor Materials, to be published in J. Nucl. Mat., 1986.

21. D. R. Oiercks and B. A. Loomis, "Alloying and Impurity Effects in Vanadium-Base Alloys," Proceedings of the Second International Conference on Fusion Reactor Materials, to be published in J. Nucl. Hat., 1986.

SWELLING OF Fe-Mn AND Fe-Cr-Mn ALLOYS AT HIGH NEUTRON FLUENCE

F. A. Garner and H. R. Brager (Hanford Engineering Development Laboratory)

1.0 Objective

The object of this effort is to assess the suitability of austenitic Fe-Cr-Mn alloys as low activation candidates for fusion reactor materials.

2.0 Summary

Swelling data on neutron-irradiated simple Fe-Cr-Mn and Fe-Mn alloys, as well as commercial Fe-Cr-Mn base alloys are now becoming available at exposure levels approaching 50 dpa. The swelling rate decreases from the ~1%/dpa found at lower exposures, probably due to the extensive formation of ferritic phases. As expected, commercial alloys swell less than the simple alloys.

3.0 Program

Title: Irradiation Effects Analysis
Principal Investigator: D. G. Doran
Affiliation: Hanford Engineering Development Lahoratory

4.0 Relevant OAFS Program Plan Task/Subtask

Subtask II.C.1. Effect of Material Parameters on Microstructure

5.0 Accomplishments and Status

5.1 Introduction

In an earlier report[1] it was shown that Fe-Mn binary and Fe-Cr-Mn ternary alloys appear to swell in a temperature-independent fashion at ~1%/dpa after an incubation period on the order of 10 dpa. (See Fiaure 1a). Thus the behavior of these alloys is similar to that of the Fe-Cr-Ni system[2]. It was also shown, however, that unlike the Fe-Cr-Ni system the Fe-Cr-Mn system is much more prone to phase separation, producing a large amount of ferrite as the irradiation proceeds.

One consequence of such a behavior is a reduction in the austenite fraction of the alloy matrix, leading inevitably to a reduction in bulk-averaged swelling rate as the lower swelling ferrite phase increases in volume. Density change data from the FFTF-MOTA irradiation program are now available at 49.8 dpa and 520°C for most of the binary and ternary alloys and most of the commercial alloys. Some very limited data are also available at 420°C and 46 dpa for the simple alloys.

5.2 Results at 520°C

Figure 1b confirms our expectation that at least at 520°C the swelling rate will fall as the irradiation proceeds in the range 14 to 49.8 dpa. The resulting tendency toward saturation appears to increase for a given manganese level as the chromium level decreases. We have not as yet shown that the ferrite fraction increases in this exposure interval however.

Figure 1 also shows that reductions in swelling can be accomplished via solute modification and/or thermal mechanical treatment; commercial alloy AMCR 0033 is shown as an example. Swelling data for the other commercial alloys at 49.8 dpa is given in Table I.

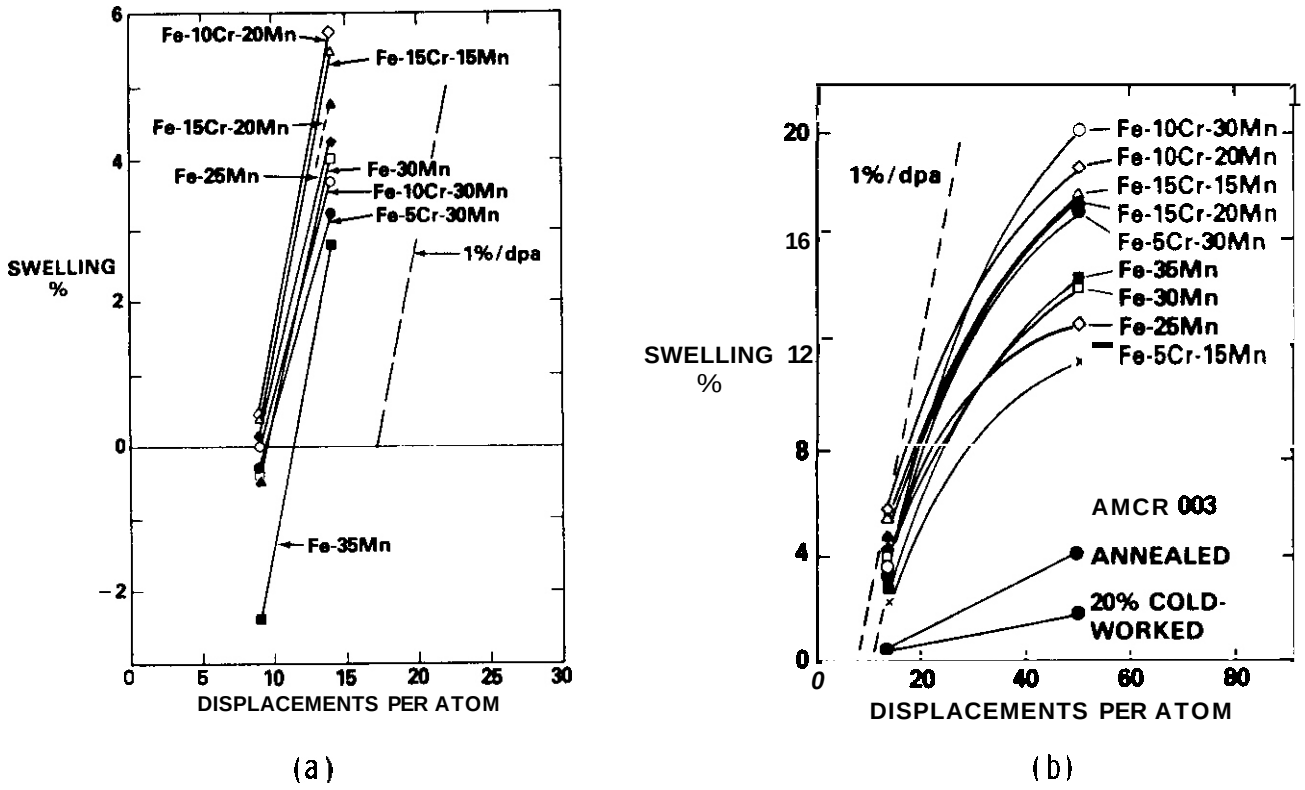

FIGURE 1. (a) Swelling at 9-14 dpa of Fe-Cr-Mn and Fe-Mn alloys at 420 and 520°C in FFTF-MOTA, (b) Swelling of these alloys at 520°C and higher fluence. The swelling of commercial alloy AMCR 003 is also shown for comparison.

Table I. Swelling of Commercial Alloys at 49.8 dpa and 520°C

Alloy	Condition	Swelling
Nitronic 32	CW	3.5
18/18 Plus	CW	2.2
AMCR 0033	CW	1.9
AMCR 0033	CWA	2.5
AMCR 0033	SAA	4.4
NMF 3	CW	0.1
NONMAG 30	CW	1.0
NONMAG 30	CWA	0.42
NONMAG 30	SAA	2.87

CW = cold-worked
CWA = cold-worked and aged
SAA = solution annealed and aged

5.3 Results at 420°C and 46 dpa

At present, data on the complete set of simple alloys are available only at 9 dpa.[3] At 46 dpa we now have swelling data for annealed Fe-10Cr-20Mn (5.8%) and Fe-15Cr-15Mn (3.2%). At 9 dpa the corresponding values were 0.4% and 0.3% respectively. It therefore appears that at 420°C the saturation of swelling occurs even more quickly than at 520°C. In this case, we must consider the additional possibility that a martensitic transformation may have occurred. This possibility will be explored during the next reporting period.

5.4 Conclusions

Fe-Cr-Mn alloys are subject to phase decomposition during neutron irradiation, producing large fractions of ferrite phases. The reduction of the austenite fraction is thought to cause a decrease in the bulk swelling rate. Commercial alloys were found to swell less than simple Fe-Mn binary and Fe-Cr-Mn ternary alloys.

6.0 References

1. F. A. Garner, O. S. Gelles, H. R. Brager and J. M. McCarthy, DAFS Quarterly Progress Report DOE/ER-0046/24, pp. 22-29.

2. F. A. Garner, J. Nucl. Mater., 122 & 123 (1984) pp. 459-471.

3. F. A. Garner, H. R. Brager, O. S. Gelles and J. M. McCarthy, "Neutron Irradiation of Fe-Mn, Fe-Cr-Mn and Fe-Cr-Ni Alloys and an Explanation of Their Differences in Swelling Behavior," to be published in J. Nuclear Materials, also HEDL-SA-3403.

7.0 Future Work

Density change data will continue to be collected and microscopy will proceed on selected specimens.

8.0 Publications

F. A. Garner, H. R. Brager, O. S. Gelles and J. M. McCarthy, "Neutron Irradiation of Fe-Mn, Fe-Cr-Mn and Fe-Cr-Ni Alloys and an Explanation of Their Differences in Swelling Behavior," to be published in J. Nuclear Materials, also HEDL-SA-3403.

ELECTRON IRRADIATION STUDIES OF Fe-Cr-Mn AND Fe-Cr-Ni ALLOYS

H. Takahashi, H. Itoh and S. Ohnuki (Hokkaido University)
F. A. Garner (Hanford Engineering Development Laboratory)
B. Hu (Beijing University of Iron and Steel Technology)

1.0 Objective

The object of this effort is to utilize both HVEM and neutron irradiation to characterize the response of Fe-Cr-Mn alloys in anticipated fusion environments.

2.0 *Summary*

Study of the elemental segregation that occurs at grain boundaries during electron irradiation confirms that iron and chromium segregate at microstructural sinks in Fe-Cr-Mn alloys while nickel segregates in Fe-Cr-Ni alloys. This accounts partially for the difference in phase stability in the two alloy systems. An example is shown that indicates that solute additions can be used to suppress the segregation process.

3.0 Program

Title: Irradiation Effects Analysis
Principal Investigator: D. G. Doran
Affiliation: Hanford Engineering Development Laboratory

4.0 Relevant DAFS Program Plan Task/Subtask

Subtask II.C.1. Effect of Material Parameters on Microstructure

5.0 Accomplishments and Status

5.1 Introduction

A joint study involving Hokkaido University and Hanford Engineering Development Laboratory is currently in progress and involves the use of HVEM irradiation to study the microstructural evolution of Fe-Cr-Mn alloys. The first results of these studies will be published shortly and involves not only information on the compositional dependence of swelling and microstructural development but also on the helium dependence of these processes.

In addition, however, these studies concentrate on the segregation behavior of these alloys. A feature of these studies is therefore the conduct of irradiations that straddle a grain boundary. Examination of the elemental profiles that develop near grain boundaries then supplies valuable information on the role of various elements in the diffusion processes involved in void growth, irradiation creep and phase stability.

Our interest in the segregation behavior has been increased recently with the realization that Fe-Cr-Mn alloys tend to decompose into ferrite and retained austenite in a manner which suggests that iron is the slowest diffusing element in Fe-Cr-Mn simple ternary austenitic alloys.[1] In Fe-Cr-Ni alloys nickel is known to be the slowest diffusing component but is also known to increase the effective vacancy diffusivity when its concentration is raised.[2]

In this report the results of segregation studies are presented which confirm that while manganese can be substituted for nickel to stabilize iron-based austenitic alloys, its effects on diffusion and segregation are different from those of nickel.

5.2 Experimental Details

Electron irradiations were performed at 1000 KeV in the H-1300 H_VEM at Hokkaido University. The mean dose rate in the center of the irradiated area was $\sim 2 \times 10^{-3}$ dpa sec^{-1} and the maximum dose was 15 dpa. The temperature range studied was 573-773K. For the segregation portion of the study a grain boundary viewed edge-on was selected to traverse the irradiated area.

The elemental composition were measured using a 200 KeV TEM/STEM electron microscope equipped with an energy dispersive x-ray spectroscope. The compositions were determined from the intensities of the $K\alpha$ x-rays for the major elements.

In this first group of studies, three alloys were employed, the compositions of which are shown in Table I. There is one nickel-stabilized alloy (Fe-15Cr-30Ni) and two Fe-Cr-Mn alloys. The first of these is a simple ternary, Fe-15Cr-20Mn, and the second is a solute-bearing alloy Fe-15Cr-15Mn with additions of C, N, W, V, Si and P.

5.3 Results

Figures 1 and 2 show that nickel indeed segregates at grain boundaries in Fe-15Cr-30Ni, with the amount of segregation increasing with temperature. Since nickel is the slower diffusing component it would be expected to segregate via the Inverse Kirkendall mechanism.

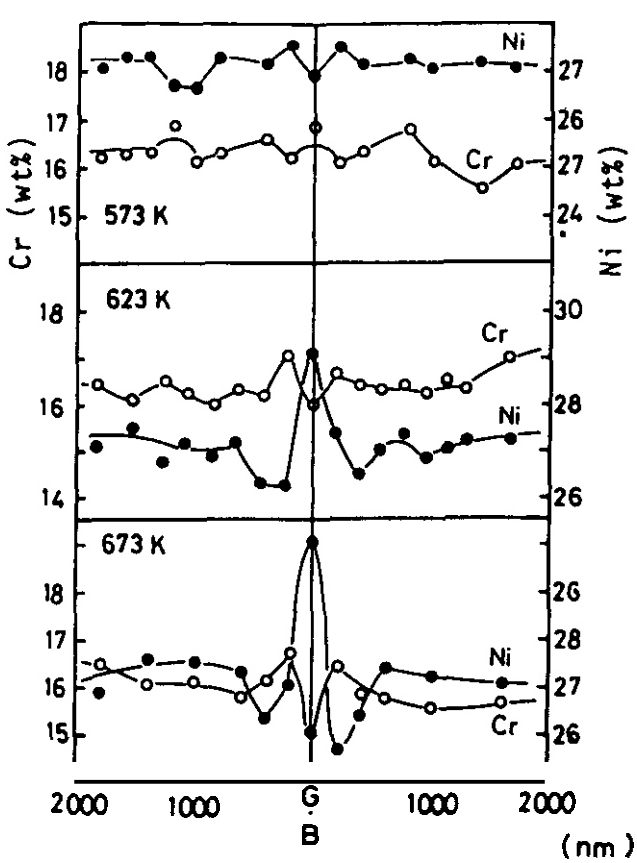

FIGURE 1. The profiles of solute (Cr,Ni) concentration as a function of distance from the grain boundary for Fe-15Cr-30Ni electron-irradiated to 15 dpa at 573-673 K.

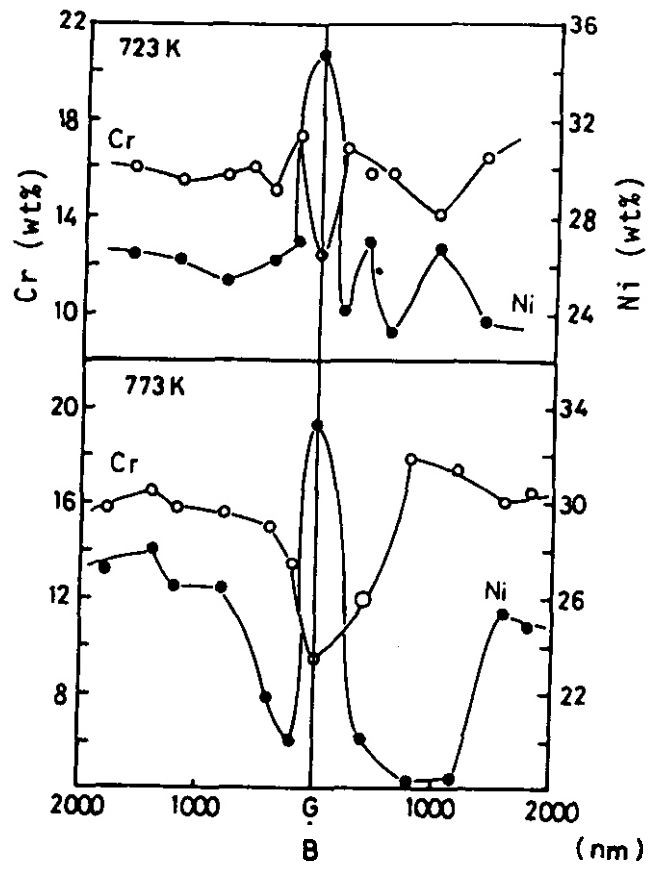

FIGURE 2. The profiles of solute (Cr,Ni) concentration as a function of distance from the grain boundary for Fe-15Cr-30Ni electron-irradiated to 15 dpa at 723-773 K.

In Fe-15Cr-20Mn, however, Mn in general flows away from the boundary, as shown in Figure 3, confirming the earlier suggestion that manganese-stabilized alloys might exhibit substantially different phase stability compared to that of nickel-stabilized alloys. Segregation of iron at the expense of manganese at microstructural sinks thus leads to extensive ferrite formation in Fe-Cr-Mn alloys.[11]

Figures 4 and 5 show that segregation in general is reduced in the solute-modified manganese alloy compared to that of the ternary manganese-stabilized alloy.

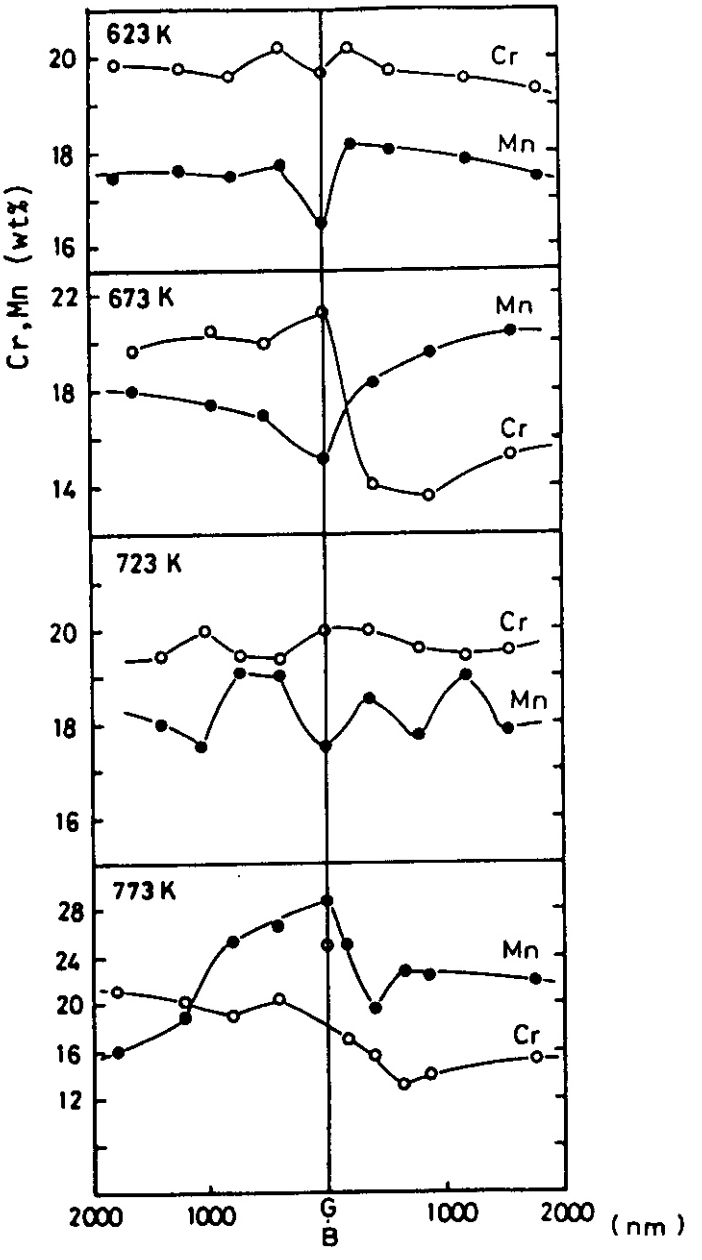

FIGURE 3. The profiles of solute (Cr,Mn) concentration as a function of distance from grain boundary for Fe-15Cr-20Mn electron-irradiated to 15 dpa at 623-773 K.

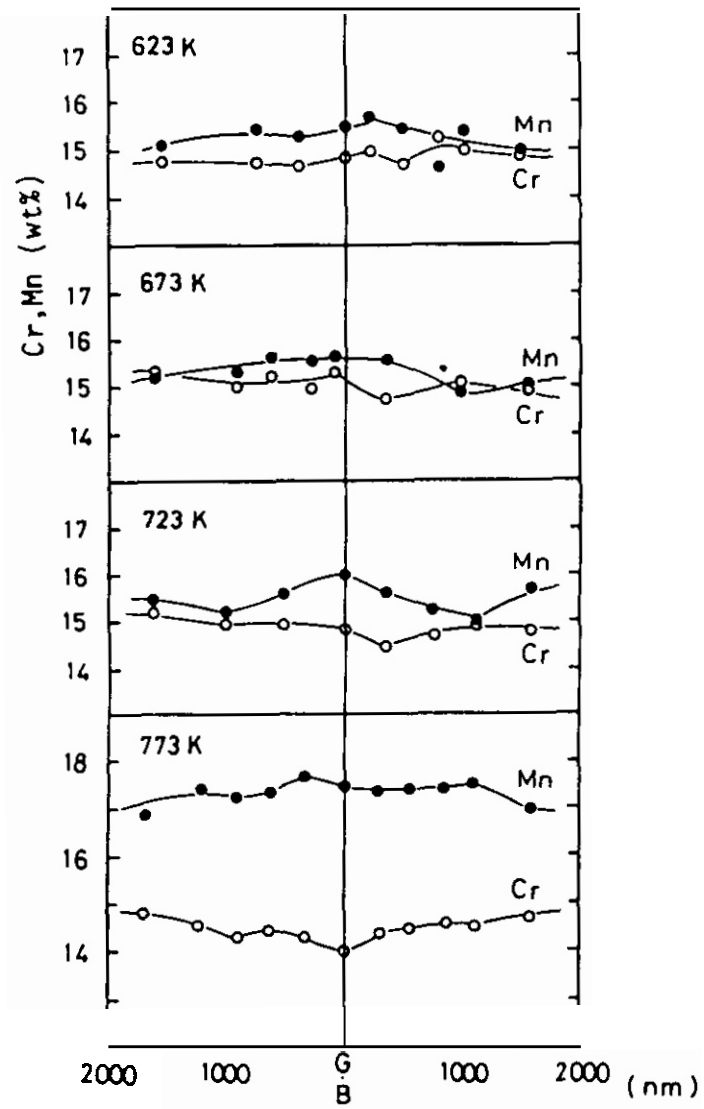

FIGURE 4. The profiles of solute (Cr,Ni) concentration as a function of distance from the grain boundary for Fe-15Cr-15Mn (W,V) electron-irradiated to 15 dpa at 623-773 K.

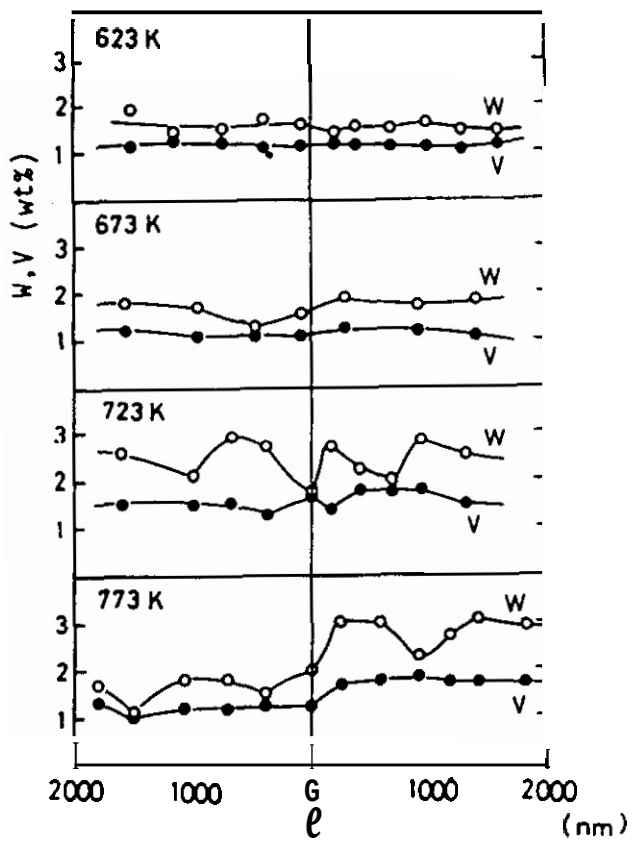

FIGURE 5. The profiles of minor alloying elements (W,V) concentration as a function of distance from the grain boundary for Fe-15Cr-15Mn(W,V) electron-irradiated at 623-773 K.

5.4 Discussion

The early results of the neutron irradiation studies[1] indicate that Fe-Cr-Mn alloys in general have a greater tendency toward phase decomposition. Part of this tendency arises from the different diffusional and segregational characteristics of nickel and manganese in iron-based austenitics. This study supports the contention that manganese and nickel flow in opposite directions along point-defect gradients generated in the vicinity of microstructural sinks. It also appears, however, that solute additions can influence this process such that some potential exists to design a viable reduced activation austenitic alloy.

5.5 Conclusions

While both manganese and nickel can be used to stabilize the austenitic phase their diffusional and segregation behaviors are different. These differences **must** be understood prior to the development of Fe-Cr-Mn alloys for fusion service.

6.0 References

1. F. A. Garner, H. R. Brager, O. 5. Gelles and J. M. McCarthy, OAFS Quarterly Report DOE/ER-0046/24, February 1986, pp. 22-29.

2. F. A. Garner and W. G. Wolfer, J. Nucl. Mater. 122&123 (1984) pp. 459-471.

7.0 Future Work

Irradiations of Fe-Cr-Mn allays with either neutrons or electrons will continue.

8.0 Publications

"The Behavior of Solute Segregation and Void Formation in Fe-Cr-Mn Steel Under Electron Irradiation" will be submitted by these authors to the 13th International Symposium on Effects of Radiation on Materials, to be held in Seattle on June 23-25, 1986.

Table 1. Compositional analysis of alloys used. (wt%)

Alloy Designation	Nominal Composition	Fe	Ni	Cr	Mn	C	O	N	W	V	Si	P
E21	Fe-15Cr-30Ni	Bal	29.6	15.3	-	0.004	0.017	0.002	-	-		-
R70	Fe-15Cr-20Mn	65	-	15	20	-	-	-	-	-	-	-
R88	Fe-15Cr-15Mn(W,V)	Bal	0.5	15	15	0.30	-	0.30	2.0	2.0	0.4	0.05

CHAPTER 4

FUNDAMENTAL MECHANICAL BEHAVIOR

MICROSTRUCTURE-MECHANICAL PROPERTY VARIATIONS IN HT-9

G. E. Lucas, R. Maiti, C. Elliott and G. R. Odette (University of California, Santa Barbara)

1.0 Objective

This research is directed at determining microstructure-property-property correlations for cleavage fracture in HT-9. Such correlations can he used to assess the potential far operating fusion reactor Structures in temperature regimes corresponding to lower shelf toughness.

2.0 Summary

Microstructure and mechanical property specimens of the ESR Heat of HT-9 were subjected to a set of heat treatments. These consisted of combinations of five austenitizing temperatures (950-1200°C) and five tempering conditions (650-780°C). The prior austenite grain (PAG) size and lath packet size were found to increase with increasing austenitization temperature. Five different carbide types were identified. They appear to be largely $M_{23}C_6$ and perhaps M_6C and Mo_2C. Large blocky carbides at PAG boundaries appeared only at low austenitization temperatures, and fine needlelike carbides in the matrix were absent at the higher tempering temperatures. Elongated lath and boundary carbides increased slightly in size at higher tempering temperatures. Lower shelf toughness showed a slight minimum at an austenitization temperature of 1050°C and increased with increasing tempering temperature and time. Yield strength, ultimate tensile strength and ductility all showed a peak for an austenitization temperature of 1050°C. Values of critical microcleavage fracture stress (σ_f^*) also showed a peak with austenitizing temperature. This may indicate a change in the controlling microstructural feature. Fracture surfaces exhibited largely cleavage facets with ductile tear ridges at PAG and lath packet boundaries. These tear ridges may contribute to the magnitude of σ_f^*.

3.0

Title: Damage Analysis and Fundamental Studies for Fusion Reactor Materials
Principal Investigators: G. R. Odette and G. E. Lucas
Affiliation: Department of Chemical and Nuclear Engineering, University of California, Santa Barbara

4.0 Relevant DAFS Program Plan Task/Subtask

Subtask II.C.14 Fracture Model Development

5.0 Accomplishments and Status

5.1 Introduction

Martensitic and duplex stainless steels are considered attractive candidate alloys for fusion reactor Structures. However, their tendency to fail by brittle cleavage fracture at low temperatures and the potential for irradiation to raise the transition temperature delineating this cleavage regime from a regime of ductile fracture have been identified as major problems to he resolved. We have previously suggested that it may be possible to operate fusion reactor structures in the cleavage fracture regime.[1] Demonstration of this requires that 1) irradiation and other environmental factors do not significantly degrade lower shelf toughness, 2) fracture occurs at stresses associated with general yield, and 3) sufficient ductility is retained.

Ensuring the irradiation insensitivity of lower shelf toughness requires understanding the basic mechanisms of cleavage fracture, at least in terms of appropriate microstructure-property relations. We have previously demonstrated[3] that the Ritchie-Knott-Rice (RKR) model for cleavage fracture[5] appeared to be consistent with the microstructure and the mechanical response of the ESR Heat of HT-9. The RKR model postulates that cleavage fracture occurs when the applied stress ahead of a sharp crack exceeds a critical stress σ_f^* over a critical distance ℓ^*. Both σ_f^* and ℓ^* appear to he sensitive only to the large scale microstructure. The work reported here is part of a subsequent effort to further verify the applicability of the RKR model for HT-9 and to develop a better understanding of the relationships between σ_f^* and ℓ^* and the microstructure.

5.2 Experimental Procedure

Standard Charpy-V-Notch specimens were cut with a TL orientation (notch parallel to the rolling direction) from HT-9 plate described elsewhere.[3] Specimens were encapsulated in quartz tubes, which were then evacuated and backfilled with helium. Five specimens each were conditioned at 25 different heat treatments. Each heat treatment consisted of austenitizing at one of 5 temperatures for 1h, air cooling, tempering at one of 5 tempering conditions, and air coaling again. Because of the encapsulation, the cooling time was slightly longer than a normal air cool (i.e. t ~ 125s for a temperature decrease from 800°C to 500°C). The five austenitizing temperatures (T_γ) were 950, 1000, 1050, 1100, and 1200°C. The five tempering conditions are shown below in Table 1.

Table 1

Tempering Conditions

Temperature, T (°C)	Time, t (h)	$P_T = T(°K)(\log t(h) + 20)$ $(x10^{-3})$
650	1	18.5
650	56	20
715	1	20
135	0.5	20
780	1	21

These were selected to provide an interesting range of tempering parameters, P_T, as well as providing a range of conditions for a single tempering parameter (P_T = 20).

Following heat treatment, small microstructural specimens were cut from the CVN specimens and examined. Prior austenite grain (PAG) sizes and lath packet sizes were determined by optical metallography. Specimens were prepared either by chemically etching with 10:5:85 $HF:HNO_3:H_2O$ or by electrolytically etching with 65:65:15:15 $H_2O:HCl:HC_2H_3O_2:HNO_3$ at 1.5-1.75 volts for 45s. Lath structure and carbides were examined by thin-foil TEM. Discs were prepared by twin jet polishing in an 8% perchloric acid-in-methanol solution at -35°C. Finally, PAG. lath packet, and lath size and carbides were examined by TEM and AEM using carbide extraction replicas and two stage surface replicas. Extraction replicas were prepared by 1) etching the surface as described above, 2) vapor depositing a layer of carbon on the surface, and 3) separating the replica from the surface in a solution of 10% HCl in methanol. Two-stage surface replicas were prepared by standard acetate tape procedures applied to an etched surface. Chromium was used to shadow the replica.

A variety of mechanical tests were applied to the heat treated CVN specimens. Rockwell hardnesses were first taken. Two CVN specimens were then fatigue pre-cracked to obtain crack length to width ratios in the range 0.45-0.55. These were tested on an instrumented pendulum machine at .79 m/s at -101°C and -112°C, and the data were analyzed to obtain dynamic fracture toughness values K_{Id} under linear elastic (lower shelf) or nearly linear elastic conditions.

One blunt notch CVN specimen was tested on the instrumented pendulum machine at room temperature; and two blunt notch CVN's, at -101°C. The room temperature data provided a measure of dynamic yield stress, and the low temperature data could be used to obtain estimates of σ_f^* (procedures are described later). For some conditions, yield stress and other flow properties were also determined from miniature round bar specimens machined from broken CVN specimen halves. The gage section diameter of these specimens was

1.52 mm, and the other dimensions were in proportion to the threaded round bar specimen described in ASTH Standard E8.

Finally, fracture surfaces were studied by SEM using stereographic techniques. In some instances, fracture surfaces were examined by an oblique sectioning technique to obtain a direct correlation between surface topography and subsurface cracking and/or microstructure. To obtain oblique section fractographs, 1) the fracture surface is coated with an acid resistant lacquer, 2) the specimen is cut on a slow speed cut-off wheel such that the sectioned surface makes an oblique angle with the fracture surface, 3) the sectioned surface is ground, polished and etched, 4) the lacquer is dissolved, and 5) the resulting specimen is examined at the fracture/section interface on an SEM.

5.3 Microstructural Results

PAG sizes were determined from optical micrographs by a combination of Hilliard's circular test procedure (ASTM Standard E112-80), the linear intercept method and direct microstructural measurements. Results obtained with different techniques were comparable. The data are shown in Fig. 1. The PAG size increases with increasing T_γ from about 25 μm at 950°C to 330 μm at 1200°C. These results are consistent with data reported by Lechtenberg and Heifrich[6] and Dobbs.[7]

Lath packet sizes (d_p) were determined largely from two stage surface replicas, and where possible from optical micrographs. The former was found to provide more reliable data. To date, lath packet-sizes have only been determined for two tempering conditions -- 650°C for lh and 780°C for lh -- over the full range of T_γ's. Typical TEM micrographs are shown in Fig. 2, and a plot of the data is given in Fig. 3. The lath packet size, like the PAG size, increases with increasing austenitizing temperature from about 10 μm at 950°C to 95 μm at 1200°C. Tempering appeared to have no effect on lath packet size. The ratio of PAG size to lath packet size is of the order 3:1 in all cases.

Lath width measurements were made largely on TEM micrographs obtained from thin foils. A representative example is shown in Fig. 4. A complete set of measurements was attempted for specimens austenitized at all temperatures and tempered at conditions of 650°C/1h, 650°C/56h and 780°C/1h. Lath width measurements were somewhat more difficult to obtain than packet sizes or PAG sizes for a variety of reasons: good thin foil images are more difficult to obtain, the laths exhibited a range of widths, and lath orientation within a given region strongly affected image quality and size. However, based on multiple measurements, it appears that lath size in all cases was of the order 0.8 μm with an average range of f0.3 μm. Hence, lath width was not strongly affected hy T or tempering conditions. Since the lath boundaries were highly decorated with carbides in all cases: it appears that lath boundary carbides largely prevent any lath coarsening during tempering for the tempering conditions investigated. Since lath packet size increases with T_γ, the number of laths per packet increases with T_γ as well.

Same carhide analysis has also been performed to date. Results have largely been obtained from inspection of carbide extraction replicas. Analyses are ongoing, so results reported here should be considered preliminary. Five general carbide types were observed, classed according to their morphology and location. Representative micrographs illustrating some of the features described below are shown in Figs. 5 and 6. Large carbides (type 1) were present largely on PAG boundaries for T_γ's of 950 and 1000°C. These large carbides were not found on PAG boundaries at higher T_γ's, but a few existed randomly at T = 1050°C. They were slightly elongated, with sizes in the range 1μm x 3.5μm. They became smaller and fewer in number at increasing T . Smaller elongated carbides (type 2) were found along PAG boundaries for all five T_γ's. These carbide% decreased slightly in size and fractional grain boundary coverage as T_γ increased. Their sizes are of the order 0.06μm x 0.2μm. Carbides an lath packet boundaries (also type 2) were smaller and hlackier than those on PAG boundaries. At T_γ = 1200°C the PAG boundary and lath packet boundary carbides were nearly the same size. Although blockier than PAG boundary carbides, the lath packet boundary carbides become more elongated with increasing T_γ. Their size was of the order 0.04μm x 0.16μm. Two types of lath carbides were present. The first type (type 3) was a coarse blocky carbide which was found throughout the material austenitized at 950°C. The number of these blocky carbides decreased rapidly with increasing T_γ. At T_γ = 1200°C, these carbides were rare. Their size was of the order 0.06μm x 0.06μm. The second type of lath carbides (type 4) were small and elongated. These carbides became smaller, more numerous, more elongated, and more strongly oriented with increasing T_γ temperature. Their sizes were approximately 0.02μm x 0.14μm at 1200°C, and 0.04μm x 0.2μ at 950°C. Finally, very small, needlelike carbides (type 5) were found distributed throughout the matrix at all T_γ's. Their sizes were on the order of 0.04μm x 0.01μm.

For a given T_γ, a number of changes in carbide characteristics occurred in going from a low (P_T = 18.5) to a high (P_T = 21) tempering parameter. Most notably, the fine, needlelike precipitates (type 5) present in the 650°C/1h tempered material (at all T_γ's) were no longer present in the 780°C/1h tempered

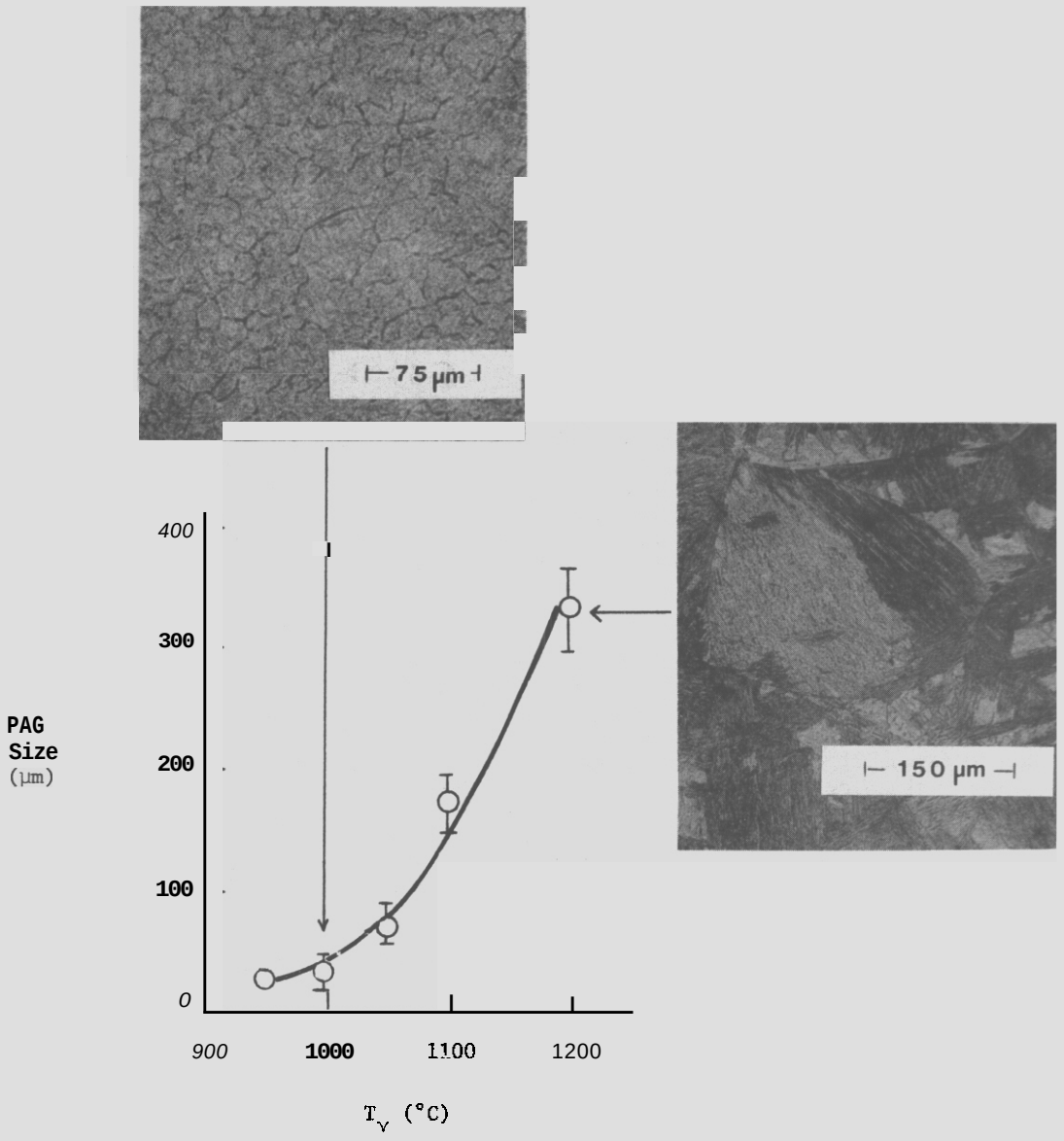

Fig. 1. Prior austenite grain size as a function of austenitizing temperature. Micrograph inserts depict the observed structure.

(b)

Fig. 2. Nepresenrarive TEM micrographs of rwo-srage surface replicas taken from rhe 650°C-1h tempered material austenitized at a) 950°C and b) 1200°C.

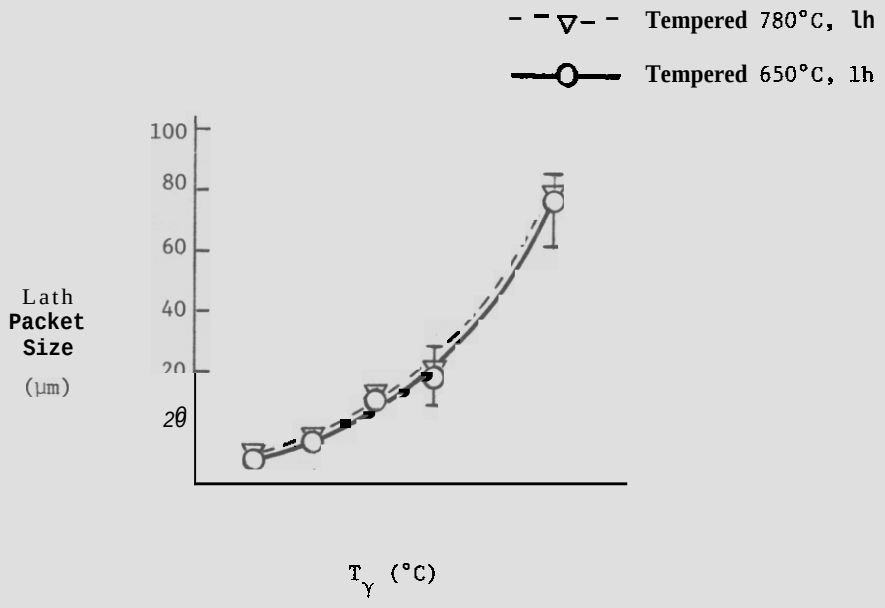

Fig. 3. Plot of the lath packet size as a function of austenitizing temperature and tempering conditions.

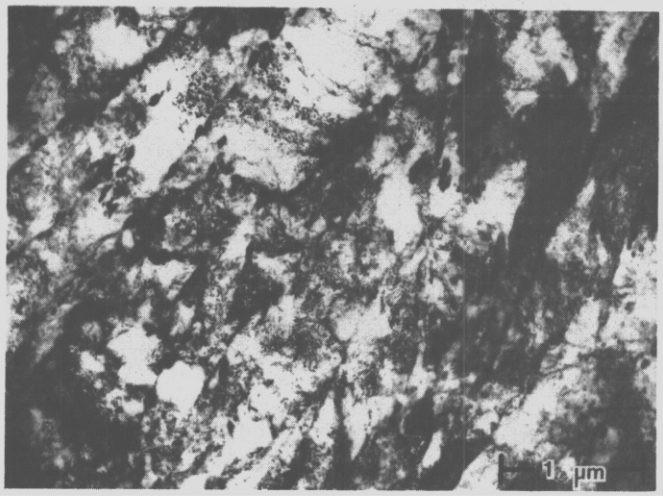

Fig. 4. Representative TEM micrograph of thin foil specimen taken from material austenitized at 1200°C and tempered 650°C for 1h.

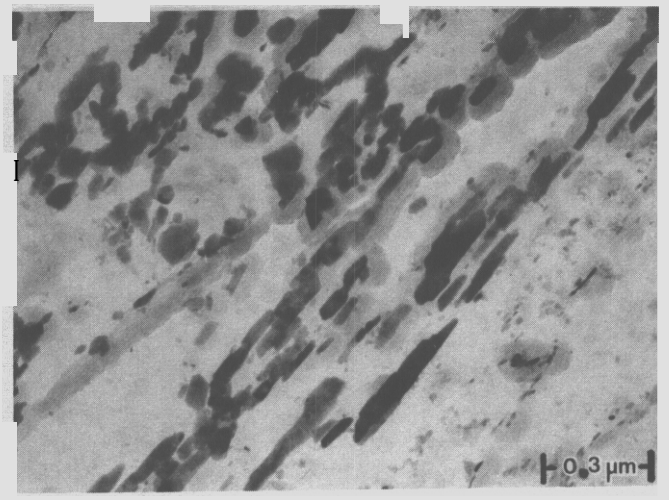

(a)

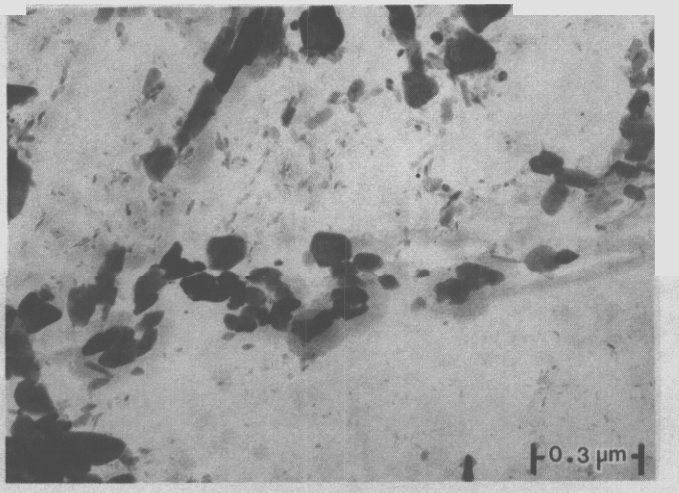

(b)

Fig. 5. Representative TEM micrographs of carbide extraction replicas illustrating a) elongated, b) blocky carbides at lath and lath packet boundaries in material austenitized at 950°C and tempered at 650°C for 1h.

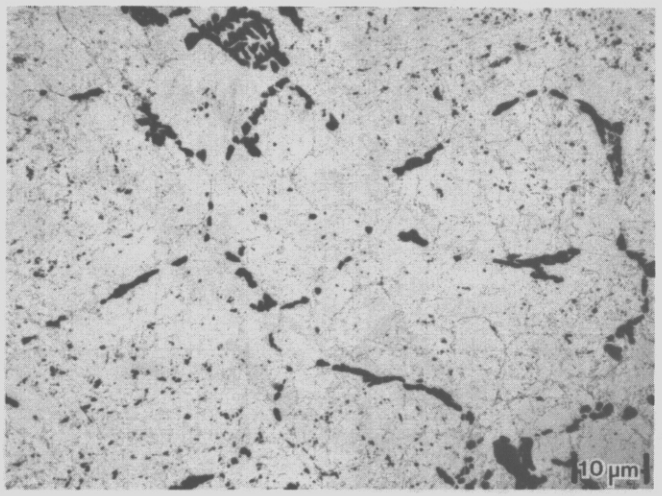

(a)

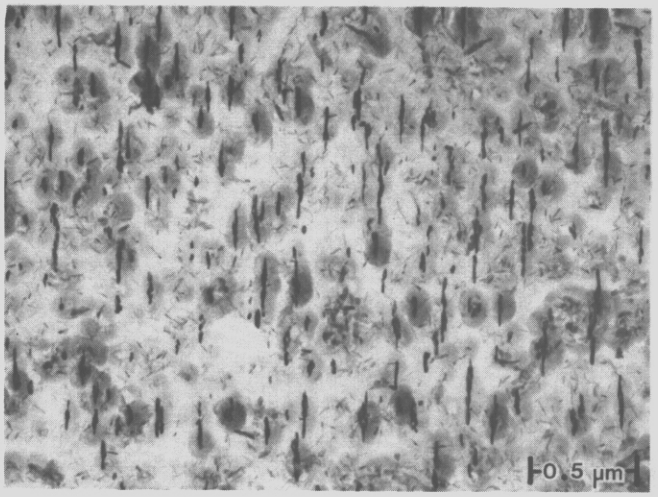

(b)

Fig. 6. Representative TEM micrographs of carbide extraction replicas illustrating a) massive PAG boundary carbides in material austenitized at 950°C and tempered at 650°C for 1h, and b) needlelike matrix carbides in material austenitized at 1200°C and tempered at 650°C for 1h. (Note the alignment of the type 4 carbides versus the random orientation of the type 5 carbides.)

material (again at all T_y's). Qualitatively, the general carbide density appeared to decrease and carbide size to increase slightly as the tempering temperature increased. Again analyses are in progress to quantify this.

Carbide identification efforts have proceeded using both electron diffraction and X-ray energy dispersive analysis. To date results have been largely obtained for the material tempered at 650°C for 1h. Electron diffraction has revealed the presence of carbides with lattice parameters of approximately 1.05 nm and 1.12 nm. The lattice parameter of 1.05 nm corresponds to the lattice parameter expected for $M_{23}C_6$ carbides. The lattice parameter of 1.12 nm is similar to the lattice parameter of M_6C carbides. At this point in the analysis, it is still not certain that M_6C carbides are present. In order to obtain verification of the presence of M_6C carbides, carbides have been extracted from the matrix and the powder collected for examination with an X-ray diffractometer. The large (type 1) carbides as well as the PAG boundary and lath packet boundary carbides (type 2) appear to be $M_{23}C_6$. The intralath carbides (types 3 and 4) have lattice parameters of 1.05 and 1.12 nm. In general the smaller, more elongated carbides (type 4) have a lattice parameter of 1.05 nm and are identified as $M_{23}C_6$. The blockier carbides (type 3) in many cases have a lattice parameter of 1.12 nm. The very small carbides (type 5) have not been analyzed for lattice parameter yet.

A representative sample of carbides from the material austenitized at 950, 1050 and 1200°C and tempered 650°C for lh have been analyzed by X-ray energy dispersive analysis. Tables 2, 3, and 4 summarize results from the three conditions. The large PAG boundary carbides (type 1) present in the material austenitized at 950°C were 64 atom% Cr and 29 atom% Fe. These carbides were of similar composition at several locations in the specimen. The large carbides reported in Table 3 far the material austenitized at 1050°C (type 1) were located within the laths and were found to be of two distinct compositions. In one location the large carbides were 32% Cr, 47% Fe, and 12% Ho; while in another location they were composed of 57% Cr, 36% Fe, and 3% Mo. The small intralath carbides (types 3 and 4) were found to have various compositions. In the T_y = 950°C material, the elongated carbides (type 4) had a composition of 62% Cr, 23% Fe, and 4% Ma, while the blocky (type 3) carbides had a composition of 29% Cr, 41% Fe, and 15% Mo. In the T_y = 1050 and 1200°C conditions, the type 3 and 4 carhide composition varied with location. As can be seen in Tables 3 and 4, the composition varied from 30 to 60% Cr, 20 to 45% Fe, and 2 to 20% Mo. However, in a given location, the compositions were similar. The type 5 carbides have widely different compositions, suggesting there may in fact be two kinds of type 5 carbides. Most of these are probably Mo_2C, but we have yet to confirm this.

Table 2

Average Composition of Carbides in T_y = 950°C Material
(At %)

Type	Cr	Fe	Mo	W	Ni	V	Mn
Large, Type 1 ($M_{23}C_6$)	63.70	29.12	3.61	0.93	0.55	1.81	0.29
Small, Elongated Type 4, ($M_{23}C_6$)	62.17	22.94	4.25	2.41	3.03	4.06	1.08
Small, Blocky, Type 3, (M_6C)	29.08	41.47	14.91	2.15	5.97	0.28	5.54

Table 3

Average Composition of Carbides in Ty = 1050°C Material
(At %)

Type	Cr	Fe	Mo	W	Ni	V	Mn
Large, Type 1	32.52	46.64	12.42	4.30	1.47	0.66	1.98
	51.36	35.61	3.43	1.08	0.36	2.09	0
Small, Type 3	61.25	25.29	5.91	1.44	1.06	1.86	0.68
& 4	40.90	31.68	16.15	4.17	4.11	0.45	2.52
	48.16	30.26	11.80	3.30	2.80	1.17	2.51

Table 4

Average Composition of Carbides in T_Y = 1200°C Material
(At %)

Type	Cr	Fe	Mo	W	Ni	V	Mn
Small Blocky,	33.95	33.66	22.60	3.08	2.92	0.43	3.34
Type 3	69.17	22.31	4.36	0.83	0.68	2.57	0.08
Small Long,	33.74	45.26	13.81	2.72	1.61	0	2.85
Type 4	40.12	32.82	8.54	1.29	5.61	1.61	4.00
	64.44	26.99	2.41	0.75	0.54	4.42	0.46
Very Small,	40.12	9.89	41.80	5.12	0	0.62	1.87
Type 5	78.96	9.39	4.42	0.92	0.29	6.02	0

5.4 Mechanical Property Results

Rockwell C hardness data obtained from specimens at all heat treatments are shown in Fig. 7. As shown in Fig. 7a, the hardness is little changed by austenitizing temperature, although there does appear to be a slight increase in hardness in going from a T of 950°C to 1050°C. The hardness is more strongly affected by tempering condition, and this is better illustrated in Fig. 7b where a typical tempering response is indicated; i.e. the material becomes softer at higher tempering parameters, and the hardness is approximately the same for the same P_T. This may he the result of the loss of the small needlelike carbides as well as a reduction in the matrix dislocation population due to recovery processes and a lass of interstitial carbon from solution as large carbides continue to grow.

The yield strengths of heat treated materials have only been determined to date for a tempering condition of 650°C-1h. Yield strengths were determined from both uniaxial tension and CVN tests at room temperature and 100°C. The uniaxial tensile data are summarized in Fig. 8. Both strength and ductility appear to show slight maxima (note the expanded scale) for a T_Y of 1050°C. It is not clear at this time what microstructural changes are responsible for this, but the ultimate tensile strength (UTS) data are consistent with the hardness data trend. Moreover, the dynamic yield strengths determined from the CVN test show the same trend. As discussed below, the static uniaxial and dynamic yield strengths are consistent with one another when appropriately normalized.

The dynamic fracture toughness values (K_{Id}) determined at low temperatures from PCCV tests are summarized in Figs. 9 and 10. For points plotted here, the load-time traces indicated linear elastic failure and

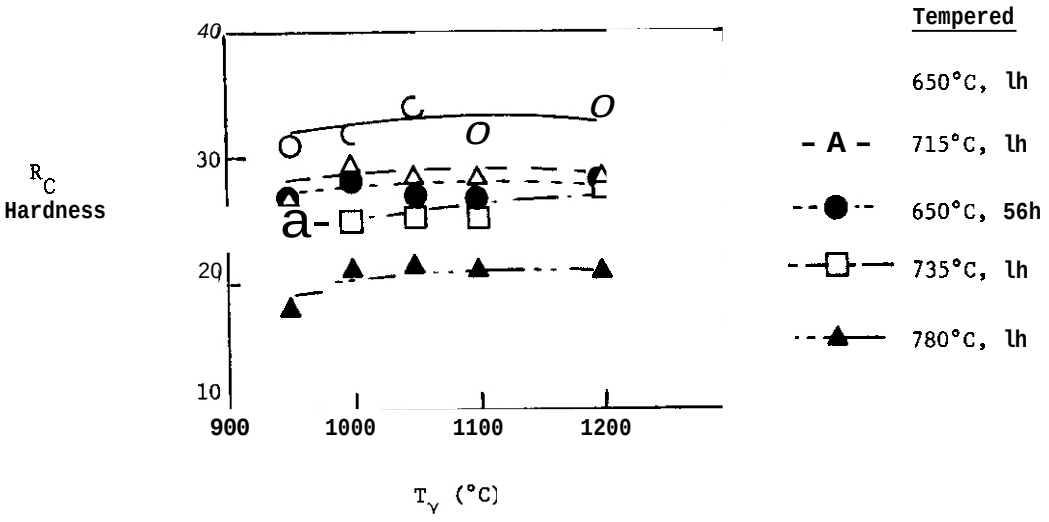

(a)

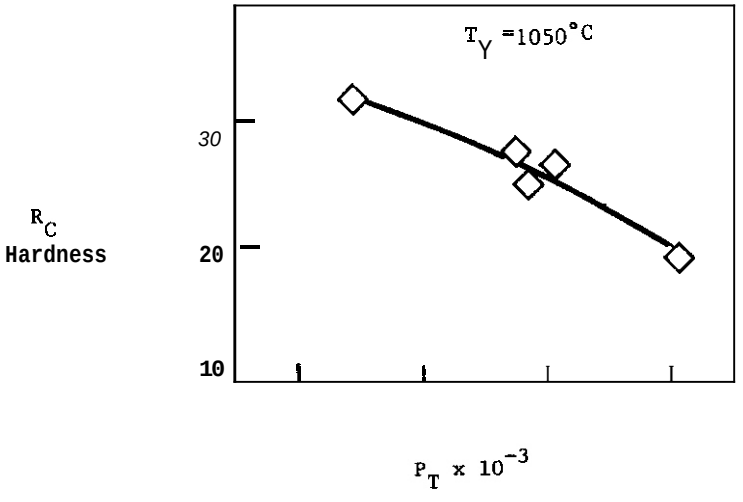

(b)

Fig. 7. Rockwell C hardness as a function of a) austenitizing temperature for 5 tempering conditions, and b) tempering parameter for a γ-T of 1050°C.

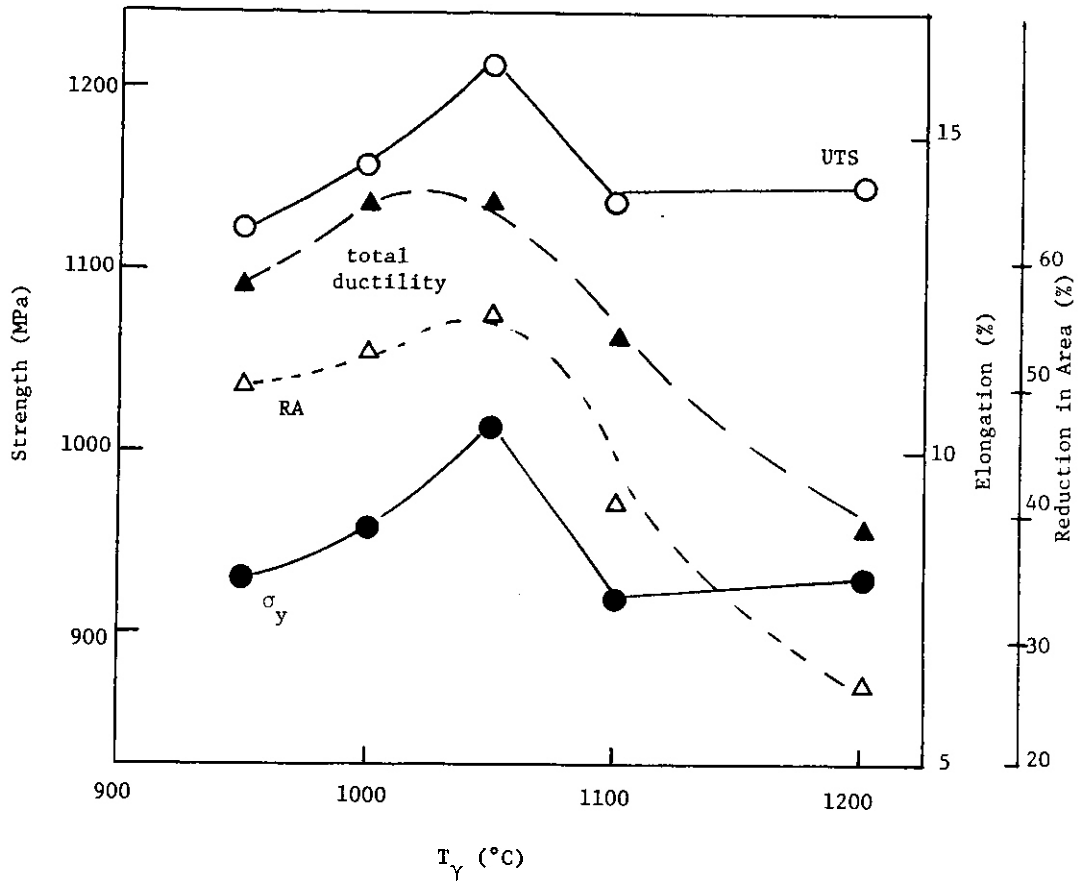

Fig. 8. Uniaxial tensile data **for** HT-9 tempered 650°C **for** lh.

values of K_{Id} were similar **for** the two temperatures, **so** K_{Id} values are probably representative of lower shelf **dynamic** toughness. For each tempering condition, K_{Id} does not appear to vary considerably with T_γ, although in most cases the data suggest a slight minimum at T_γ = 1050°C, (coincident with the strength/hardness peak). There may be competing effects leading to the relative insensitivity of K_{Id} to T_γ. For instance, based on our previous investigation, it might he expected that K_{Id} would decrease markedly with increasing T_γ, since the lath packet size increases by about ten times **from** T_γ = 950° to 1200°C and since previous work suggests K_{Id} a σ_f^* a $1/\sqrt{d}$ or the lower shelf. However, K_{Id} should also be proportional to a critical distance ℓ^* **which** may **scale** with **PAG** size. There may **also be** other microstructural dependencies that have not been accounted for. For instance, it is known that carbide size can scale with ferrite grain and lath packet size in bainitic structures, and hence the $1/\sqrt{d_p}$ dependence of σ_f^* may actually be a correlated dependence on carbide size. Same phenomenological evidence of the carbide size dependence of K_{Id} is shown in Fig. 10, where K_{Id} increases with P_T which alters neither the **PAG** size nor the lath packet **size** but does change the carbide size. Sorting this out will take further analysis.

We attempted to make some estimates of σ_f^* in the following way. Using the K_ρ analysis of Wullaert et al.,[8] σ_f^* can be evaluated from

$$\sigma_f^* = (\ell n\,[1 + \tfrac{1}{2}(K_\rho/2.89\,\sigma_{yd})2| + 1)\sigma_{yd} \qquad (1)$$

where

K_ρ = dynamic fracture toughness measured in a blunt notched CVN test under linear elastic conditions

ρ = notch radius of a CVN specimen (= .25 mm)

a_{yd} = dynamic yield strength at the temperature **and** strain rate of the CVN test.

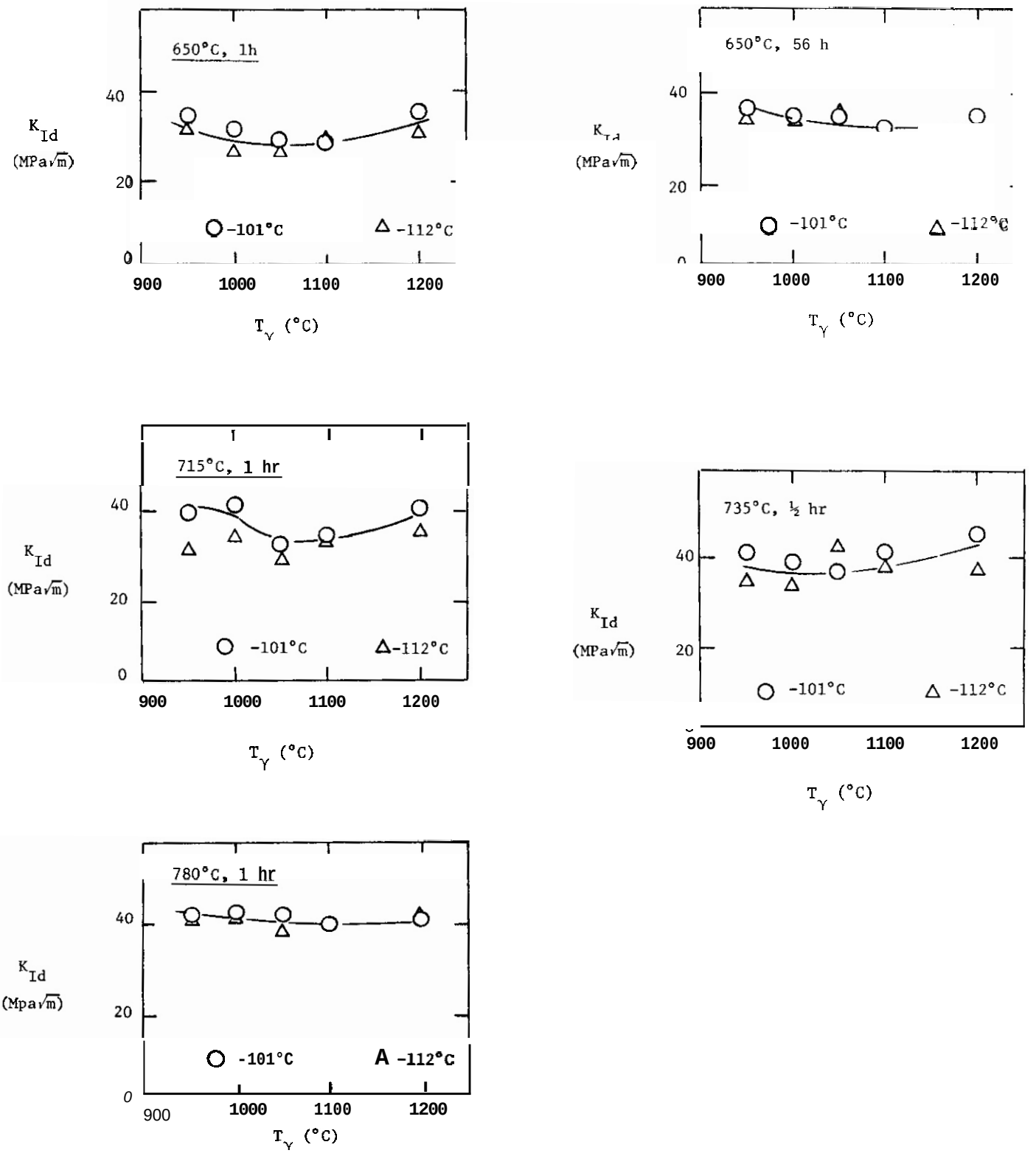

Fig. 9. **Variation of dynamic fracture toughness with TY for different tempering conditions.**

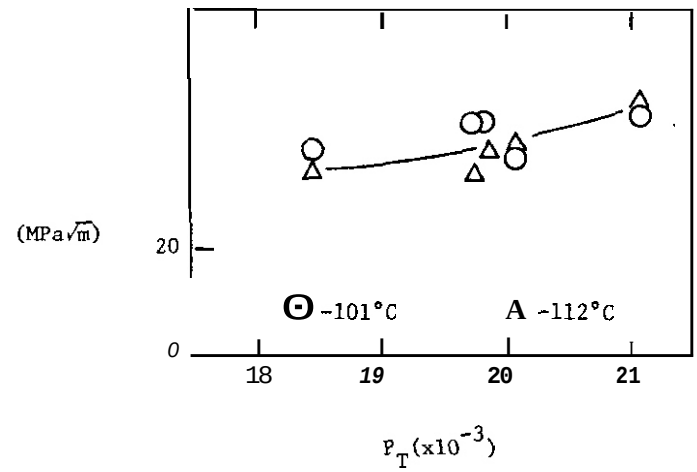

Fig. 10. Variation of dynamic fracture toughness with tempering parameter

Values of K_ρ were determined from the low temperature instrumented CVN tests described earlier. Values of σ_{yd} were obtained in the following way. We fit yield strength data obtained on as-received material tested over a range of strain rates (10^{-3} to $10^{2}s^{-1}$) and temperatures (-100°C to 50°C) to the following simple empirical expression

$$\sigma_Y = 10(3.056 - 9.18x10^{-4}T)\,\dot{\varepsilon}^{.0167} \qquad (2)$$

where σ_Y is in MPa, T in °K, and $\dot{\varepsilon}$ in s^{-1}

This is different than the expression we have provided previously,[3] but it provides a better fit to our data in the strain rate-temperature regime of interest here. It was then assumed that the strain rate/temperature dependence of the yield strength of the heat-treated material was the same as for the as received material; i.e. only the absolute value of σ_{yd} at a particular strain rate and temperature differed. This is based on our observations of similar $\dot{\varepsilon}$-T dependence of σ_y for a range of steels.' Hence, a value of σ_{yd} to be used in eq. (1) was obtained as an average of the static tensile yield and elevated temperature CVN dynamic yield adjusted to the test conditions at which K_ρ was obtained by using

$$\sigma_{yd} = \sigma_{y1} = \sigma_{y2}\,(10^{-9.18x10^{-4}(T_1-T_2)})(\dot{\varepsilon}_1/\dot{\varepsilon}_2)^{.0167} \qquad (3)$$

Values of σ_f^* so obtained are plotted against T_γ in Fig. 11. Like hardness and yield stregath, the calculated values of σ_f^* show a peak at T_γ = 1050°C. Also shown in Fig. 11 is a curve (dashed) depicting the variation of σ_f^* ff it were a function of lath packet size alone; that is previous studies[10,11] including our own' suggest that $\sigma_f^* \sim C/\sqrt{d_\rho}$ where C = 200 MPa$\sqrt{mm}$ and d_ρ is the lath packet size. Clearly there are some uncertainties associated with the methodology by which we have calculated σ_f^* and the differences between the two curves in Fig. 11 may be reduced when we evaluate σ_f^* by more rigorous empirical methods. Moreover, the value of C = 280 MPa$\sqrt{m}$ is derived from data on steels that are more highly tempered than the ones we consider here. However, the shape of the curve indicates that a $1/\sqrt{d_\rho}$ dependence is not followed entirely. Again, the value σ_f^* may be controlled by carbide size rather than lath packet size. Models proposed to describe such a mechanism have been proposed by Smith[12] for mild steels containing lasmellar carbides and by Curry[13] for spheroidized carbide steels. They are generally of the form

$$\sigma_f^* = \sqrt{\frac{CE\,\gamma_\rho}{z}} \qquad (4)$$

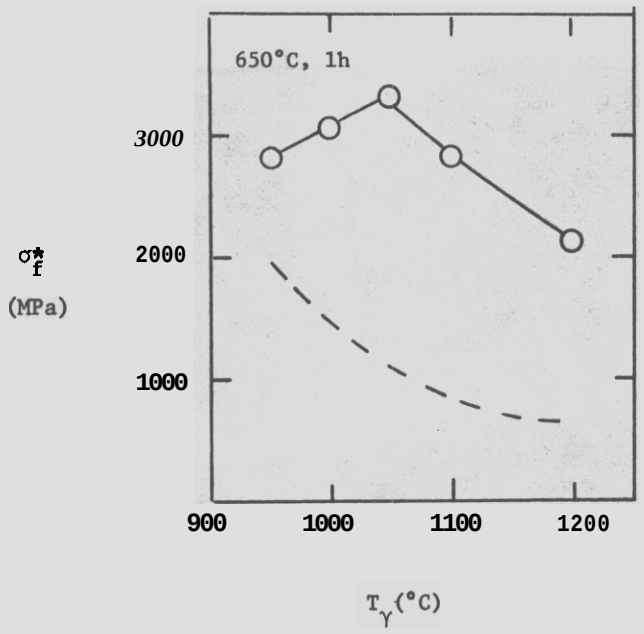

Fig. 11. Variation of calculated values of σ_f^* vs. T_γ.

where C is a constant of the order 1.5, E is the Young's modulus, z is the carbide size, and γ_p the effective surface energy. Knott[21] has discussed a model similar to this for martensitic steels. More recently Bowen and Knott[22] have provided experimental data on lath martensitic A5338 steel heat treated to various grain sizes that suggests the micromechanism of cleavage fracture is the nucleation and propagation of microcracks from autotempered carbides on or within prior austenite grain boundaries. If such is the case for HT-9, the variation in σ_f^* with T_γ in the range 950°C to 1050°C might be explained in the following way. As the HT-9 is austenitized at increasing temperatures, the large blocky carbides at the PAG boundaries decrease in size and density; if these are the primary sites for microcracks, eq. (4) predicts σ_f^* should increase as T_γ increases from 950 to 1050°C, in agreement with data in Fig. 11. However, as discussed previously the changes in carbide size for $T_\gamma \geq 1050$°C are not large, although σ_f^* decreases with increasing T_γ. This may be a result of changes in γ_p, and this is addressed below.

5.5 Fractographic Analysis

Oblique section fractography has permitted us to look at the association between the fracture surface and the subsurface microstructure. We have most frequently observed an association between secondary surface cracks (cracks out of the crack plane) and subsurface microcracks and carbide particles at PAG boundaries. A representative micrograph is given in Fig. 12. Occasional association between microcracks and lath boundary or lath carbides has been observed, but with much less frequency. Such observations support a dependence of σ_f^* on a boundary carbide-micro crack in^ mechanism.

SEM fractography of the fracture surfaces themselves has been conducted for a number of materials. Typical micrographs are shown in Fig. 13. The fracture surface is largely covered with cleavage facets of the order of the lath size. However, thin strips of ductile tearing were also found. Oblique section fractography showed these to he coincident with lath packet boundaries and PAG boundaries. As reported previously,[3] we have also observed microvoids which appear to have propagated through one or more laths and have arrested when they intersect a boundary between regions of high misorientation (e.g. lath packet boundary). Together, this suggests that microcracks are arrested at high angle boundaries and ductile tearing is required for further advancement. The tearing ridges at PAG boundaries were thicker and higher than those at lath packet boundaries. The ridges were nearly continuous along the boundaries, and could also be used to estimate sizes of lath packets and PAG's. Table 5 provides a comparison of size estimates of these two features obtained from tear ridge measurements on fractographs and from TEM of surface replicas. Agreement is quite good.

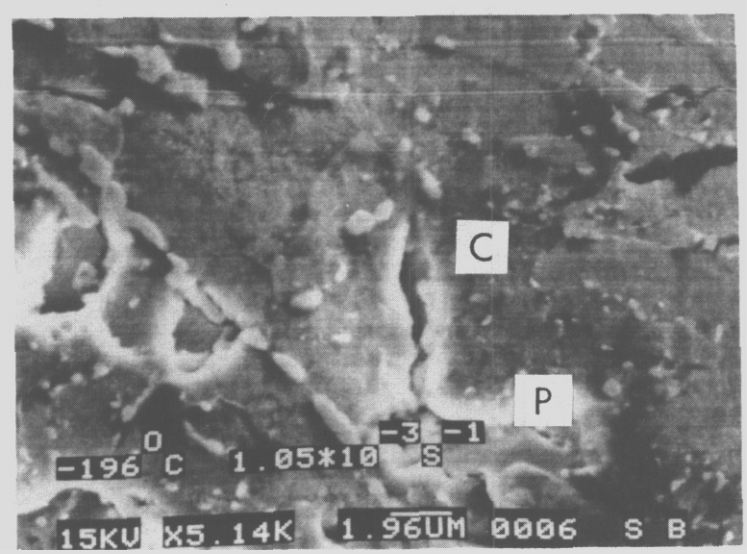

Fig. 12. Representative micrograph showing the association between a microcrack (C) and a PAG carbide (P) observed in oblique section SEM.

Table 5

T_Y (°C)	Feature	Size (μm)* TEM Analysis	Size (μm)* Fractographic Analysis
950	PAG	22±5	29±5
	Lath Packet	8f3	9±1
1000	PAG	30±10	40±10
	Lath Packet	16±3	16±6
1050	PAG	86±7	74±7
	Lath Packet	29±4	28±9
1100	PAG	175±20†	176±39
	Lath Packet	40±15	50±10
1200	PAG	325±40†	294±50
	Lath Packet	95±15	85±15

*Limits indicate range of sizes not standard deviations; numbers are based on approximately 50 measurements.

†Determined from optical micrographs

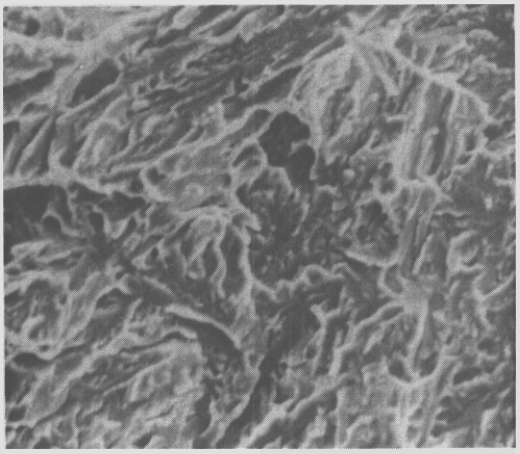

(a)

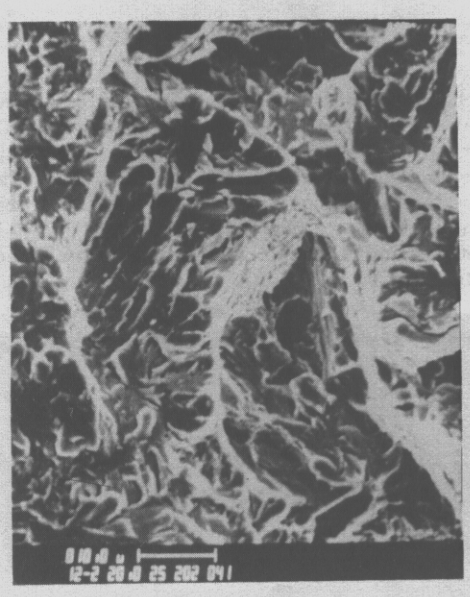

(b)

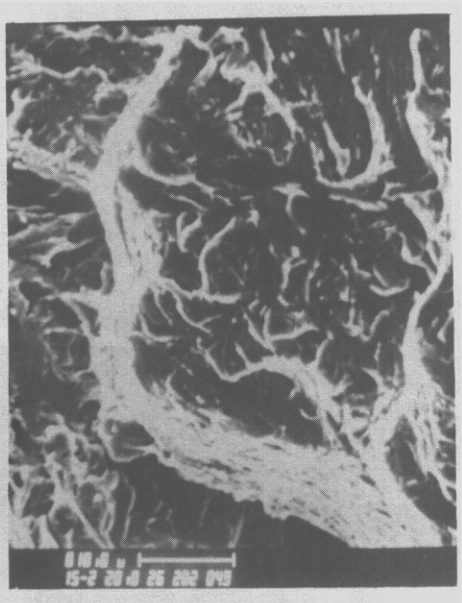

(c)

Fig. 13. Representative fractographs of heat treated HT-9 showing a) cleavage facets within a lath packet, and ductile tear ridges at b) lath packet boundaries, and c) a prior austenite grain boundary.

Material			Tear Ridge Height (μm)		
T_γ (°C)	Tempering Temp (°C)	Tempering Time (h)	PAG Boundary	Lath Packet Boundary	Ratio of PAG/Lath Boundary Ridge Heights
950	650	1	31	10	3.1
1050	650	1	84	15	5.7
1200	650	1	145	18	8.0
1050	650	56	77	12	6.1
1050	715	1	86	12	7.1
1200	715	1	165	18	9.2
1050	735	0.5	93	13	7.2
950	780	1	36	7	5.1
1000	780	1	46	9	5.2
1050	780	1	89	14	6.5
1100	780	1	103	15	6.8
1200	780	1	135	17	7.9

5.6 Conclusion

While we are still in the process of collecting information, the data thus far suggest that both carbide size and tear ridge height play a major role in the micromechanisms of cleavage fracture. As mentioned previously, the increase in σ_f^* from 2800 MPa to 3300 MPa as T_γ increases from 950°C to 1050°C in the material tempered at 650°C for 1h is qualitatively consistent with a decrease in the size and density of large PAG carbides; that is, eq. (4) predicts an inverse dependence of σ_f^* on large carbide size. The decrease in σ_f^* as T_γ increases from 1050 to 1200°C may he due to a decrease in γ_p. If the largest PAG boundary Carbides are critical microcrack nucleation sites in this T_γ regime, $z \sim .8\mu m$ and $\gamma_p \sim 15\ J/m^2$. This is larger than the chemical free surface energy (2-4 J/m^2), and the increase may be related to the ductile tearing that occurs in the formation of tear ridges. If this is the case, γ_p should be proportional to the total boundary length times ridge height per unit area of fracture surface. That is

$$\gamma_p \sim \frac{1}{A}\left[\left(\frac{A}{2d_g^2}\right)\pi d_g h_g + \left(\frac{A}{d^2}\right)\pi d_p h_p\right] \sim \pi\left(\frac{h_g}{d_g} + \frac{h_p}{d_p}\right) \qquad (5)$$

where A = fracture surface area

d_g = PAG size

d_P = lath packet size

h_g = tear ridge height at PAG boundaries

h_P = tear ridge height at lath packet boundaries

Using values of h_g and h_p given in Table 6 and values of d_g and d_p given in Figs. 1 and 3, values of the last term in parenthesis in eq. (5) are 2.6 for T_γ = 950°C, 1.8 for T_γ = 1050°C and 0.64 for T_γ = 1200°C for material tempered at 650°C for lh. This suggests the ratio of $\sqrt{\gamma_\gamma}$ (and thus σ_f^* for constant carbide size) at T_γ = 1200°C vs. 1050°C should he ~ 0.6 which is consistent with σ_f^* values in Fig. 11.

If the RKR model for cleavage fracture were to apply strictly to this system, the lower shelf toughness should vary as $K^{2s} = \sigma^{*1.5} \ell^*$. If ℓ^* were of the order of the PAG size, as has been suggested in previous studies,[1,2,15] then using values of σ_f^* and ℓ^* obtained here for the material tempered at 650°C for 1h, one would expect a continuous 5-fold increase in K_{Id} measured in the lower shelf regime as T_γ increased from 950°C to 1200°C.* As previously shown in Fig. 9, this is clearly not the case. The variation of K_{Id} with T_γ is modest with an approximate minimum at T_γ = 1050°C. Moreover, one might expect, based on arguments above, that for a given T_γ, as the material is tempered to higher P_T's, the value of σ_f^* would decrease, because carbide size increases and tear ridge heights are relatively uninfluenced.[3] Since tempering should not affect ℓ^* if $\ell^* = d_g$, K_{Id} should decrease with increasing P_T. Again, referring to Fig. 10, this is the opposite of what we have observed experimentally. Consequently, it appears that a strict proportionality between ℓ^* and d_g may not hold for the range of microstructures we have investigated. Indeed, ℓ^* may he a parametric convenience which reflects the statistical nature of the cleavage fracture process. That is, assume cleavage fracture occurs when a critical microcrack nucleation/propagation event is triggered ahead of the crack tip. If, for instance, cracked carbides provide the nucleation sites, a whole range of combinations of carbide size and applied tensile stress can trigger the event. For a stress field which varies strongly with position ahead of a sharp crack, cleavage occurs when the first critical combination of stress and carbide size is achieved. This statistical approach has been evaluated by a number of authors.[16-20] Curry[16] demonstrated that the statistical approach was equivalent to the RKR model when the plastic zone ahead of the crack is larger than the critical distance. However, Evans" and Saario et al.[19] have derived expressions for cleavage fracture that *are* not equivalent to the RKR model. At this time we do not have sufficient data to evaluate these alternate models completely, but we will do so in future work.

6.0 References

1. G.R. Odette and G.E. Lucas, J. Nucl. Mat., 117 (1983) 276.
2. G.R. Odette and G.E. Lucas, J. Nucl. Mat., 117 (1983) 264.
3. G.R. Odette, G.E. Lucas, K. Naiti, and J.W. Sheckherd, J. Nucl. Mat., 122/123 (1984) 442.
4. G.R. Odette, G.E. Lucas, R. Haiti, and J.W. Sheckherd, J. Nucl. Mat., 133/134 (1985).
5. R.O. Ritchie, J. Knott, J. Rice, J. Mech. Phys. Solids, 21 (1973) 395.
6. T.A. Lechtenberg and S. Heifrich, DOE/ER-0045/3, June 1980, 201.
7. O.R. Dobbs, Met. Prog., Dec. (1984) 33.
8. R.A. Wullaert, D.R. Ireland, A.S. Tetelman, ASTM STP 484 (1970) 20.
9. G.R. Odette, P.M. Lombrozo, R.A. Wullaert, ASTM-STP-870 (1985).
10. P. Brozzo, G. Buzzichelli, A. Mascanzoni, M. Mirabile, Met. Sci., 11 (1977) 123.
11. G. Green, Ph.D. Thesis, Cambridge University (1975).
12. E. Smith, Proc. Conf. Phys. Basis Yield and Fracture, 36 (Inst. Phys. and Phys. Soc., 1966. Oxford).
13. D. Curry (unpublished work).
14. P. Brown and J. Knott, Met. Trans., 17A (1986) 231.
15. R.O. Ritchie, W.L. Server, R.A. Wullaert, Met. Trans., 10A (1979) 1557.
16. D.A. Curry, Met. Sci., 14 (1980) 78.
17. A.G. Evans, Met. Trans., 14a (1983) 1349.
18. T.M. Beremin, Met. Trans., 14A (1983) 2271.
19. T. Saario, K. Wallin, K. Torronnen, J. Eng. Mat. Tech., 106 (1984) 173.

---

* This assumes that $K_{Id} = K_{IC}^{\ell s}$; however, if the strain rate is high enough, a different cleavage initiation mechanism may dictate K_{Id} vs. $K_{IC}^{\ell s}$.

20. D.A. Curry and J.F. Knott, Met. Sci., 13 (1979) 341.

21. J. Knott, Conf. on Living With Defects, Roy. Soc. London (1979).

7.0 Future Work

We will continue to obtain microstructural and mechanical property data on heat treated materials. and we will use the data to more fully evaluate micromechanistic models for cleavage fracture.

8.0 Publications

1. G.R. Odette, G.E. Lucas, R. Maiti, J.W. Sheckherd, "The Effects of Strength and Geometry on Cleavage Fracture and Strain Limits of Uartensitic Stainliness Steels," J. Nucl. Mater., 133/134 (1985).

APPLICATION OF HYUKOGEN EMBRITTLEMENT MODELS TU THE CRACK GROWTH BEHAVIOR OF FUSION REACTOR MATERIALS

Russel1 **H.** Jones (Pacific Northwest Laboratory)

1.0 Objective

The purpose of this evaluation was to apply existing models of hydroyen induced crack growth to examine the potential effect of hydrogen on fusion reactor. materials. Hydrogen from the plasma, cathodic corrosion and nuclear reactions within a material was examined. The initial analysis was limited to HT-9 but other fusion reactor materials such as vanadium alloys will be the subject of future evaluations.

2u Summary

Hydrogen induced crack growth rates of HT-Y have been estimated for three sources of hydrogen: the plasma, nuclear reaction and aqueous corrosion. Estimdtes of crack growth rates were derived using hydrogen embrittlement models which describe the temperature and hydrogen activity dependence of .cracking. A crack growth rate of 10^{-3} cm/s at a reactor operdting temperature of 400°C was ohtained for a steady-state hydrogen concentration of **U5** appm resulting from (n,p) reactions. while a much slower Crack growth rate was predicted for the same steady-state hydrogen concentration with an alternate model. These calculations have shown the need for further research to assess the effect of temperature on crack growth. Other sources of hydrogen give very slow hydrogen induced crack growth rates at reactor operating temperatures while significant hydroyen induced crack growth rates are possible at lower temperatures. For instance, hydroyen from *an* aqueous corrosion reaction could produce a crack growth rate of 10^{-7} cm/s at 25°C which could he significant duriny extended downtime. Also, a non-equilibrium hydrogen uptake from the plasma could occur from surfdce reaction controlled effects, and a crack growth rate of 10^{-1} cm/s was estimated for this condition at a temperature of 75°C. Rased on this analysis, hydrogen induced crack growth is not considered significant for *HT-9* during reactor *operation* but may he a problem duriny extended downtime if the temperature decreases to a value less than 100°C.

3.0 Program

Title: Mechanical Properties
Principal Investigator: R. H. Jones
Affiliation: Pacific Northwest Laboratory

4.0 Relevant DAFS Program Plan Task/Subtask

Subtask II.C.9 Effects of Hydrogen on Fracture

5.0 Accomplishments and Status

5.1 Background

Hydrogen induced crack growth of materials can result from both external gaseous or cathodic hydrogen and from internal dissolved hydrogen. In a fusion reactor there are several potential sources of hydrogen or hydrogen isotopes including direct injection *from* the plasma, tritium gas in the breeding blanket, nuclear (n,p) reactions within the material or, for water-cooled systems, cathodic reduction from an aqueous corrosion reaction.

Hydrogen has been shown to induce cracking in a wide variety of materials, including ferritic steels, austenitic stainless steels, nickel-based alloys and aluminum alloys. The mechanism by which hydrogen causes crdckiny is generally thought to be the collection of hydrogen at particle-matrix interfaces, grain boundaries ahead of the crack tip or other defects. The distance that the hydrogen concentrates ahead of the crack tip is not well established, but for external hydrogen it may be anywhere from a few hundred angstroms to a few micometers [1]. Earlier work by Williams and Nelson [2] and recent analysis by Pasco, Sieradzki and Ficalora [3] considered the hydroyen effect to be primarily a surface chemistry controlled process.

Temperature and hydrogen activity are two parameters on which the crack growth rate is strongly dependent. Material parameters such as yield strength, hydrogen diffusivity, hydrogen trap densities and strength, and grain boundary chemistry are also important. The purpose of this paper is to use existing models of hydrogen induced crack growth to estimate the temperature and hydrogen activity dependence of the crack growth rate for hydrogen from the plasma, nuclear reactions and aqueous corrosion reactions. HT-9 is used as the base material, and the material parameters are not varied except that the yield strength is assumed to be that following radiation hardening.

5.2 Hydrogen induced crack growth rates

5.2.1 External gaseous hydrogen

Hydrogen uptake is generally recognized as a surface controlled process which may involve several surface reaction steps. Most hydrogen adsorption studies suggest the existence of a molecular precursor state [4-6] which is intermediate between gaseous hydrogen and the chemisorbed state. This precursor dissociates into atomic hydrogen, which is then absorbed into the material. Several observations of crack growth of high-strength steel in gaseous hydrogen have been interpreted as being controlled by the adsorption rate of hydrogen [1-3,7,8]. Williams and Nelson [2] modeled the crack growth rate-temperature dependence of 413U steel in gaseous hydrogen with a gas phase adsorption isotherm for hydrogen adsorption on iron. Simons, Pao and Wei [7] found a similar temperature dependence and low-temperature activation energy for a 4340 steel in gaseous hydrogen and concluded that the rate-limiting step was surface reaction controlled. Gangloff and Wei [8] found that the temperature dependence of the low-temperature crack growth rate of a maraging steel was similar to that observed by others [2,7]; however, they concluded that the crack growth rate was controlled by short-range diffusion of hydrogen or the kinetics of a hydrogen-iron embrittlement reaction associated with either near-surface or sub-surface hydrogen. Pasco, Sieradzki and Ficalora [3] were ahle to model the low-temperature regime observed by Gangloff and Wei using a surface adsorption-desorption kinetic model. Examples of the two types of crack growth rate versus temperature relationships found for steels are given in Figure 1.

Williams and Nelson [2] found that the temperature and pressure dependence of the crack growth rate of 4340 steel could be accurately described by the following hydrogen adsorption isotherm:

$$\frac{d\theta}{dt} = \alpha P^{1/2} (1-\theta) \exp(-E_m(\theta)/RT) \qquad (1)$$

where α is related to the condensation coefficient, P is the pressure. θ the fraction of final adsorption sites, E_m the energy of migration of an adatom from an initial physisorption site to a final chemisorption site, R is the gas constant and T is the temperature. Inserting the appropriate relationship for α and the assumption that the crack growth rate is equal to the adsorption rate at a given coverage, equation 1 can be simplified to the following two expressions for the low-temperature regime (curve 1), equation 2, and the high-temperature regime (curve 1), equation 3, in Figure 1:

$$\frac{da}{dt} = C_3 P^{1/2} \exp(-E_m/RT)$$

$$\frac{da}{dt} = C_4 P^{3/2} T^{-1/2} \exp(-\Delta H - E_m/RT) \qquad (3)$$

where C_3 and C_4 are constants, and ΔH is the heat of adsorption of hydrogen. Williams and Nelson also found that the measured pressure dependence was consistent with those expressed by equations 2 and 3. An increase in the hydrogen pressure increased the crack growth rate and shifted the peak in the crack growth rate curves to higher temperatures.

Equations 2 and 3 are therefore appropriate for assessing the crack growth rates of a fusion reactor first wall exposed to a hydrogen gas. To adopt its use for evaluating the effect of a hydrogen plasma on the crack growth rate it is iiecessary to relate the hydrogen flux impinging on a first wall to an equivalent hydrogen gas pressure which would give the same colljsion rate with the surface. Such a comparison has been made by Ashby [9] where a hydrogen flux of 10^{17} H/cm -s was equal to a pressure of 10^{-2} Pa. Therefore, as a first estimate this pressure was used to represent the effect of a hydrogen plasma on the crack growth rate of HJ-9, and using the parameters listed in Table 1 the crack growth rate versus temperature relationship given in Figure 2 resulted. It is clear from this calculation that the hydrogen activity of the plasma is sufficiently low so as to have no effect on the crack growth rate of HT-9 based on this agalysis. The maximum crack growth calculated with equations 2 and 3 for a pressure of 10^{-2} Pa is 1.6 x 10^{-} cm/s, and it occurs at a temperature of -125°C. At 25°C the crack growth rate is 10^{-13}, and at 200°C it is 10^{-15} cm/s.

The excellent fit between the crdck growth rate of 4340 steel and the adsorption isotherm relationship used hy Williams and Nelson [2] only demonstrates that adsorption is the rate-limiting step hut does not prove that surface hydrogen causes cracking. Hydrogen-induced crack growth is thought to result from hydrogen, which diffuses to some point ahead of the crack tip. Nelson. Williams and Tetelman [10] illustrated this hy measuring the crack growth rate of 4340 steel in atomic hydrogen produced with a hot filament in hydrogen gas. The crack growth rates increased by several orders of magnitude, and the activation energy of the low-temperature regime increased to a value equal to the heat of solution of hydrogen in iron. Nelson et al. concluded that the slow step in crack growth in molecular hydrogen is the migration of adsorbed molecular hydrogen to a dissociation site on the steel surface. If atomic hydrogen is the adsorbing species, then the rate-limiting step is controlled by the heat of solution of hydrogen in steel. This result indicates that the surface hydrogen concentration was not the cause of cracking but merely the supply of hydrogen to defects within the material.

Since hydrogen from the plasma is either neutral or ionic atomic hydrogen, it is possible that its effect on cracking will be greater than that of molecular hydrogen at an equivalent pressure. Using the results of Nelson et al. [10], the pressure used in their ionized hydrogen test, 10^{-2} Pa, results in the crack growth rate versus temperdture relationship given in Figure 3. The data of Nelson et al. was insufficient to describe the hiyh-temperature regiine in atomic hydrogen; therefore, it is not possible to determine the temperature of the maximum crack growth rdte and the crack growth rates at high temperatures. Although significant crack growth rates are feasible in atomic hydrogen at temperatures below 100°C, atomic hydrogen would not be present at low temperatures when the reactor is shut off. It is important to note that hydrogen from the plasma has sufficient energy to he injected into the first wall. Injection of hydrogen would eliininate the rate limiting hydrogen dissolution step observed by Nelson et al. in their ionized hydrogen experiment. Therefore, the results given in Figure 3 may under-predict the crack yrowth rate resulting from injected hydrogen.

The adsorption rate relationship for crack growth proposed by Williams and Nelson considers the crack moving forward in a continuous process governed by the adsorption rate. Gerherich, Livne and Chen [1] have presented a model that hlends the adsorption rate concept with the transport of hydrogen to a location ahead of the crack tip. Gerherich et al. modeled the hydrogen effect assuming a temperature dependence as given by curve #2 in Figure 1 where T_o is a function of the hydrogen pressure and coverage on the surface. They also assumed that cracking was controlled by sub-siirface hydrogen which was supplied by surface adsorbed hydrogen and was controlled by the trapping of hydrogen at defects. Each incremental crack advance occurred when a critical coverage resulted at the emhrittlement site which was 500°A beneath the surface. The crack growth rate was described hy Gerberich et al. as follows:

$$\frac{da}{dt} = \frac{4D_o \exp(-Q^{eff}/RT)}{\chi^{CR}} \left[1-\exp\frac{(\frac{1+\pi}{2})\sigma_y \bar{V}_H (T-T_o)}{RTT_o}\right]^2 \qquad (4)$$

with the definitions and values for the parameters given in Table 1. The critical parameter in equation 4 is T_o because as T approaches T_o the crack growth rate decreases rapidly towards zero. Gerberich et al. estimated the value of T_o as a function of hydrogen surface coverage as given by the curves in Figure 4. It is apparent from this data that for the two critical surface coverages in Figure 4 the value of T_o is well below room temperature for a pressure of 10^{-2} Pa, which is consistent with the conclusion reached using equations 2 and 3 as given by the results in Figure 2.

The analysis by Gerberich et al. assumes an equilibrium adsorption process between molecular hydrogen gas and a surface. This equilibrium between the surface coverage of hydrogen and the hydrogen pressure can he altered and a quasiequilibrium estahlished hy alterations in the surface chemistry or structure. An example is given in Figure 5 where the surface hydrogen coverage was found by Baer and Jones [11] to he a function of the surface sulfur coverage. Also, the coverage of hydrogen obtained with a very clean surface obtained hy sputter cleaning the surface in a vacuum of 10^{-8} Pa was suhstantially greater than expected for the

hydrogen pressure of 10^{-3} Pa used in this experiment. Therefore, it is possible that a quasiequilibrium surface coverage of hydrogen could occur on a fusion first wall because of it's surface chemistry. Assuminy a quasiequilibrium coveraye of hydrogen which results in a hydrogen coverage of 0.15 and a T_o of 400°K, equation 4 resulted in the crack growth rate versus temperature relationship given in Figure 6. This condition represents the worst possible case where the quasiequilibrium surface coverage results in a T_o of 400°K and a maximum crack growth rate of 10^{-1} cm/s at about 50°C. Even with these extreme conditions it is not likely that hydrogen from the plasma will cause crack growth of HT-9 because the crack growth rate at reactor operating conditions when plasma hydrogen is present is extremely slow.

5.2.2 External cathodic hydrogen

Structural materials in a water cooled fusion reactor will undoubtedly be chosen because of their slow corrosion rates in reactor coolants; however, even at very low corrosion rates there are finite anodic and cathodic current densities. The reduction of hydrogen at a cathode can be described by the following equations:

$$H^+ + e^- \rightarrow H_{ads} \tag{5}$$

$$2H_{ads} \rightarrow H_2 \tag{6}$$

Hydrogen adsorbs as atomic hydrogen in a cathodic reaction whereas yaseous hydrogen adsorbs as molecular hydrogen and dissociates on the material surface. Therefore, the activation energy for crack growth would he expected to differ from that observed with gaseous hydrogen where the activation eneryy in the low-temperdture regime is related to the migration of molecular hydrogen on the surface to a dissociation site.

The rate of hydroyen reduction can he described hy the Tafel equation:

$$\phi_H = \beta \log \frac{i}{i_o} \tag{7}$$

where ϕ_H is the hydrogen overpotential, β is the Tafel slope, i_o is the exchange current density for hydrogen on the material of interest and i is the corrosion current density. Values of 0.1, 5×10^{-7} A/cm^2 and 10^{-6} A/cm^2 were assumed for β, i_o and i, respectively, which results in a hydrogen overpotential of 0.03 mV for HT-9 in high temperature water. The relationship between an electrode potential and the activity of hydrogen is given by the Nernst equation under equilibrium conditions; however, McCright [12] has shown that the Nernst equation does not accurately describe the relationship between electrode potential and hydrogen pressure. Therefore, the experimental relationship between hydrogen overpotential and hydrogen pressure given by McCright was used to estimate the hydrogen pressure as given by the following relationship:

$$P_{H_2} = 0.15\ \phi_H \qquad \text{Pa/mV} \tag{8}$$

For the conditions given above, a hydrogen pressure of 4.5×10^{-3} Pa was estimated. The cathodic hydrogen induced crack growth rate was then estimated using equations 2 and 3 and the calculated hydrogen pressure.

It was assumed that the desorption process of hydrogen from an electrode in equilibrium with an aqueous environment is the same as a surface in equilibrium with a gas. This is a reasonable assumption because the desorption process on both surfaces involves the recombination of atomic hydrogen on the surface to form molecular hydrogen. In gas phase equilibrium, the molecular hydrogen on the surface is in equilibrium with molecular hydrogen in the yas phase while in the aqueous hydrogen case, the molecular hydroyen on the surface is in equilibrium with molecular hydrogen in the gas phase contained in bubbles on the surface. There may be a small difference between these two equilibrium states, but for the purpose of this calculation it is assumed that they are the same.

Hydrogen adsorption in the aqueous case was assumed to differ from that in gaseous hydrogen because it adsorbs in the atomic state in the aqueous case and molecular state in the gas phase case. Therefore, the activation energy for crack growth in the low-temperature regime was taken as that of 29 kJ/mol found by Nelson, Williams and Tetelman [10] for crack growth in atomic hydrogen. With these assumptions, the calculated crack growth rate versus temperature relationship given in Figure 7 resulted. Also shown in Figure 7 is experimental crack growth rate data for HT-9 tested in 1N H_2SO_4 at the corrosion potential and a

temqerature of 25°C. The calculated and experimental datd are in close agreement with the loner pH in the 1N H_2SO_4 accounting for the faster crack growth rates in the experimental test. Acidification of the crack chemistry can occur because of hydration of metal ions vrithin the crack solution and crack transport processes as reported by Turnbull [13]. Therefore, it is possible that the crack growth rate in water with a pH of 7 could shift towards the experimental datd because of crack tip acidification.

The calculated crack yrowth rate results for HT-9 in a water coolant are sinilar to those obtained for gaseous hydrogen from the plasmd. Significant crack growth rates occur only around room temperature, where crack growth rates of about 6 x 10^{-8} cm/s (1.8 cm/yr) could result while a crack growth rate of 2 x 10^{-10} cm/s (6 x 10^{-3} cm/yr) results at reactor operating temperatures. Therefore. the crack growth rate of HT-9 induced hy corrosion in an aqueous coolant is not expected to he a problem except for reactor shutdown periods where the temperature decreases below 100°C.

5.2.3 Internal hydrogen

Hydrogen yenerated by nuclear reactions is formed as internal hydrogen which can diffuse to trap Sites such as grain boundaries and particle-matrix interfaces and cause hydrogen induced cracking. Testing for the effect of internal hydroyen on the fracture of materials can done with a constant load test where the time to failure relates to the time for hydrogen to diffuse to internal defects or interfacer. When a crack exists in the material, internal hydrogen will concentrate ahead of the crack tip because of the hydrostatic stress state. Hydrogen will diffuse to grain boundaries and particle-matrix interfaces by an equilibrium segregation process similar to elements *such* as S, P, etc. *Shin* and Meshii *[14]* hdve estimated the effect of hydrogen segregation to the grain boundaries of iron and concluded that a monolayer of hydrogen could segregate to the grain boundaries and that this quantity reduced the fracture stress of iron hy a factor of 2 relative to the fracture stress resulting from the presence of only S at the grain boundaries.

Gerberich, Chen and St. John [15] have modeled the hydroyen-stress field interactions to develop a kinetic model *of* Crack growth for internal hydrogen. They assumed that the stage *II* crack yrowth kinetics which *are* nearly stress-intensity independent are controlled primarily by the plastic stress field. The crdck growtli rate relationship proposed by Gerberich et al. is given by equation 9 below:

$$\frac{da}{dt} = \frac{9\, C_o D_A \bar{V}_H \sigma_y}{2\, d\, RT (C_{CR} - C_o)} \tag{9}$$

where the definition and numerical values given in Tahle 1. To account for strong hydrogen trapping, which is expected in HT-Y, the expression given by Ellerbrock [16] for D_A was substituted for D_A in equation 9 to give the following expression:

$$\frac{da}{dt} = 4\, D_o \exp\left(\frac{-Q^{lattice}}{RT}\right) \left\{1 + \frac{\alpha_4}{T} \exp\left(\frac{2Hs}{RT}\right)\right\}^{-1} \left[\frac{9\, C_o \bar{V}_H \sigma_y}{2dRT(C_{CR} - C_o)}\right]. \tag{10}$$

The crack yrowth rate versus temperature relationship given in Figure 8 was determined using equation 10 for various values of C_o ranging from 0.0005 to 5 appm with *a* single value of C_{CR} of **10** appm.

The variable C_o in equation 10 is the initial hydrogen concentration existing in the material which is in equilibrium with external hydrogen. However, in a fusion reactor first wall, the hydrogen concentration will reach a steady state which is a function of its generation rate, transport rate and external pressure. Stoltz, Baskes and Look [17] have evaluated the steady-state hydrogen concentration in a fusion first wall structure made *of* HT-Y for various surface reactions and for conditions of hydrogen generation by (n,p) reaction and direct injection from the plasma. They found a very small temperature dependence between 473 and 673°K for steady-state hydrogen concentrations ranging from 0.0005 appm to 0.5 appm; therefore, it was assumed as d first approximation that C_o is temperature independent. The highest Steady-state hydruyen concentration of 0.5 appm resulted when they assumed that surface recombination of hydrogen was the rate-limiting step in the desorption of hydrogen. For injected hydrogen the steady-state concentration was 0.5 appm hydrogen and for (n,p) hydrogen it was 0.01 appm hydrogen. Crack growth rates for these steady-state hydroyen concentrations are given in Figure 8 based on equation 10, and it can be seen that the crack yrowth rates increase with increasing temperature and reach a plateau at about 200°C. This relationship predicts a crack growth rate of 2 x 10^{-3} cm/s for a hydrogen concentration of 0.5 appm and 2 x 10^{-4} cm/s for a hydrogen concentration of 0.05 appm. Even the lowest hydrogen concentration calculated by Stoltz et al. could result in a crack growth rate of 2 x 10^{-6} cm/s, which corresponds to 60 cm/yr. As this rate would be intolerable in a fusion reactor design, experimental verification of this result is important.

In a recent analysis, Gerberich, Livne and Chen [1] evaluated the temperature dependence of hydrogen induced crack growth for internal hydrogen in a manner similar to that for external gaseous hydrogen. This later analysis gives a maximum crack growth rate at around room temperature with a rapidly decreasing crack growth rate with increasing temperature. The effect of a steady-state hydrogen concentration could not be readily assessed with this relationship; however, the parameters used by tierberich et al. in his analysis were similar to those used to derive the curves in Figure 8 so that the HT-9 should have comparable behavior. If Gerherich et al.'s analysis is correct, the effect of (n,p) generated hydrogen would be similar to that for external gaseous and cathodic hydrogen where there is a temperature limit above which the crack growth rate decreases very rapidly. For an internal hydrogen concentration of 200 appm as evaluated by tierberich et al., this upper temperature limit is equal to about 50°C. Limited experimental data for 4340 steel was consistent with the theoretical analysis.

While Gerberich et al. took precautions to prevent hydrogen loss during crack growth testing, there is a possibility that hydrogen loss did occur along the crack walls which were uncoated. Also, in a fusion reactor, hydrogen will he continuously generated so that a steady-state concentration develops while C_0 would decrease in the tests by Gerberich et al. if hydrogen loss occurred. Clearly, clarification of the temperature dependence of the crack growth rate induced by internal hydrogen is needed for candidate fusion reactor materials.

6.U Keferences

[1] W.W. Gerberich, T. Livne and X. Chen, in: Proceedings of a Symposium on Modeling Environmentdl Effects on Crack Initiation and Propagation, Toronto, Canada, 1985, Eds. R.H. Jones and W.W. Gerherich (TMS-AIME, Warrendale, PA).
[2] D.P. Williams and H.G. Nelson, Metall. Trans. 1 (1970) 63.
[3] R.W. Pasco, K. Sieradzki and P.J. Ficalora, Scripta Met. 16 (1982) 881.
C41 M.R. Shanabarger, in: Advanced Techniques for the Characterization of Hydrogen in Metals, Eds. N. Fiore and B. Berkowitz (The Metallurgical Society of AIME, Warrendale, PA, 1982) p. 155.
[5] E. Nowicka, Z. Wolfram, W. Lisowski and R. Dus, Surface Science 151 (1985) L116.
[6] N.V. Hieu and J.H. Craig, Surface Science 150 (1985) L93.
[7] G.W. Simmons, P.S. Pao and R.P. Wei, Metall. Trans. A 9A (1978) 1147.
[8] R.P. Gangloff and K.P. Wei, Metall. Trans. A 8A (1977) 265.
[9] C. Ashby, Proceedings of the Third Topical Meeting on Fusion Reactor Materials, Albuquerque, NM, *1983,* Eds. J.R. Whitley, K.L. Wilson and F.W. Clinard, Jr., (North-Holland, Amsterdam, 1984), p. 1406.
[10] H.G. Nelson, D.P. Williams and A.S. Tetelman, Metall. Trans. 2 (1971) 953.
[11] R.H. Jones and D.R. Raer, Scripta Met., in press.
[12] R.D. McCright, in: Stress Corrosion Cracking and Hydrogen Embrittlement, Eds. R.W. Staehle, J. Hockmann, R.D. McCright and J.E. Slater (National Association of Corrosion Engineers, Houston, 1973) p. 306.
[13] A. Turnbull, in: Proceedings of a Symposium on Embrittlement by the Localized Crack Environment. Philadelphia, PA, 1983, Ed. R.P. Gangloff (TMS-AIME, Warrendale, PA, 1984) p. 3.
[14] K.S. Shin and M. Meshii, Scripta Met. 17 (1983) 1121.
[15] W.W. Gerberich, Y.T. Chen and C. St. John, Metall. Trans. A 6A (1975) 1485.
[16] H.G. Ellerbrock, G. Vibrans and H.P. Stuve, Acta Met. 20 (1972) 53.
[17] R.E. Stoltz, M.I. Raskes and G.W. Look, Alloy Development *for* Irradiation Performance Quarterly Report for Period Ending Sept. 30, 1980 (DOE/ER-0045/4) p. 151.

7.0 Future Work

The temperature dependence of hydrogen induced crack growth of HT-9 at temperatures above 25°C will be examined experimentally. Also, the effect of hydrogen on the fatigue crack growth *of* HT-9 will be examined experimentally and theoretically. Application *of* hydroyen embrittlement models to vanadium alloys will be evaluated.

8.0 Publications

None.

TABLE 1

Parameter	Definition	Value
C_3	Constant	1.05 $cm^2/s\text{-}N^{1/2}$
C_4	Constant	2.1 x 10^{-7} $cm^4\text{-}K^{1/2}/N^{3/2}\text{-}s$
E_m	Surface migration energy	16.6 kJ/mol
$-\Delta H$	Heat of adsorption of hydrogen	-40.6 kJ/mol
σ_y	Yield strength	1660 MPa
D_o	Hydrogen diffusivity (Eq. 4)	3 x 10^{-5} m^2/s
D_o	Hydrogen diffusivity (Eq. 10)	1.2 x 10^{-7} m^2/s
Q^{eff}	Activation energy for hydrogen diffusivity	35.4 kJ/mol
$\tilde{V}_H$	Partia1 molar volume of hydrogen in metal	2 x 10^{-6} m^3/mol
X^{CR}	Distance of hydroyen embrittlement site from crack surface	5 x 10^{-8} m (external)
X^{CR}	Distance of hydrogen embrittlement site from crack surface	1.38 x 10^{-4} m (internal)
$Q^{lattice}$	Activation energy for diffusion of untrapped hydrogen	7 kJ/mol
α_4	Constant	5 x 10^{-5} K
H_b	Binding eneryy between hydrogen and a trap	96 kJ/mol
H_s	Heat of solution of hydrogen	27 kJ/mol
β	Constant	5.6 kJ/mol
θ_o	Hydrogen surface coverage at T_o	0.15
d	Grain size	10^{-4} m
C_o	Initial hydroyen concentration	5 x 10^{-4} to 5 appm
C_{CR}	Critical hydrogen concentration for crack advance	10 appm

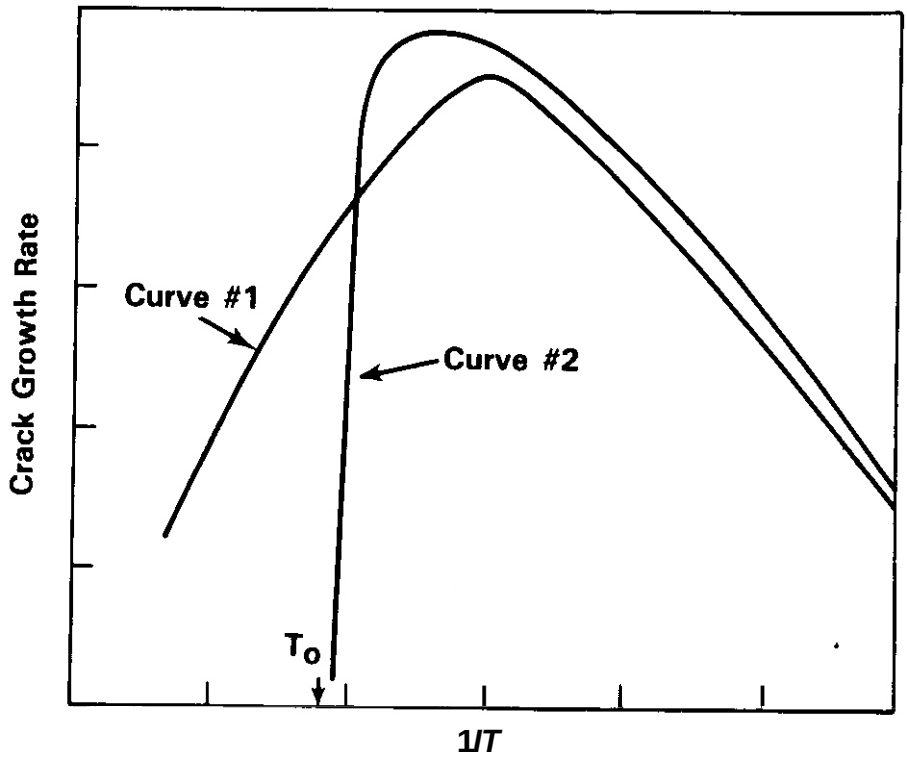

FIGURE 1. Schematic of crack growth rate - 1/T relationships for steels in gaseous hydrogen.

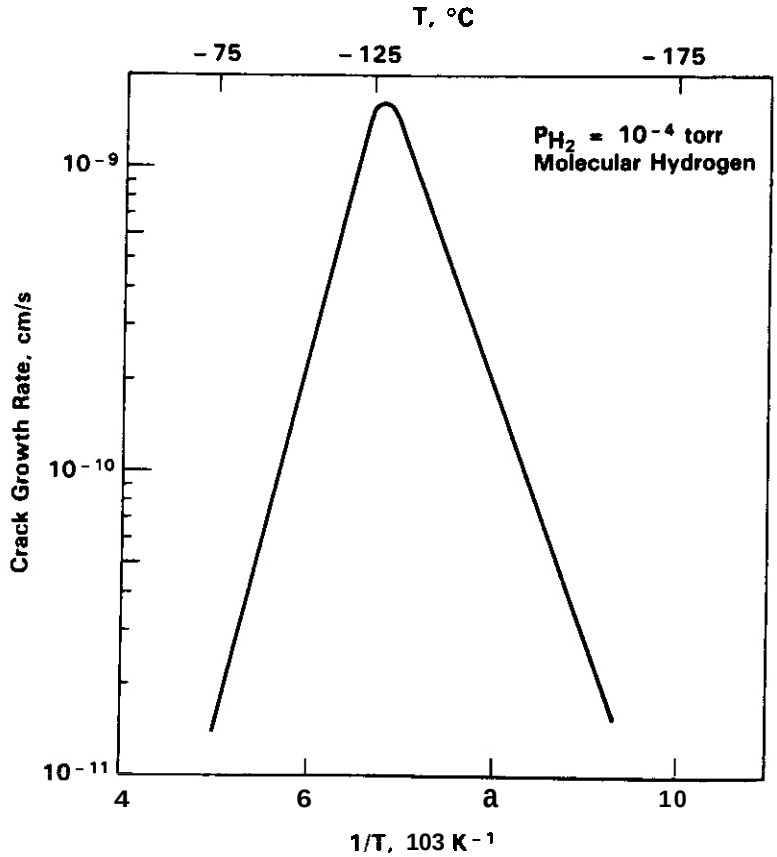

FIGURE 2. Calculated crack growth - 1/T relationship for *HT-9* in low pressure hydrogen approximating plasma hydrogen with molecular hydrogen.

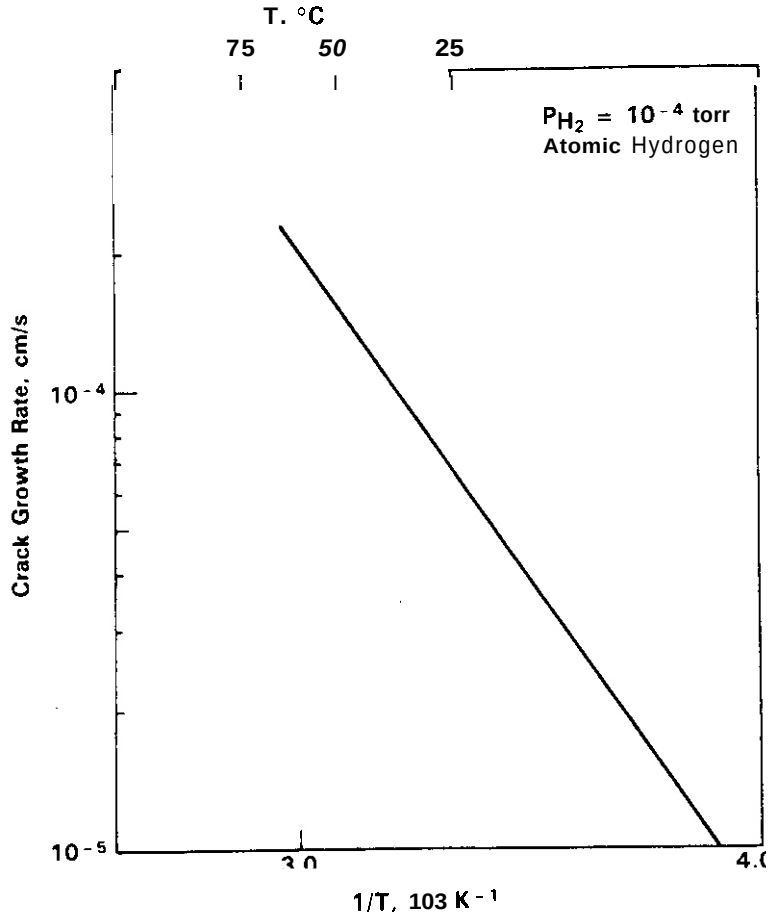

FIGURE 3. Calculated crack growth rate - 1/T relationship (low temperature regime only) for HT-9 in low pressure ionized hydrogen from the plasma.

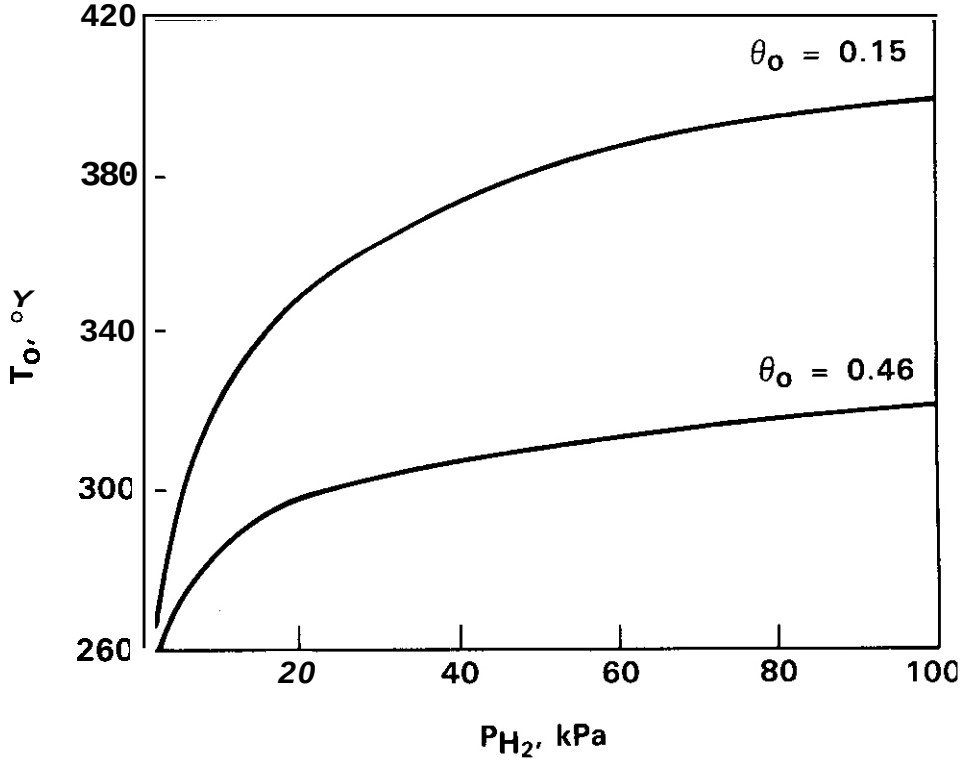

FIGURE 4. Critical temperature versus hydrogen pressure for two critical coverage values.

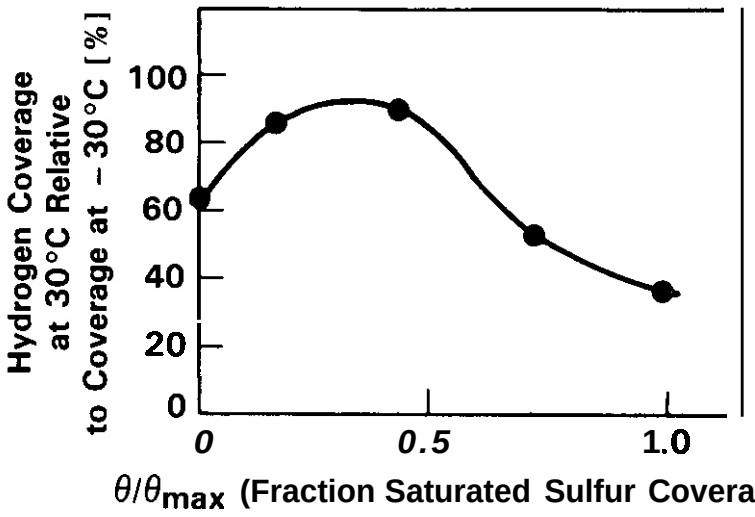

FIGURE 5. Surface hydrogen coverage on 4340 steel as a function of surface sulfur coverage.

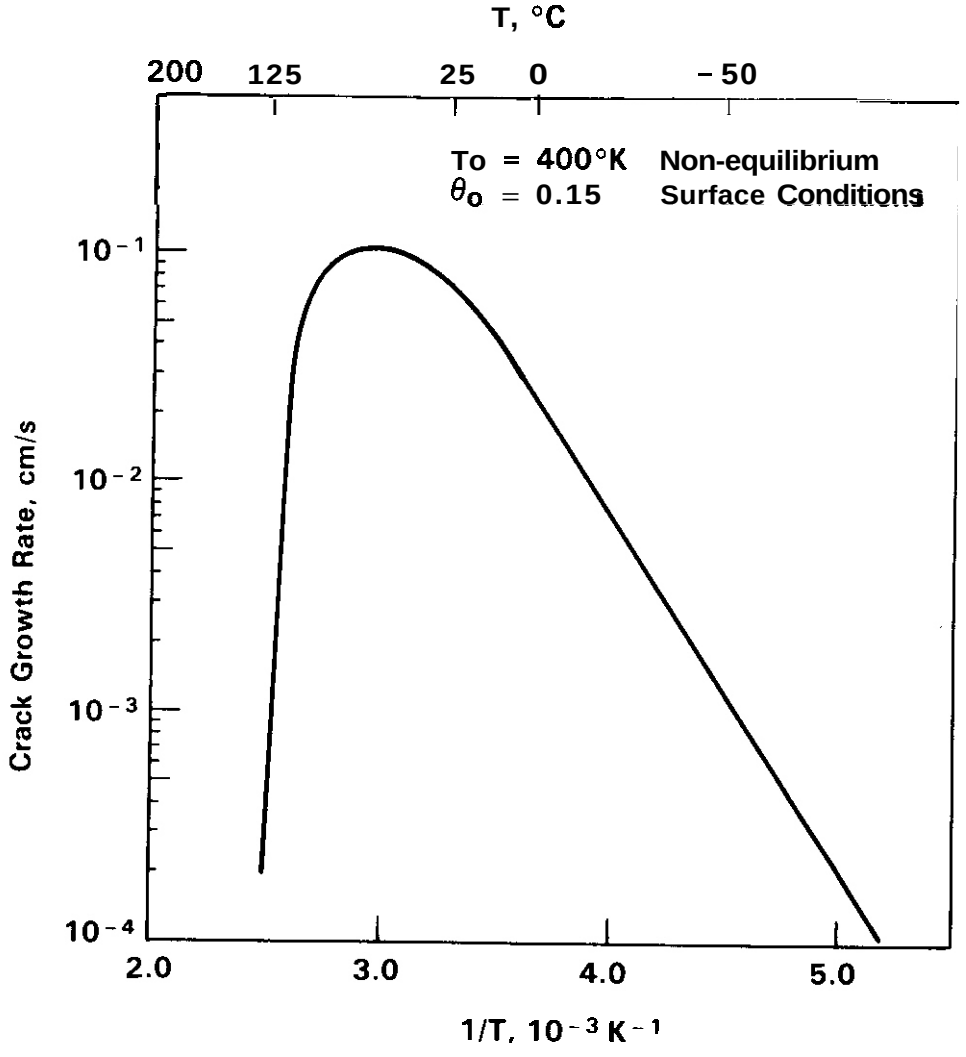

FIGURE 6. Calculated crack growth rate - 1/T relationship for HT-9 with non-equilibrium surface hydrogen coveraye.

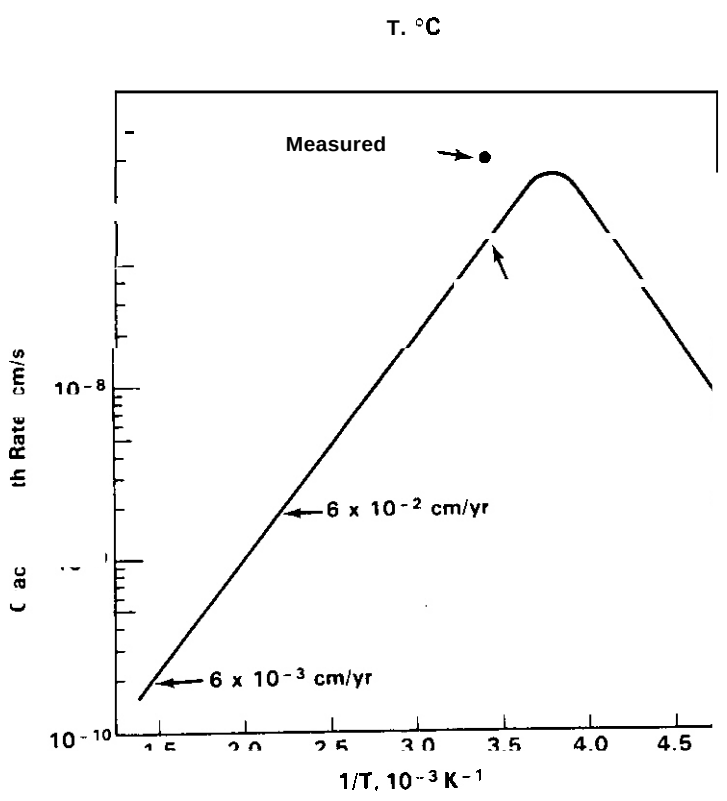

FIGURE 7. Calculated crack growth rate - 1/T relationship for **HT-9** in cathodic hydrogen.

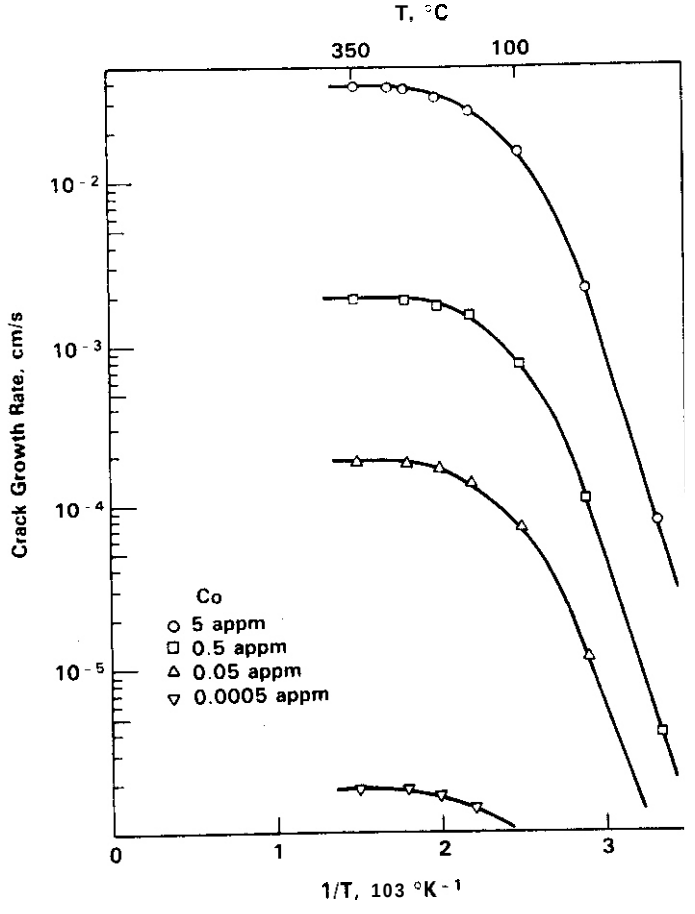

FIGURE 8. Calculated crack growth rate - 1/T relationship for HT-9 with variable steady state internal hydroyen concentrations.

THE RELATIONSHIP BETWEEN J-INTEGRAL AND CRACK TIP OPENING DISPLACEMENT

R. L. Simons and W. J. Mills (Hanford Engineering Development Laboratory)

1.0 Objective

The objective of this effort is to demonstrate the relationship between the critical J-integral value (J_{Ic}) and the critical crack tip opening displacement ($CTOD_c$).

2.0 Summary

Silicone replicas of the crack extension in compact tension (CT) specimens made of SS304 and SS316 were used to determine the critical crack tip opening displacement ($CTOD_c$). These values were used to test the relationship between J_{Ic}/σ_{ys} and $CTOD_c$. The best proportionality constant is ~2. Reasonable agreement between measured and calculated $CTOD_c$ using Wells' equation was found.

3.0 Program

Title: Irradiation Effects Analysis (AKJ)

Principal Investigator: D. G. Doran

Affiliation: Hanford Engineering Development Laboratory

4.0 Relevant OAFS Plan Task/Subtask

Subtask II.C.14 Models of Flow and Fracture

5.0 Accomplishments and Status

5.1 Introduction

Elastic plastic fracture toughness concepts are being used to characterize the fracture response of materials that exhibit appreciable plasticity prior to failure. Both the J-integral and crack tip opening displacement (CTOD) methods are used as fracture criteria when widespread plastic deformation is present in a material. Wells[1] introduced the CTOD concept as a measure of crack tip deformation prior to stable crack propagation. Extensive development of the J-integral approach to fracture was done by Rice.[2] Standard practices have been written for both approaches. In the United States the J-integral method is generally favored and it is described by the ASTM Standard E 813-81.[2] Outside the United States the CTOD method is used extensively (see for example British Standard BS 5762:1979).

Previous work[3] has suggested that J is related to CTOD and yield strength as

$$J_{Ic} = m\sigma_{ys}(CTOD_c) \quad (1)$$

The value of m for a non-strain hardening material under plane stress conditions should approach unity. For materials that exhibit substantial strain hardening, the value of m is expected to be much larger. Empirically deduced valves of m have ranged between 1 and 2.[4-7]

In this work, J_{Ic} fracture toughness data and critical crack tip opening displacement ($CTOD_c$) data are correlated for low strength, high work hardenable materials in an attempt to establish a relationship between these two fracture criteria.

5.2 Material Selection and Testing

The materials used in this work were solution annealed Type 316 and Type 304 stainless steels. Testing was done at room temperature. The yield strengths and ultimate strengths were 40.8 and 82.5 ksi for 316 SS and 32.9 and 89.9 ksi for 304 SS. The J_R valves were determined using deeply cracked CT specimens. The fracture toughness behavior was determined by the multiple-specimen J_R-curve technique. Specifically, compact specimens were loaded to various displacements producing different amounts of crack extension, Δa, and then unloaded. After unloading, each specimen was heat tinted to discolor the crack growth region and subsequently broke open so that amount of crack extension could be measured. The value of J for each specimen was determined from the load versus load-line displacement curve by the following equation: [2]

$$J = \frac{2A\,(1 + \alpha)}{Bb\,(1 + \alpha^2)} \qquad (2)$$

where: A = area under load versus load-line displacement curve

b = unbroken ligament size

$\alpha = [(2a/b)^2 + 2(2a/b) + 2]^{\frac{1}{2}} - (2a/b + 1)$

a = crack length

B = specimen thickness

The J_R-curves were constructed by plotting values of J as a function of Δa. The initiation J_C value was then taken to be that value where a least-squares regression line through the crack extension data points interesected the stretch zone line for low strength, high strain-hardening materials: [7]

$$J = 4\sigma_f(\Delta a)$$

where: σ_f = flow strength = $\frac{1}{2}(\sigma_{ys} + \sigma_{uts})$

σ_{ys} = 0.2% offset yield strength

σ_{uts} = ultimate tensile strength

The J_{IC} values are shown on Table I. The details of the experimental work will be reported at a later time.

Crack opening replicas were made after the CT specimens were tested and heat tinted by infiltrating the crack with a catalytically hardening silicone rubber commonly used to make dental impressions. This technique was first developed by Robinson and Tetelman.[4] The silicone rubber is poured into the notch with dams on each side of the CT specimen and allowed to harden. The specimen was then broken in half and the replica was removed and sectioned into quarters. The width of the replica was measured with a traveling difference microscope relative to the end of the precrack line traveling back into the precrack region -100 mils and out to the end of the crack tip. Reference 8 gives considerable detail on the preparation of silicone replicas of the crack.

5.3 Results and Discussion

Figure 1 shows results of replica thickness versus distance from the precrack tip for a 316 stainless specimen. The curve shows three characteristic regions: the precrack region at negative x values, the blunting region (or stretch zone) out to about 20 mils and the crack extension region beyond -20 mils. The curves are linear least squares fit to the data. The $CTOD_C$ at the precrack tip is the difference between the two curves at x = 0. In this case (specimen 1993) the average of three section measurements is 0.035 ± 0.014 inches. The uncertainty is the one standard deviation of the three measurements. The weighted average critical CTOD for SS316 is 0.030 ± 0.006 inches and for SS304 is 0.048 ± 0.013 inches. The measured CTOD, for six specimens are shown in Table 1.

It is noted that the SS304 specimens 1952 and 1954 showed very little crack extension while 1955 showed crack extension comparable to the SS316 specimens (-100 mils). Specimen 1955 also showed twice as large of $CTOD_C$ as the other two SS304 specimens. The consequences of this behavior of 1955 is a larger uncertainty in the SS304 data than the SS316 data.

The measured CTOD were compared to calculated values based on the Wells'[9] equation

$$CTOO = \frac{0.45\,(W-a)}{0.45W + 0.55a}\left[V_{LL} - \frac{\gamma\,\sigma_{ys}\,W\,(1-\nu^2)}{E}\right] \quad (2)$$

where W = specimen width

a = precrack length

V_{LL} = final load line displacement

γ = constant (2.5 for deeply cracked specimens)

σ_{ys} = yield strength

ν = Poisson's ratio (ν = 0.3)

E = elastic modulus (2.90 x 10^4 ksi)

The critical calculated CTOD was determined by an R curve technique (i.e., calculated CTOO versus Aa). The critical CTOD was taken at the Δa determined at the intersection of the J_R curve and blunting line. These values along with the measured J_{Ic} are shown in Table 1. The CTOD R curves are shown in Figures 2 and 3. A comparison of measured and calculated critical CTOD's are shown in Figure 4. They show fairly good agreement within experimental uncertainties. Elastic relaxation effects have not been made for in the measured values.

Evaluation of the relationship between J_{Ic} and $CTOD_c$ (Eq. 3) is shown by plotting J_{Ic}/σ_{ys} versus $CTOD_c$ in Figure 5. The two lines drawn correspond to different values of m. The m=l line corresponds to an elastic material with no work hardening, The m=2 time best fits the SS316 and SS304 data. The maximum m that would fall within the SS304 error bars is m=2.5. Mills[7] found that m=2 best fit several low and intermediate strength steels. The individual measurements are shown in Figure 5 as A's.

Steels with significant work hardenability require m>1. The yield strengths of SS304 and SS316 are 33 ksi and 40 ksi, respectively. The SS304 shows a higher work hardening coefficient than SS316 (0.56 and 0.32, respectively), and thus a correspondingly higher value of m is expected. These results are in qualitative agreement with the evaluation of Paranjpe and Banejee[10] who found m to increase linearily with the strain hardening exponent up to m=1.5. However, the increase was at a lower rate for hardening exponents >0.2.

5.4 Conclusions

Critical crack tip opening displacement ($CTOD_c$) were measured from silicone replicas of cracked compact tension specimens made of SS304 and SS316. .Measured $CTOD_c$ and calculated CTOD, based on Wells' equation were in close agreement. The relationship between J_{Ic} and $CTOD_c$ is proportional to a constant times yield stress. The best constant (m) appears to be equal to 2.

6.0 References

1. A. A. Wells, "Unstable Crack Propagation in Metals-Cleavage and Fast Fracture," Proceedings, Crack Propagation Symposium, Vol. 1, Cranfield, Fig. 1.

2. ASTM Standard, "J_{Ic}, A Measure of Fracture Toughness," ASTM E813-81, Part 10, American Society for Testing and Materials, pp. 822-840, 1982.

3. J. R. Rice, "A Path Independent Integral and the Approximate Analysis of Strain Concentration by Notches and Cracks," J. Appl. Mech. 35, 1968, p. 379.

4. J. N. Robinson and A. S. Telelrnan, "Measurement of K_{Ic} on Small Specimens Using Critical Crack Tip Opening Displacement," ASTM STP 559, (1974) pp. 139-158.

5. C. A. Griffis, "Elastic-Plastic Fracture Toughness: A Comparison of J-Integral and Crack Opening Displacement Characterizations," Journal of Pressure Vessel' Technology, 97, No. 4, Nov, 1975, pp. 278-283.

6. J. N. Robinson, "An Experimental Investigation of the Effect of Specimen Type on the Crack Tip Opening Displacement and J-Integral Fracture Criteria," International Journal of Fracture, 12, No. 1, (1979) pp. 45-53.

7. W. J. Mills, "On the Relationship Between Stretch lone Formation and the J-Integral for High Strain-Hardening Materials," Journal of Test and Evaluation, JTEVA, 9, No. 1, Jan. 1981, pp. 56-62.

8. C. F. Shih, et al., "Methodology for Plastic Fracture," Third Quarterly Report Nov 1, 1976 to Jan 31, 1977, General Electric Corp., Schenectady, New York, EPRINP1735.

9. A. A. Wells, "The Status of COD on Fracture Mechanics," in Third Canadian Congress of Applied Mechanics, Calgary, 1971, pp. 59-77.

10. S. A. Paranjpe and S. Banejee, "Interrelation of Crack Opening Displacement and the J-Integral," Engineering Fracture Mechanics, 11, (1979), pp. 43-53.

7.0 Future Work

Additional CTOD measurements will be made to improve the measurement statistics. Application to other low and intermediate strength steels is planned to expand the data base.

8.0 Publications

None.

TABLE 1

CTOD DATA FOR SS316 AND SS304

Steel	Specimen No.	Measured Mean $CTOD_c$ (inches)	$CTOD_c$ (inches)	Calculated $CTOD_c$	J_{Ic} (ksi inch)
SS316	2000	0.025±0.005			
1993		0.035±0.014	0.03020.006	0.041	2.27±0.17
1985		0.035±0.006			
55304	1954	0.042±0.006			
1952		0.03620.004	0.04820.013	0.044	2.96'0.29
1955		0.071±0.005			

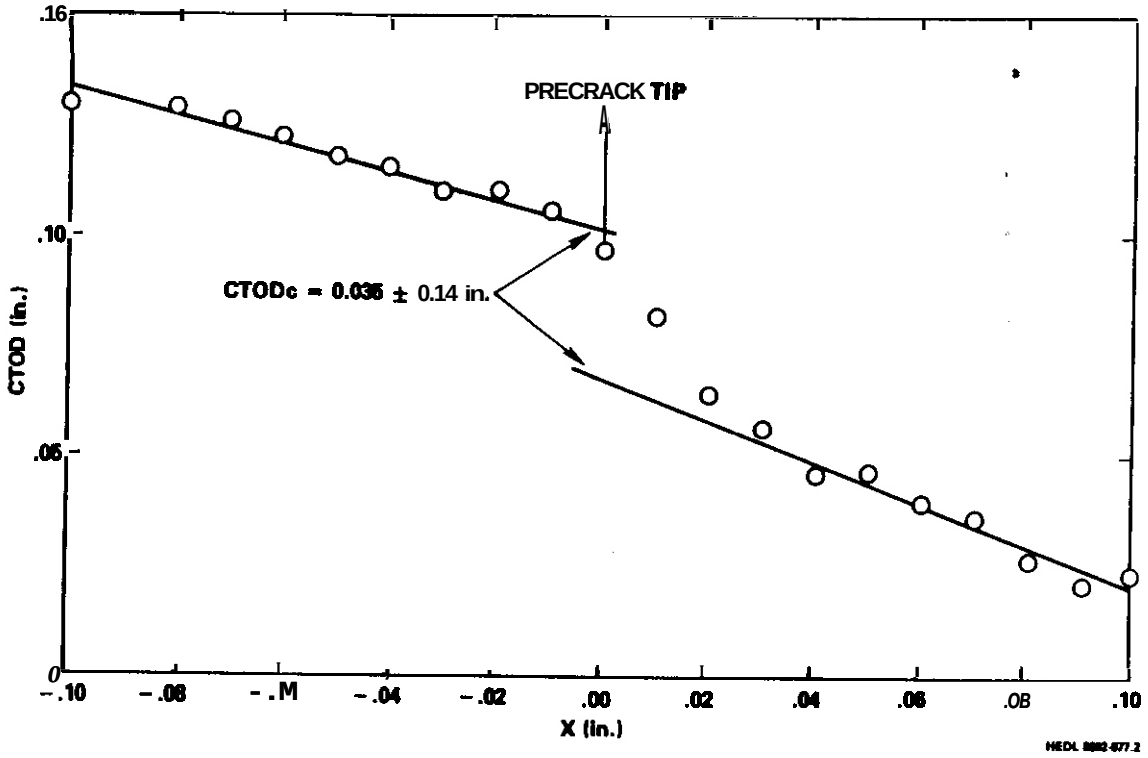

FIGURE 1. CTOD As A Function Of Crack Depth In 316 Stainless Steel Specimen Number 1993.

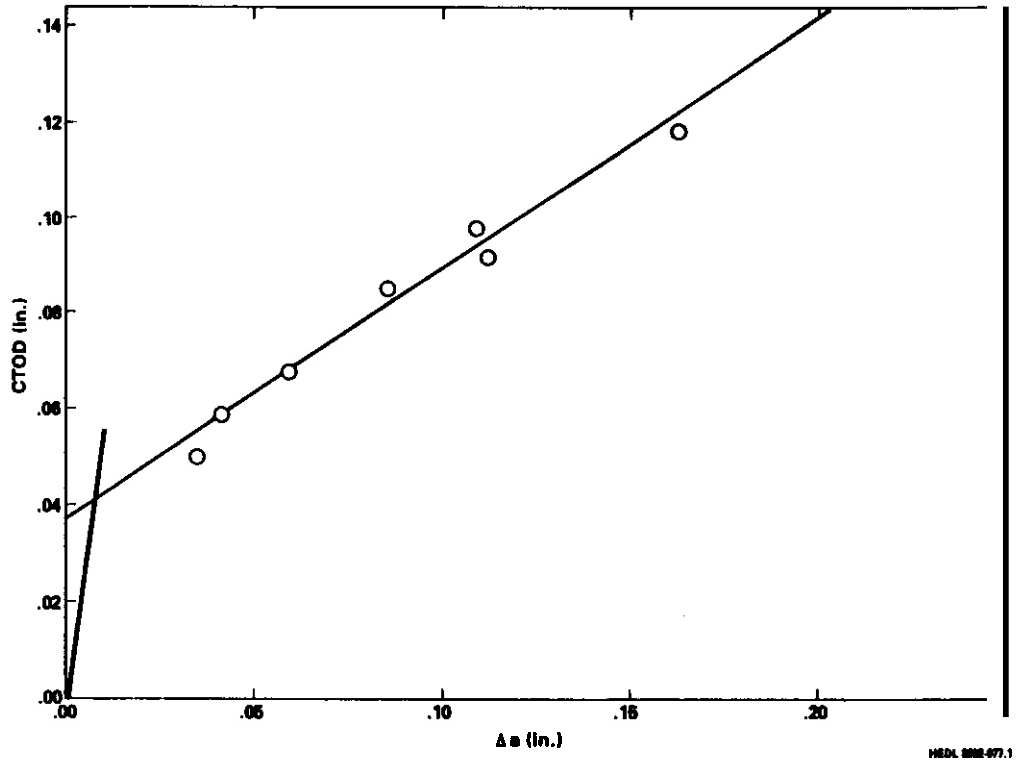

FIGURE 2. Calculated CTOD In 316 Stainless Steel By R Curve Analysis.

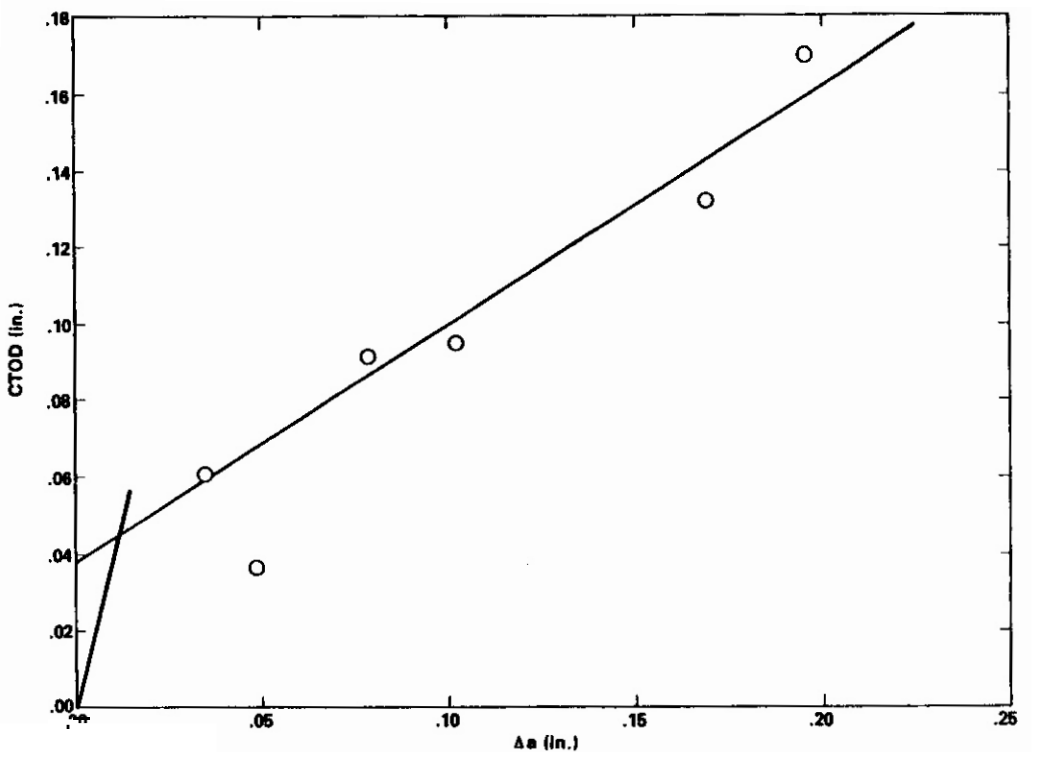

FIGURE 3. Calculated CTOD In 304 Stainless Steel By R Curve Analysis.

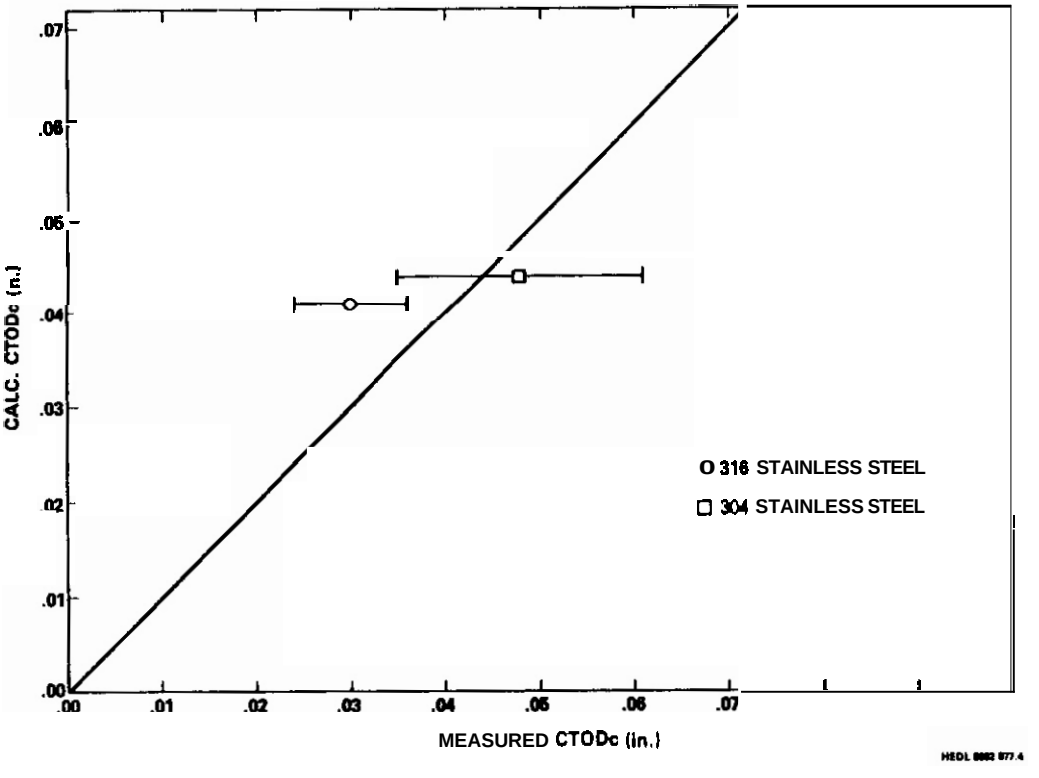

FIGURE 4. Comparison Of Calculated And Measured $CTOD_c$.

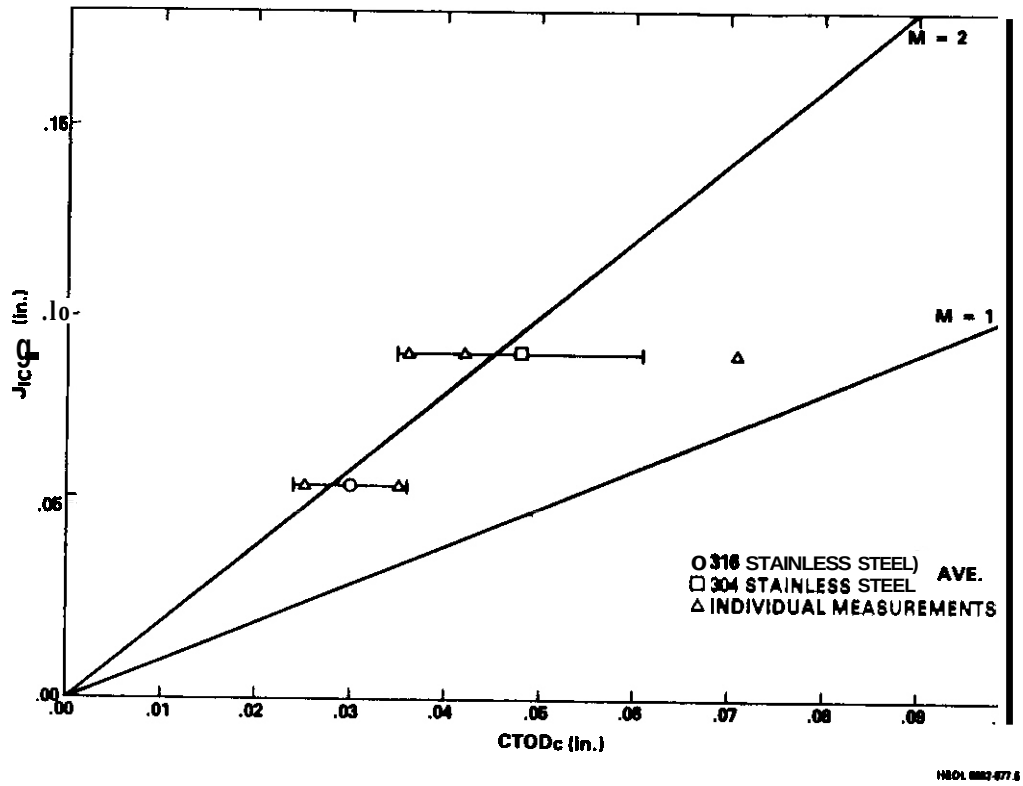

FIGURE 5. Evaluation Of The Constant Of Purpertimatility Between J_{1c} And $CTOD_c$.

CHAPTER 5

RADIATION EFFECTS MECHANISMS AND CORRELATIONS

OWR/RTNS-II LOW EXPOSURE SPECTRAL EFFECTS EXPERIMENT

H. L. Heinisch, S. O. Atkin and C. Martinez (Hanford Engineering Development Laboratory)

1.0 Objective

The objective of this experiment is to determine the effect of the neutron spectrum on radiation-induced changes in mechanical properties for metals irradiated with fusion and fission neutrons.

2.0 *Summary*

The status of the OWR/RTNS-II Low Exposure Spectral Effects Experiment is reviewed. Irradiations in RTNS-II and OUR at 90°C and 290°C have been completed. The results of tensile tests on AISI 316 stainless steel, A302B pressure vessel steel and pure copper are reported here. The radiation-induced changes in yield strength as a function of neutron dose in each spectrum are compared. The data for 316 stainless steel correlate well on the basis of displacements per atom (dpa), while those for copper and A302B do not. In copper the ratio of fission dpa to fusion dpa for a given yield stress change is about three to one. In A302B pressure vessel steel the fission to fusion ratio is more than three at lower fluences, but the fission and fusion yield stress data appear to coalesce or intersect at the higher fluences.

3.0

Title: Irradiation Effects Analysis
Principal Investigator: D. G. Doran
Affiliation: Westinghouse Hanford Company

4.0 Relevant OAFS Program Plan Task/Subtask

Subtask	II.B.3.2	Experimental Characterization of Primary Damage State; Studies of Metals
Subtask	II.C.6.3	Effects of Damage Rate and Cascade Structure on Microstructure; Low-Energy/High Energy Neutron Correlations
Subtask	II.C.16.1	14-MeV Neutron Damage Correlation

5.0 Accomplishments and Status

5.1 Introduction

This is a report of the first results from an experiment to determine quantitative differences in the effects of RTNS-II and fission reactor neutrons on the changes in tensile properties and microstructure of metals irradiated to exposures < 0.1 displacements per atom (dpa). Irradiations were performed at the RTNS-II and at the Omega West Reactor (OWR) at Los Alamos National Laboratory. The materials irradiated represent several categories of pure metals and engineering alloys. Results of tensile tests of some of the irradiated materials are presented here. Details of the experiment and some early results have been described in previous reports[1-3].

Data from previous experiments comparing the effects on tensile properties of fusion neutrons and fission reactor neutrons in copper[4] and stainless steel[5] indicate the existence of spectral effects that cannot be accounted for simply on the basis of displacements per atom (dpa).[6] The earlier fission and fusion irradiations were conducted at different temperatures (65°C and 25°C respectively), so in correlating the data some assumption must be made regarding the magnitude of any temperature dependence.

The earlier experiments attained very low fluences in RTNS-I (<0.001 dpa). One of the goals of the present experiment is to extend the investigation of spectral effects to a higher fluence range, while having the same irradiation temperature in each spectrum. A more general goal is to provide data for a systematic study of spectral effects with respect to the categories of pure metals and structural alloys, austenitic and ferritic materials, and annealed and cold worked conditions. The results of tensile tests on AISI 316 stainless steel, A3020 pressure vessel steel and pure copper will be discussed in this report

5.2 Materials

An important concern in the selection of materials for this experiment was that the expected relative change in yield strength at low exposures would be large enough that the irradiation effects could be easily distinguished. High strength ferritic alloys for example. were omitted; ferritic materials are represented by pure iron and pressure vessel steel. Another concern in materials selection was to take advantage of the existing body of radiation effects data. Table 1 summarizes the materials and their ore-irradiation conditions.

TABLE 1

MATERIALS FOR LOW EXPOSURE SPECTRAL EFFECTS EXPERIMENT

Material	Composition	Heat Treatment	ASTM Grain Size
cu	99.999% cu	450 C, 15 min Air Cooled	7
Fe	99.99 % Fe 30 oom O 20 ppm N 12 ppm C	800 C (UHV), 2 h Furnace Cooled	8
AISI 316 (N-lot)	16.45wt% Cr 13.48 Ni 2.48 Mo 1.59 Mn 0.48 Si 0.15 other balance Fe	1000 C, 10 min Air Cooled	6
AISI 316 (N-lot)		20% cold worked	6.5
A3020	1.34wt% Mn 0.51 Mo 0.24 C 0.23 Si 0.20 Cu 0.18 Ni 0.11 Cr 0.13 other balance Fe	As Received	8

5.3 Irradiation Temperatures

One of the aims of this experiment is to study temperature effects. Irradiations were done at 90°C and 290°C in both OWR and RTNS-II. In addition, some copper and 316 stainless steel specimens were irradiated in RTNS-II at 25°C.

The choice of temperatures was limited to those that could easily be maintained in the available irradiation facilities. The lower temperature, 90°C, was essentially dictated by the OWR coolant temperature, the gamma heating rate, and the capabilities of the In-core Reactor Furnace built at Lawrence Livermore National Laboratory. The high irradiation temperature, 290°C, was chosen as one at which defects become significantly more mobile, yet not so high that the residual damage in all the materials is negligible at

these low fluences. With respect to defect kinetics, 290°C can be considered a relatively high temperature for copper, lower for 316 stainless steel, and intermediate for iron and A3026 steel. A large data base exists for A3026 at 290°C, which makes this a desirable temperature. The two temperatures, 90°C and 290°C, are comfortably within the operating range of the Dual-temperature, Vacuum-insulated (DTVI) furnace used for the RTNS-II irradiations.

5.4 Irradiations

Tensile specimens were irradiated using the HEDL dual-temperature, vacuum-insulated furnace in two joint US/Japan RTNS-II runs, R-1 to a peak fluence of 2.4 x 10^{18} n/cm^2 and R-2 to a peak fluence of 8.8 x 10^{18} n/cm^2. The neutron flux decreases rapidly with distance from the source, so specimens with doses (and dose rates) ranging over two orders of magnitude were obtained in each run. Specimens of copper and annealed AISI 316 stainless steel were also irradiated at room temperature to fluences from 7 x 10^{17} to 1.3 x 10^{18} n/cm^2 in a Japanese-sponsored RTNS-II irradiation. Tensile specimens for this experiment are also included in the joint Japan/US long-term irradiation (to 1 x 10^{19} n/cm^2) now underway at RTNS-II using the Japanese dual-temperature furnace at 200°C and 450°C.

The eight planned OWR irradiations have been completed, to four fluences each at 90°C and 290°C. The highest OWR fluence, 1.3 x 10^{20} n/cm^2, is slightly higher in dpa than the highest RTNS-II dose. So far, tensile specimens from only six of the OWR irradiations have been tested.

The OWR irradiations use the In-Core Reactor Furnace developed at Lawrence Livermore National Laboratory specifically for OWR irradiations. Temperatures of the specimens are maintained by balancing nuclear heating, coolant flow through the furnace, and resistance heating near the specimens. In the lower irradiation temperature region (including 90°C) the furnace utilizes the reactor coolant water to maintain the required temperature, while at the higher temperatures a flow of helium gas is used. The resistance heater within the furnace provides precise control of the temperatures.

The tensile specimens are contained in helium-filled aluminum capsules developed at HEDL that were designed to provide well-controlled specimen temperatures by minimizing temperature gradients caused by nuclear heating. One capsule contained thermocouples directly welded to specimens so that a correlation among the furnace, capsule, and specimen temperatures could be determined. Measurements with this capsule in the reactor showed that temperatures can be controlled during a run to within 2°C, and that the absolute specimen temperatures can be determined to within five degrees at both 90°C and 290°C. The dosimetry in the OWR capsules consisted of wires of Fe, Ni, Ti and 0.1%-Co-Al, supplied and analyzed by L.R. Greenwood at Argonne National Laboratory. The neutron fluences determined from the dosimetry have an estimated uncertainty of 10%.

5.5 Tensile Testing

Flat, miniature tensile specimens were prepared from each material. The specimens are 12.7 x 2.54 x 0.254 mm overall, with a gauge section of 5.10 x 1.03 x 0.254 mm. The specimens were punched from sheets of material, polished to remove burrs, engraved with identification, and heat treated as indicated in Table 1. The A3028 specimens were punched from sheets that were sliced from a bar of material. Consequently, they do not have thicknesses that are as uniform as those punched from rolled sheet stock. Even with uniformly rolled sheet stock, the acts of punching and polishing can create a dispersion in the thicknesses of specimens from the same sheet. This dispersion is a trade-off for the ease of preparing large batches of specimens inexpensively in a short time. The thickness of each specimen is measured with an electronic thickness probe prior to testing. The largest single source of deviation in the tensile data is uncertainty in the values of the cross-sectional areas of the gauge sections that are used to calculate the tensile stresses.

Tensile tests were performed at room temperature using a horizontal tensile frame designed specifically for miniature specimens.[7] All tests were performed with a free-running cross-head speed of 2.5 x 10^{-6} m/s. The load and displacement test data are collected in both digital and analog form. The 0.2% offset yield stress, ultimate tensile strength and uniform elongation are determined by computer from the digital data. Anomalies are resolved by graphical analysis of the analog data. Control specimens of AISI 304 stainless steel are regularly tested; results fall within a 2-sigma band of ± 6% for both yield stress and ultimate tensile strength.

Miniature tensile specimens have been shown to give valid bulk property measurements as determined from standard size specimens.[8] Effects of grain size are a critical issue. The "rule of thumb" requires a minimum of ten grains across the smallest gauge dimension, but apparently valid results have been obtained in stainless steel with as few as 2-3 grains.[9] The largest grain size of the materials tested here (for 316 stainless steel; see Table 1) corresponds to an average of 5 grains across the specimen thickness.

5.6 Results

The data presented here consist of the radiation-induced changes in 0.2% offset yield stress as a function of neutron fluence. Curves have been fitted to the data in most of the figures, primarily to illustrate the trends in the data. Functions linear in the square root of the fluence and in the fourth root of the fluence were fitted. In general, the difference in fit between the square root and fourth root functions is small. Models of irradiation strengthening predict different fluence dependencies of the yield stress change, depending on the mechanisms in effect. Although no attempt is made here to determine the mechanisms in each case, the fluence dependencies of the best-fitting curves are noted.

In Fig. 1 the change in yield stress of RTNS-II irradiated copper is displayed at three temperatures, 25, 90, and 290°C. Data from both R-1 and R-2 are included; doses in R-2 were obtained at one-fourth the dose rate in R-1. The uncertainty of each data point is estimated to be ± 5% of the absolute yield stress, or about ± 10 MPa. This is indicated by error bars drawn on one point near the middle of the data. At 90°C strengthening of up to 3 times the unirradiated yield stress takes place at these fluences. At 290°C there is minimal effect of the irradiation in this fluence range, but the trend in the data shows a slight increase at the higher fluences, indicating perhaps the onset of more substantial radiation-induced strengthening at even higher fluences.

The curve at 90°C in Fig 1 is fitted to the data of R-1 only, and it is linear with the fourth root of the fluence. The other lines in Fig 1 are not fitted, but simply show the trend of the data. The yield stress data from the 25°C irradiation, having about the same dose rate as R-1, are at the upper edge of the scatter of the data at 90°C. They are, however, uniformly higher than the 90°C values by about 15 MPa, indicating either an irradiation temperature effect or some unexpected systematic difference.

Figure 2 shows the change in yield stress as a function of fluence for solution annealed 316 SS irradiated at the RTNS-II at 25°C, 90°C and 290°C. The uncertainty, indicated by error bars on a single point, is estimated to be ± 5% of the absolute yield stress, or about ± 17 MPa at the middle of the range. At these fluences the maximum change in the yield stress is about 50% of the value of the yield stress of the unirradiated material.

There is no separation between the sets of data taken from R-1 and R-2 at either temperature. As with copper, the yield stress change increases more rapidly with fluence at 90°C, while the yield stress change at 290°C is minimal. However, for 316 SS at 290°C there is a significant increase in yield stress at the higher fluences. The curves in Fig 2, linear in the fourth root of the fluence, were fitted to the combined R-1 and R-2 data at each temperature. The data at 25°C are uniformly higher than the 90°C data, but lie within their scatter. The evidence for a temperature effect in this range is less compelling for 316 SS than for copper.

The change in yield stress as a function of neutron fluence for A302B pressure vessel steel irradiated in RTNS-II is shown in Figure 3. The 5% uncertainty for A302B is about ± 30 MPa and is indicated by error bars on a single point. Within this fluence range the maximum change in yield stress is about 30% of the yield stress of the unirradiated material. The 90°C and 290°C data diverge beyond the scatter of the data only at the higher fluences. The data for A302B were better fit by curves linear in the square root of the fluence.

In Figs. 1-3 the data from R-1 and R-2 are shown as separate sets of points at each temperature. Fluences in the R-1 irradiation were achieved at a rate 4 times higher than for R-2. In copper (Fig 1) the data from R-2 lie uniformly below those from R-1. At the lower fluences the differences are within the uncertainty in the data, but at the higher end some divergence is noticeable at both 90°C and 290°C. In 316 SS and A302B there is no discernable difference between the R-1 and R-2 data at either temperature.

In Figs. 4-8 the changes in yield stress due to irradiation in RTNS-II and OWR are plotted as a function of dpa, using spectral averaged displacement cross sections calculated with the NJOY nuclear data code.[10] The displacement cross sections for copper are 293 b and 3699 b for OWR and RTNS-II respectively. For AISI 316 stainless steel they are 230 b and 2782 b, and for A302B pressure vessel steel they are 222 b and 2810 b for OUR and RTNS-II respectively. The cross sections are calculated on the basis of total neutrons; in OUR 31% of the neutrons have energies greater than 0.1 MeV.

Figure 4 contains yield stress data for copper at 90°C. The lines are fitted to the R-1 and OWR data points, and are linear in the fourth root of dpa. The yield stress changes resulting from the two spectra clearly do not correlate on the basis of dpa. The fission reactor neutrons require about 2.9 times more dpa to produce the same strengthening in copper as the D-T neutrons. If the R-2 data alone are compared to OWR, a factor of only 1.8 is obtained. Data has not yet been obtained from copper specimens irradiated in OWR at 290°C.

Figs. 5 and 6 show yield stress changes for solution annealed 316 SS at 90°C and 290°C, respectively, plotted as a function of dpa. At 90°C the RTNS-II data and the OWR data correlate very well in this fluence range. At 290°C there are data at only two OWR fluences. While the OWR data tend to fall slightly below the RTNS-II data, little can be concluded until the higher fluence OWR data are obtained. The curves in Fig 5 and 6 are fitted to the data at both temperatures, and they vary linearly with the fourth root of dpa.

Figs. 7 and 8 show data for A3028 pressure vessel steel at 90°C and 290°C respectively. At 90°C the OWR and RTNS-II data do not correlate on the basis of dpa in this fluence range. The data are fitted best by curves that vary with the square root of dpa. The curves, if extended, intersect at about the highest fluence point in the OUR data. At 290°C the data at the two OUR fluences fall among the RTNS-II data.

5.7 Discussion

Effects of the irradiation temperature are observed in the RTNS-II irradiations of all three materials investigated here. In copper the D-T neutrons require about 25% greater fluence at 90°C to achieve the same strengthening as at 25°C. The difference in behavior at 25°C and 90°C can be attributed to the sensitivity of defect migration to these temperatures. The lack of irradiation strengthening in copper at 290°C is probably due to the instability of clusters at this temperature. This temperature is within "Stage V" of resistivity recovery experiments on copper,[11] which is usually attributed to the breakup of vacancy clusters.

In 316 SS any differences in behavior at 25°C and 90°C are lost in the scatter of the data. An irradiation temperature effect is not anticipated in 316 SS at this temperature range. In 316 SS there is apparently much less irradiation strengthening at 290°C than at 90°C. However, if the R-2 data at 290°C in Fig 2 are displaced to the left by about an order of magnitude in fluence, they fall on the curve fitted to the 90°C data. Thus, at 290°C the onset of irradiation strengthening is delayed, but then proceeds at the same rate per unit fluence as at 90°C. This behavior can be confirmed when the higher fluence 290°C data from OUR are available.

In A3028 the large scatter in the data precludes the clear identification of irradiation temperature effects, although the fitted curves in Fig 3 are an attempt to separate the 90°C and 290°C data. At the higher temperature the onset of irradiation strengthening is apparently also delayed in A302B.

The change in yield stress of fission and fusion neutron irradiated solution annealed 316 SS correlates well on the basis of dpa. There is no evidence of additional spectral effects or rate effects in the data presented here. This is in contrast to the data of Vandervoort. et al.,[5] in which fusion neutrons were observed to have about 1.7 times the strengthening effect of the fission neutrons.[6] The difference in strengthening observed in their results cannot be accounted for on the basis of the different irradiation temperatures (25°C and 65°C for fusion and fission neutrons respectively), since the present experiment shows no temperature effects on the yield stress in the range from 25°C to 90°C (see Fig 2).

In annealed copper D-T fusion neutrons from RTNS-II were found to be more effective than fission reactor neutrons in radiation strengthening at 90°C. OUR requires 1.8-2.9 times more dpa to produce the same yield stress change as in RTNS-II, depending on the damage rate. This is comparable to the value of 2.3 determined by Mitchell et al.,[4] in the earlier work comparing room temperature RTNS-I irradiations and 65°C fission reactor irradiations.

There is evidence in the 90°C copper data that the damage rate may have an effect on radiation strengthening, since the yield stress changes for R-2 are uniformly 10% less than those from R-1, which has four times the damage rate at each fluence. The damage rate is different for each specimen in the RTNS-II irradiations, varying from 3×10^{-11} to 3×10^{-9} dpa/s, while in OWR all specimens were exposed at 5×10^{-8} dpals. Thus, comparing R-1 and R-2, the higher rate at each exposure leads to more strengthening, while the much higher rate of OWR results in much less strengthening. Any model that accounts for the observed differences in yield stress changes on the basis of rate effects would have to explain this behavior.

In A3028 the RTNS-II and OWR data also are not correlated on the basis of dpa, but the situation is somewhat different than in copper (see Fig 7). At the lower fluence values the RTNS-II neutrons are more than three times as effective at strengthening as the OWR neutrons. However, the data for the two spectra appear to intersect or coalesce at higher fluence values. Data at higher fluences is needed, but unfortunately there are no A3028 specimens irradiated to higher fluences in RTNS-II. There are, however, additional untested specimens that may help define the behavior in the limited fluence rdnge available. There is no evidence for rate effects in the RTNS-II data for A302B.

5.8 Conclusions

1. Irradiation-induced changes in yield stress from fission and fusion neutrons can be correlated on the basis of dpa in annealed AISI 316 stainless steel. There is no evidence for irradiation temperature effects below 90°C, and no evidence for damage rate effects.

2. Dpa is not an effective correlation parameter for irradidtion-induced yield stress changes in annealed copper. There are measurable temperature effects, as well as possible rate effects, at temperatures below 90°C.

3. Dpa is not an effective correlation parameter for irradiation-induced yield stress changes in A3028 pressure vessel steel in the fluence range investigated. There is evidence that dpa may correlate the yield stress changes at doses above 0.03 dpa. There is no evidence for damage rate effects in the fusion neutron data.

5.9 Acknowledgments

The authors gratefully acknowledge the contributions of all who aided in the successful performance of this experiment. In particular we are indebted to J. S. Pintler for performing tensile tests, to N. E. Harding and to the RTNS-II staff for RTNS-II irradiations, to R. A. VanKonynenburg and M. W. Guinan for the In-core Reactor Furnace, to D. L. Greenslade for the OWR capsules, to the OWR staff for irradiations, and to R. L. Simons and D. G. Ooran for valuable discussions. RTNS-II irradiations were performed under the US-Japan Collaboration Program for Operation and Utilization of the RTNS-II. This work was sponsored by the USDOE, Office of Energy Research, Office of Fusion Energy, under Contract No. DE-AC06-76FF02170.

6.0 References

1. H. L. Heinisch and S. D. Atkin, DAFS Quarterly Progress Report, January-March, 1984, U. S. Department of Energy, DOE/ER-0046/17, 76 (1984).

2. H. L. Heinisch, DAFS Quarterly Progress Report, July-September, 1985, U. S. Department of Energy, DOE/ER-0046/23, 58 (1985).

3. H. L. Heinisch and J. S. Pintler. DAFS Quarterly Progress Report, October-December, 1985, U. S. Department of Energy, DOE/ER-0046/24 (1986).

4. J. O. Mitchell, R. A. VanKonynenburg, C. J. Echer and D. M. Parkin, Radiation Effects and Tritium Technology for Fusion Reactors, J. S. Watson and F. W. Wiffen, eds, Gatlinburg, Tenn., 11. 172 (1975).

5. R. R. Vandervoort, E. L. Raymond and C. J. Echer, Rad. Effects, 45 (1980).

6. H. L. Heinisch and R. L. Simons, DAFS Quarterly Progress Report, Jan-Mar 1982, DOE/ER-0046/9, 147 (1982).

7. N. F. Panayotou, S. O. Atkin and R. J. Puigh, Proceedings of the ASTM Symposium on Use of Nonstandard, Subsized Specimens for Irradiation Testing, Albuquerque, NM, Sept. 23, 1983, ASTM STP 888 (1986).

8. N. F. Panayotou, "Oesign and Use of Nonstandard Specimens for Irradiation Testing," Proceedings of the ASTM Symposium on Nonstandard, Subsized Specimens for Irradiation Testing, Albuquerque, NM, Sept. 23, 1983, ASTM STP 888 (1986).

9. N. Igata et al., "The Specimen Thickness Effects on the Strength Properties of Austenitic Stainless Steels," Proceedings of the ASTM Symposium on Nonstandard, Subsized Specimens for Irradiation Testing, Albuquerque, NM, Sept 23, 1983, ASTM STP 888 (1986).

10. R. E. MacFarlane, R. J. Barrett, D. U. Muir and R. B. Boccourt, The NJOY Nuclear Data Processing System, Yol. I: Users Manual, LA-75844. Los Alamos National Laboratory (1978).

11. W. Schilling, P. Ehrhart, and K. Sonnenberg, Proceedings of the International Conference on Fundamental Aspects of Radiation Damage in Metals, Gatlinburg, Tenn, Oct., 1975. M. T. Robinson and F. W. Young, eds, USEROA CONF-751006, p. 470, (1976).

7.0 Publications

A report on this work will be presented at the Second International Conference on Fusion Reactor Materials in Chicago, April 13-17, 1986.

8.0 Future Work

Tensile tests will be done on specimens now available from the 290°C irradiations in OWR and on specimens from the 200/450°C RTNS-II irradiation soon to be completed. Additional information will be obtained from microscopy and resistivity measurements.

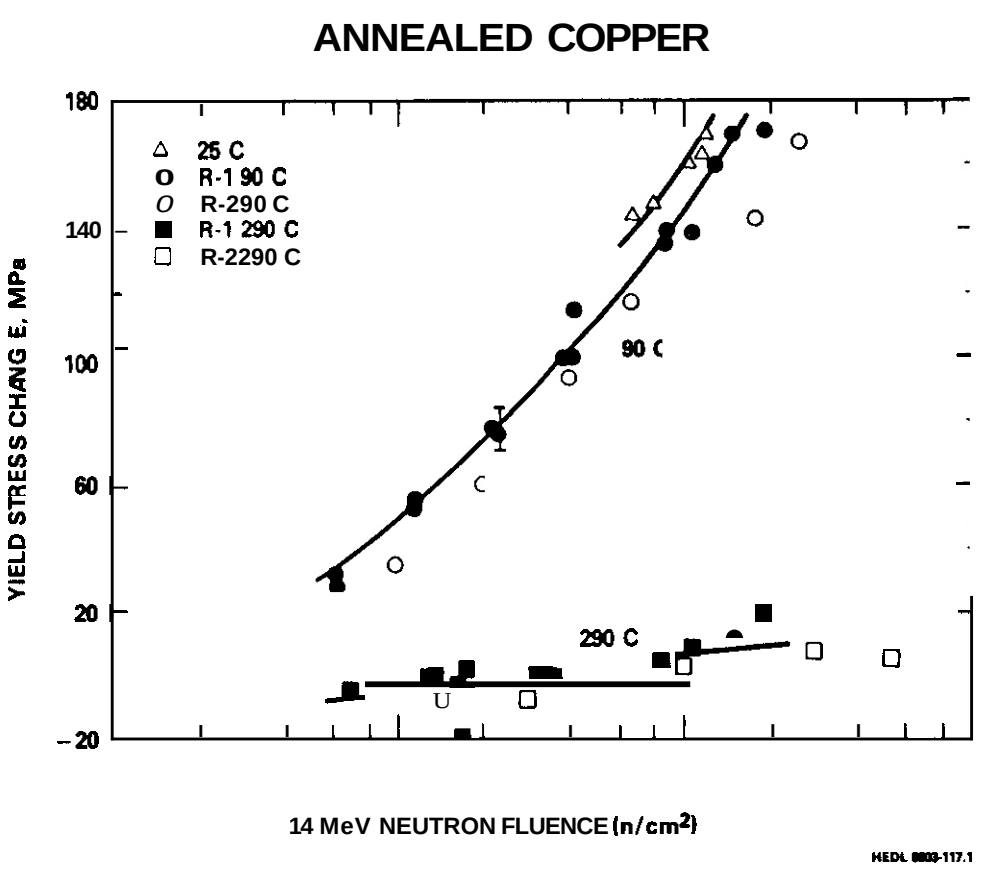

FIGURE 1. Change in Yield Stress of Annealed Copper as a Function of 14 MeV Neutron Fluence.

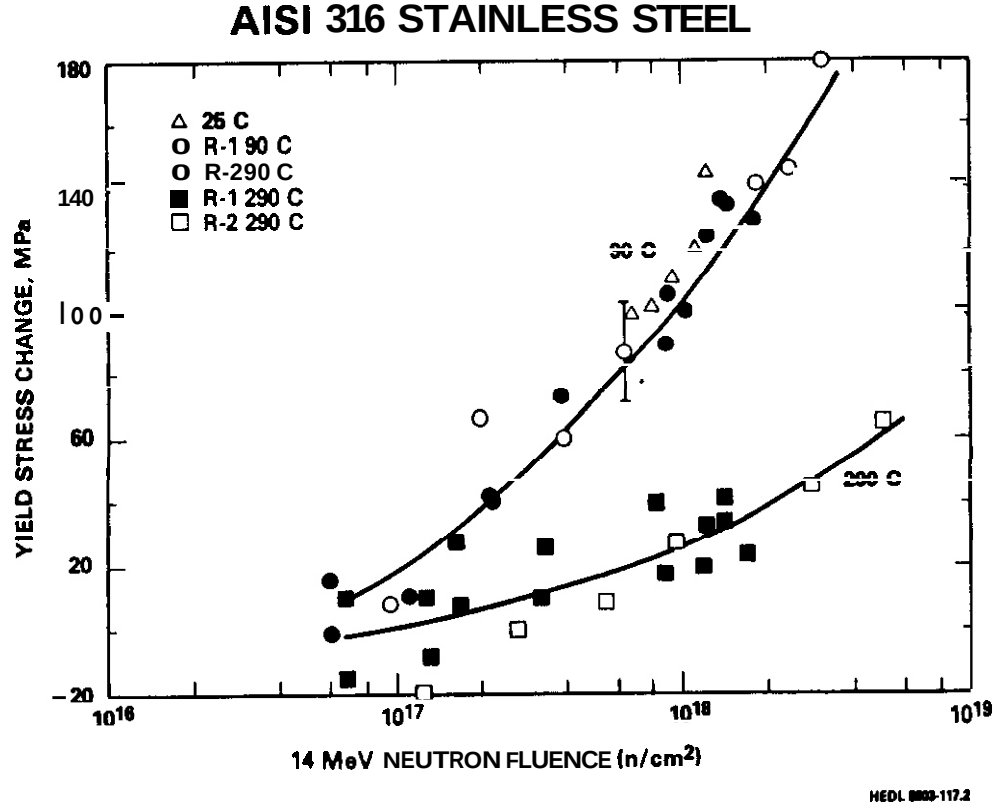

FIGURE 2. Change in Yield Stress of Annealed AISI 316 Stainless Steel as a Function of 14 MeV Neutron Fluence.

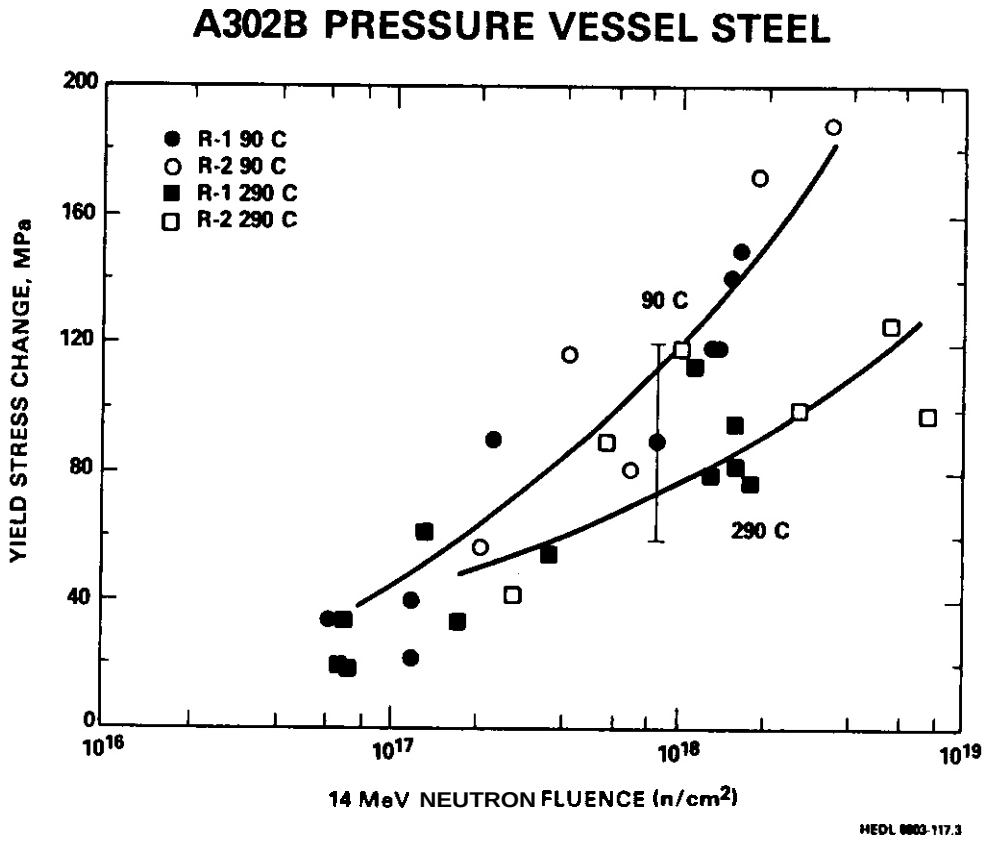

FIGURE 3. Change in Yield Stress of A302B Pressure Vessel Steel as a Function of 14 MeV Neutron Fluence.

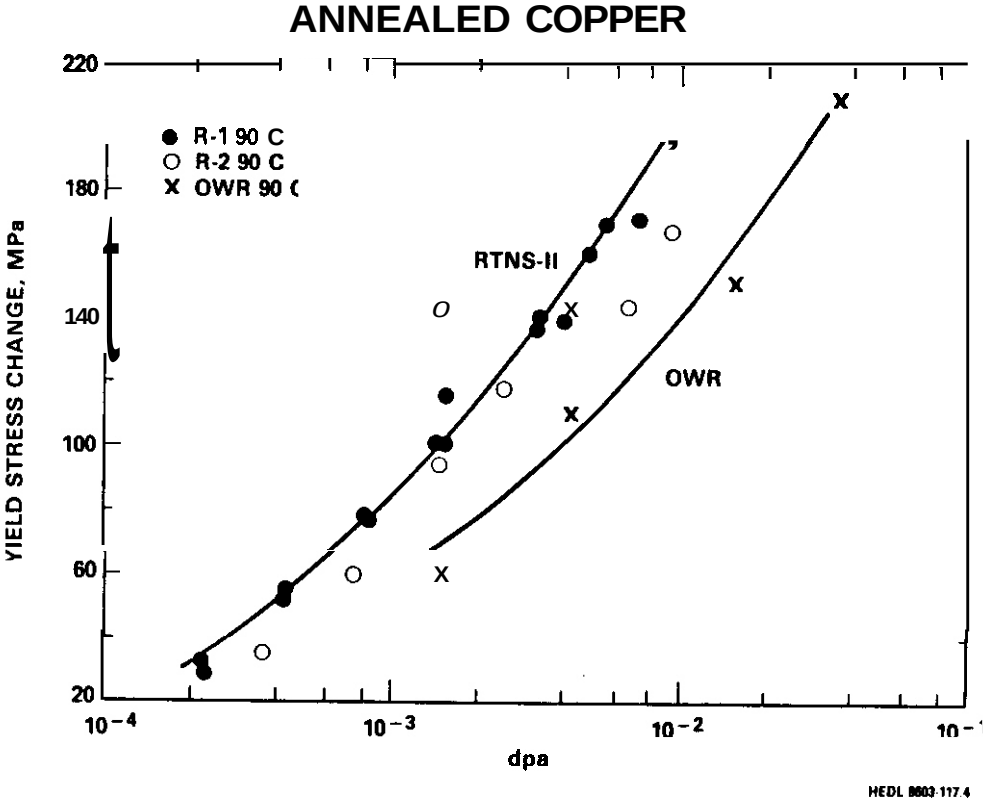

FIGURE 4. Change in Yield Stress of Annealed Copper as a Function of DPA for RTNS-II and OWR Irradiations at 90°C.

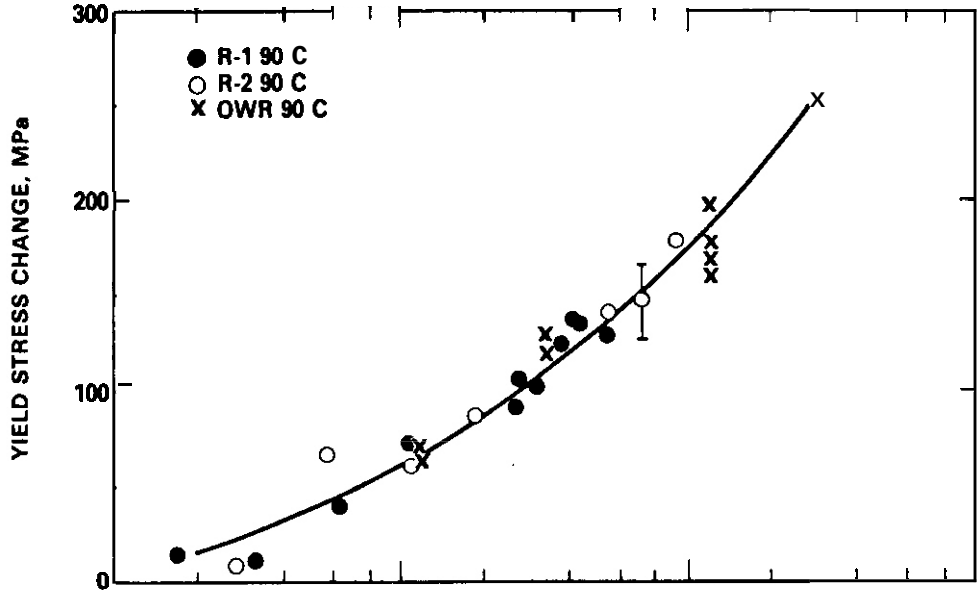

FIGURE 5. Change in Yield Stress of Solution Annealed 316 Stainless Steel as a Function of OPA for RTNS-II and OWR Irradiations at 90°C.

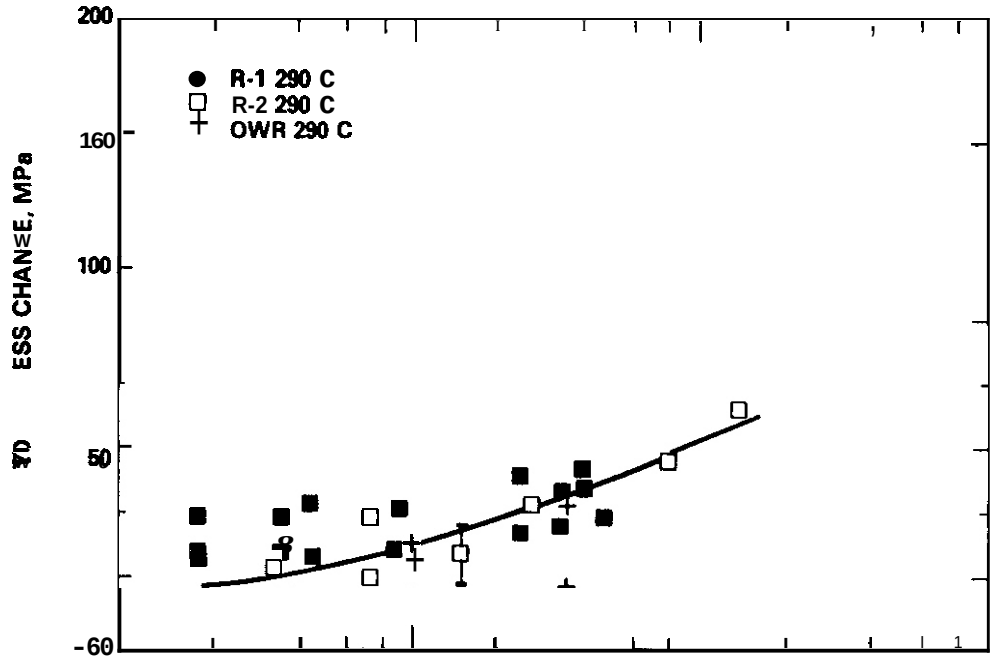

FIGURE 6

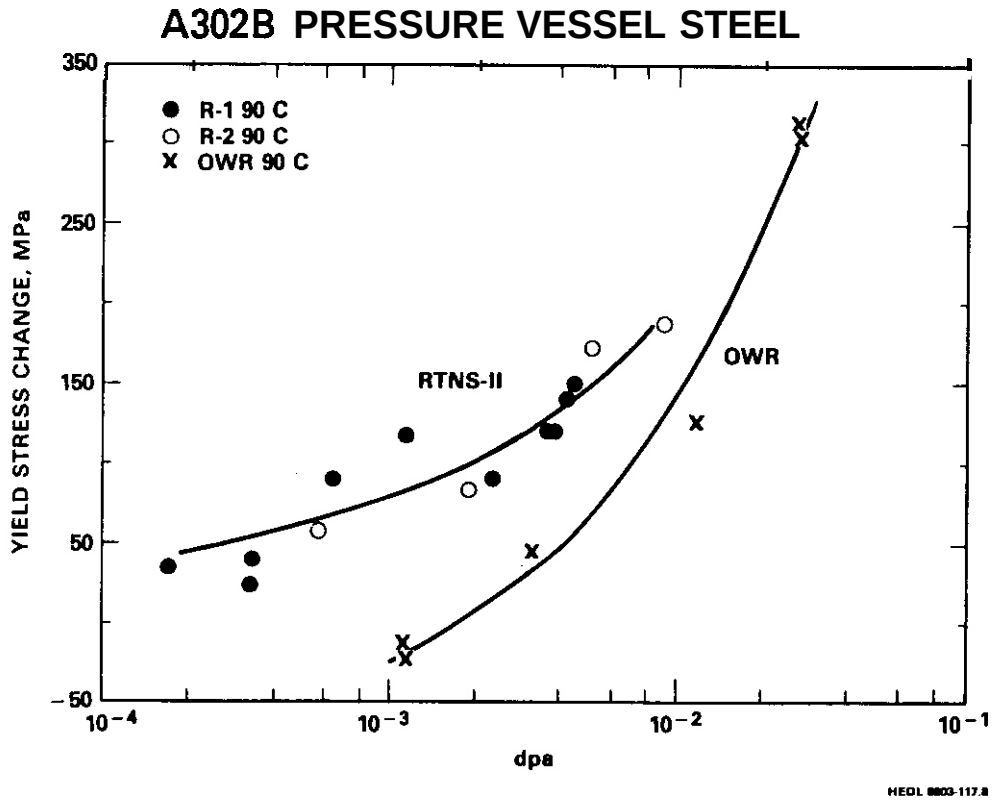

FIGURE 7. Change in Yield Stress of A302B Pressure Vessel Steel as a Function of DPA for RTNS-II and OWR Irradiations at 90°C.

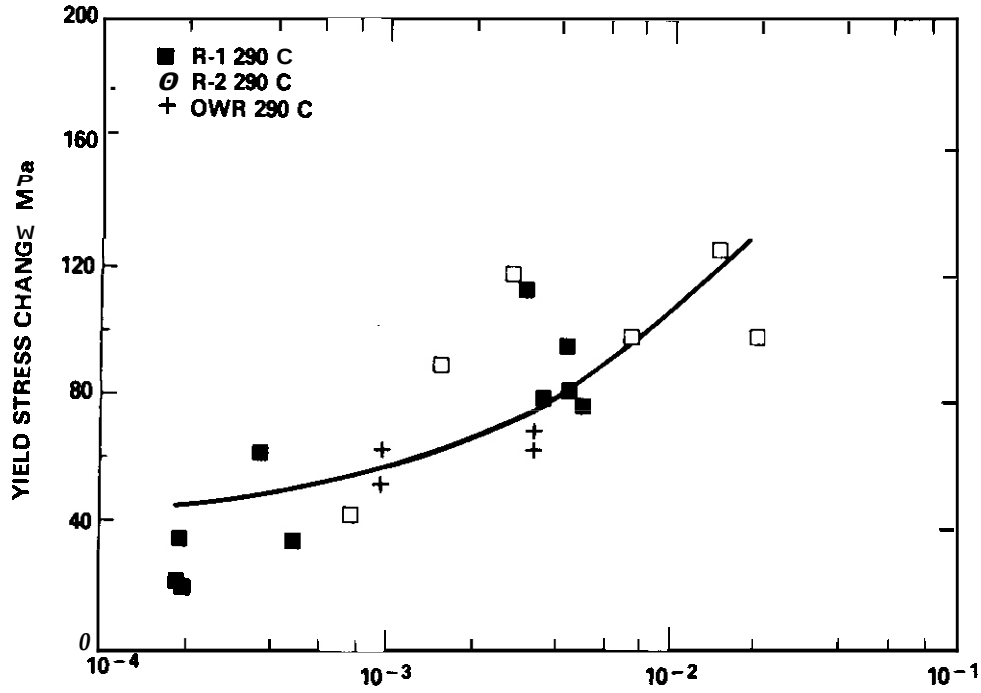

APPLICATIONS OF A COMPOSITE MODEL OF MICROSTRUCTURAL EVOLUTION

R. E. Stoller (Oak Ridge National Laboratory) and G. R. Odette (University of California, Santa Barbara)

1.0 Objective

To develop comprehensive models of microstructural evolution in austenitic stainless steels under fast neutron irradiation and to apply such models to the problem of extrapolating the fission reactor data base to predict swelling under fusion reactor conditions.

2.0 *Summary*

Near-term fusion reactors will have to be designed using radiation effects data from experiments conducted in fast fission reactors. These fast reactors generate atomic displacements at a rate similar to that expected in a DT fusion reactor first wall. However, the transmutant helium production in an austenitic stainless steel first wall will exceed that in fast reactor fuel cladding by about a factor of 30. Hence, the use of the fast reactor data will involve some extrapolation. A major goal of this work is to develop theoretical models of microstructural evolution to aid in this extrapolation.

In the present work a detailed rate-theory-based model of microstructural evolution under fast neutron irradiation has been developed. The prominent new aspect of this model is a treatment of dislocation evolution in which Frank faulted loops nucleate, grow and unfault to provide a source for network dislocations while the dislocation network can be simultaneously annihilated by a climb/glide process. The predictions of this model compare very favorably with the observed dose and temperature dependence of these key microstructural features over a broad range. In addition, this new description of dislocation evolution has been coupled with a previously developed model of cavity evolution and good agreement has been obtained between the predictions of the composite model and fast reactor swelling data. The results from the composite model also reveal that the various components of the irradiation-induced microstructure evolve in a highly coupled manner. The predictions of the composite model are more sensitive to parametric variations than more simple models. Hence, its value as a tool in data analysis and extrapolation is enhanced.

3.0 Program

Title: Radiation Effects Mechanisms
Principal Investigators: L. K. Mansur and R. E. Stoller
Affiliation: Oak Ridge National Laboratory

Title: Damage Analysis and Fundamental Studies for Fusion Reactor Materials Development
Principal Investigators: G. R. Odette and G. E. Lucas
Affiliation: University of California, Santa Barbara

4.0 Relevant OAFS Program Plan Task/Subtask

Subtask II.C.1.2 Effects of Material Parameters on Microstructure — Modeling and Analysis
Subtask II.C.16.1 Composite Correlation Models and Experiments — Correlation Model Development
Subtask II.C.18.3 Relating Low and High Exposure Microstructures — Modeling and Analysis

5.0 Accomplishments and Status

5.1 Introduction

During the last 10 to 15 years, a large amount of radiation effects data has been produced. The focus of much of this experimental effort has been to increase our understanding of void swelling and microstructural

evolution in austenitic stainless steels. Almost all of these experiments have been carried out in fast fission reactors where the damage rate is similar to that which will occur in the first wall of a fusion reactor fueled by deuterium and tritium (DT). Unfortunately, the production of helium by transmutation reactions in an austenitic stainless steel fusion reactor first wall will be about 30 times greater than the value obtained in fast reactor irradiations. This difference is most conveniently expressed as the ratio of transmutant helium to atomic displacements (He/dpa ratio). The He/dpa ratio is about 0.35 appm He/dpa in the Experimental Breeder Reactor-II (ERR-II) and will be about 10 appm He/dpa in a DT fusion reactor first wall. Therefore, the use of this fast reactor data to design near-term fusion reactors will require some extrapolation.

One purpose of the work discussed below is to aid this extrapolation of fast reactor swelling data hy developing theoretical models of microstructural evolution under fast neutron irradiation. These models can be used in the analysis of irradiation experiments to identify key mechanisms and parameters for further study. The use of fast reactor data to calibrate such models also permits them to be used in a predictive fashion. Earlier work has involved the use of more simple cavity evolution models in just this way (1–4). A major limitation of the work just referenced was the neglect of the dose dependence of microstructural features other than the cavities. The present work represents an effort to remove this limitation by generating in a self-consistent manner the time dependence of the major microstructural features observed in irradiated stainless steels; cavities, Frank faulted dislocation loops and network dislocations. The influence of second phase precipitate particles is included to a limited degree as described previously (4). Although the model does not yet include any explicit treatment of microchemical evolution, the specific values of the various rate-theory parameters used to calibrate the model can approximately account for this evolution. The major approximation in this case is that the value of parameters which can be altered by microchemical evolution (e.g. point defect biases and diffusivities) are essentially time-averaged.

5.2 Model Description

Because the details of the model are discussed elsewhere (5,6), only a summary description of the model's features will be given here. The present work is an extension of the cavity evolution models referenced above (1–4). That work helped to establish a generally accepted sequence of events which leads to void formation in irradiated stainless steels. Voids are believed to form as the result of gas-stabilized bubbles reaching a critical size beyond which additional gas is not required for growth. This critical size is determined primarily by the matrix free surface energy, the temperature and the vacancy supersaturation[7-10]. References 4 and 7 describe the aspects of the model which concern cavity evolution in detail.

The familiar rate theory approach (4,11) is used to compute the sink strengths of the various extended defects and the point defect concentrations. The concentration of vacancies and mono-, di-, tri- and tetra-interstitials are computed at quasi-steady-state. Only the mono-defects are considered to be mobile (12). The tetra-interstitial is assumed to be a stable nucleus for Frank faulted loop growth. The model includes the following extended defects: bubbles, voids, transient vacancy clusters in the form of microvoids, subgrain structure, Frank faulted loops and network dislocations. The faulted loops and network dislocations are assigned a bias for interstitials; all other sinks are unbiased.

The consideration of small interstitial clusters modifies the conventional equations for the vacancy and interstitial concentrations by including terms which reflect their loss due to impingement upon such clusters. The equations for the di- and tri-interstitial clusters reflect growth and shrinkage by reactions with the mono-defects (5,6). The equation describing the tetra-interstitial population provides a transition between the discrete cluster regime and the Frank faulted loop regime. This "hybrid" equation describes single atom transitions between the tri- and tetra-interstitial but uses an effective transition time to describe losses to the larger loop population,

$$\frac{dC_4}{dt} = \beta_i^3 C_3 - \beta_v^4 C_4 - C_4 \tau_4^{-1} \qquad (1)$$

The $\beta_{i,v}^j$ terms in Eq. (1) are impingement rates of the mono-defects on the j-th cluster size (5,6). The τ_4 term in Eq. (1) is the lifetime of a tetra-interstitial against growth to the size of the first loop size class, r_1^ℓ. If r_4 is the radius of the tetra-interstitial,

$$\tau_4 = \int_{r_4}^{r_1^\ell} \left(\frac{dr_\ell}{dt}\right)^{-1} dr_\ell \qquad (2)$$

in which dr_ℓ/dt is the loop growth rate. The loop population is described by equations of the form:

$$\frac{dN_i^\ell}{dt} = N_{i-1}^\ell \tau_i^{-1} - N_i^\ell \tau_{i+1}^{-1} \qquad (3)$$

where N_i^{ℓ} is the number of loops in a given size class with radius r_i^{ℓ} and the τ_i are computed with appropriate limits using Eq. (2).

Equation **(1)** has been shown to provide an adequate boundary condition between the two regions in which alternate mathematical descriptions of interstitial loop growth (5,6) are used. The use of the discrete clustering description would require greater than 10^4 equations to describe the loop population. The hybrid description requires about 20.

The model for the evolution of the network dislocations includes four components, two of which are only active under irradiation while the other two are thermally activated. The thermal components are a high temperature climb source term due to Bardeen-Herring sources and an annihilation term due to stress-assisted directional diffusion of vacancies. The development of these components owes much to similar models which have been developed in the study of creep (13,14). The Bardeen-Herring sources for network dislocations are similar to Frank-Read sources except that the latter are glide driven while the former are climb driven **(15).** A simple geometrical argument leads to a network dislocation (ρ_n) generation rate from Bardeen-Herring sources **(5.6):**

$$R_{th}^{\rho_n} = 2\pi v_{cl}^{\sigma} S_D \tag{4}$$

in which v_{cl}^{σ} is the dislocation climb velocity in the presence of a back stress due to pinned dislocations (16,17) and S_D is thermal the source density (5,6). Network dislocations can also be annihilated when segments with opposite Burgers vectors climb together. If the average climb distance to annihilation is d_{cl}, the characteristic time for this process is:

$$\tau_{th} = \frac{d_{cl}}{v_{cl}^{\sigma}} . \tag{5}$$

This climb distance is assumed to be equal to the mean spacing of network dislocations so that $d_{cl} = (\pi\rho_n)^{1/2}$. Under irradiation the unfaulting of Frank loops provides an additional source of network dislocations. The model assumes that the maximum faulted loop size is governed by the geometric constraint that the loop unfaults upon contacting another loop or network dislocation. This leads to an unfaulting radius

$$r_{unf}^{\ell} = (\pi\rho_t)^{-1/2} \tag{6}$$

in agreement with observation **(18).** In Eq. **(6)** ρ is the total dislocation density. The rate at which loops unfault (τ_{unf}^{-1}) is calculated using an equatfon analogous to Eq. *(2).* Finally, bias driven climb under irradiation can also lead to the annihilation of network dislocations. The climb velocity in this case is:

$$v_{cl}^{irr} = \frac{a}{b} [Z_i^n D_i C_i - Z_v^n D_v (C_v - C_v^n)] . \tag{7}$$

The characteristic time for this process is given by analogy with Eq. (5) and the two lifetimes are added using an electrical resistance analog:

$$\tau_T = (\tau_{irr}^{-1} + \tau_{th}^{-1})^{-1} . \tag{8}$$

This leads to the rate equation describing the evolution of the dislocation network as

$$\frac{d\rho_n}{dt} = 2\pi(v_{cl}^{\sigma} S_D + r_{unf}^{\ell} N_{unf}^{\ell} \tau_{unf}^{-1}) - \rho_n \tau_T^{-1} \tag{9}$$

5.3 Model Calibration and Predictions

Such a complex microstructural model includes a number of physical parameters. Unfortunately, values for many of the required parameters are not well known or have only been measured in pure materials. Because of this uncertainty about parameter values, the predictions of even a well calibrated model may not be based on a unique set of parameter values. Other combinations of parameters can give very similar results. One goal of the present work was to try to limit the range of possible parameter choices by including additional physical mechanisms in a well understood, simple model. This has proven to be successful. A full description of the model calibration can be found in References 5 and 6, a couple of examples of this work will be given here. The primary material parameters used are listed in Table 1.

Table 1. Material Parameters

vacancy migration energy, E_v^m	1.4 eV
Vacancy formation energy, E_v^f	1.6 eV
Interstitial migration energy, E_i^m	0.85 eV
Network dislocation/interstitial bias, Z_i^n	1.25
Frank faulted looplinterstitial bias, Z_i^ℓ	1.5
Free surface energy, γ	$3.24 - 1.4 \times 10^{-3}\ T(°C)\ J/m^2$

The thermal dislocation evolution model was first calibrated by predicting the recovery of 20% cold-worked material with the dose rate set to zero. Using reasonable values of model parameters, very good agreement was ohtained with dislocation densities in 20% cold-worked and aged AISI 316 stainless steel (5,6,19,20). The sensitivity of the model predictions to the thermal dislocation evolution model will be discussed below. Then the swelling predictions of the model were calibrated using swelling data from irradiations in the ERR-I1 of several heats of AISI 316 stainless steel which had been developed for the first core of the Fast Flux Test Facility (FFTF) (21,22). These so-called FFTF first core heats were chosen to minimize the effect of heat-to-heat variations. Figure 1 compares the predicted swelling and the first core data at an intermediate and high fluence. The model predicts both similar incubation times (Fig. la) and peak swelling rates. Figure 2 and Fig. 3 compare the predicted network dislocation density and peak Frank faulted loop density with fast reactor data from several sources (18,20,23–27). Here again the agreement is very good.

An example of a new parametric dependence in the model is shown in Fig. 4, a–c. Here the influence of the interstitial migration energy on the swelling, network dislocation density and peak faulted loop density is shown. The curves labeled as the base case use $E_i^m = 0.85$. The results of the simple void swelling theory are not sensitive to this parameter (28) and a much lower value (<0.5 eV) which reflects measurements on pure materials is normally used (1–4,29). However the present model is sensitive to E_i^m via its effect on the loop population. The loop evolution in turn influences the network dislocation density and the predicted swelling. An analysis of Fig. 4, a–c reveals the complex coupling of the evolution of these three microstructural features. The higher interstitial migration energy is also consistent with recent measurements of this parameter in austenitic stainless steels (30,31).

Ouring the calibration, the model was also used to compare alternate descriptions of the faulted loop/interstitial bias, Z_i^ℓ. If interstitial absorption at faulted loops is diffusion limited, a size dependent bias is obtained (32) while if the absorption is reaction rate limited a constant loop bias would result. The temperature dependence of the predicted faulted loop density at 50 and 100 dpa and the peak loop density are shown in Fig. 5. The size dependent used bias was that of Wolfer and Ashkin (32). The maximum value of $Z_i^\ell(r_\ell)$ was 3.5 for the smallest loops and it asymptotically approached the network dislocation/interstitial bias at large sizes. The results for a constant loop bias in Fig. 5 reflect the base case value of 1.50. The predictions using the size dependent bias are clearly too high at the higher temperatures (cf. Fig. 3). This result is in agreement with an analysis of loop growth during electron irradiation performed by Yoo and Stiegler (33).

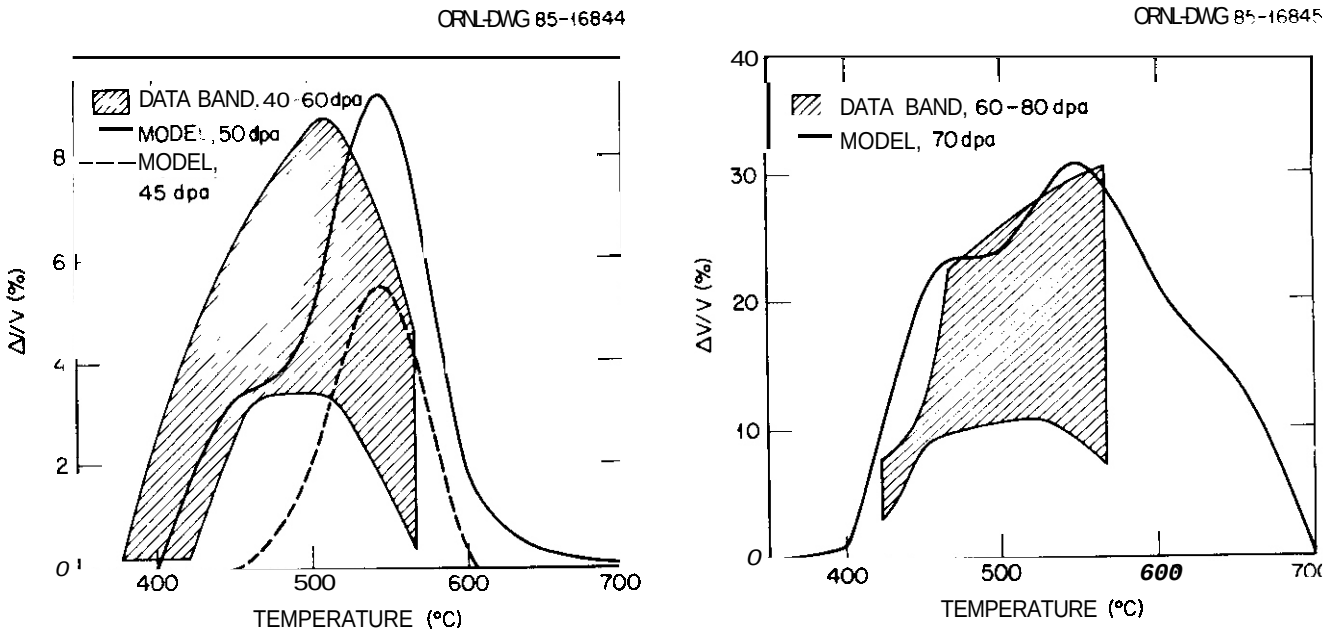

Fig. 1. Comparison of model predictions and fast reactor swelling data (21.22).

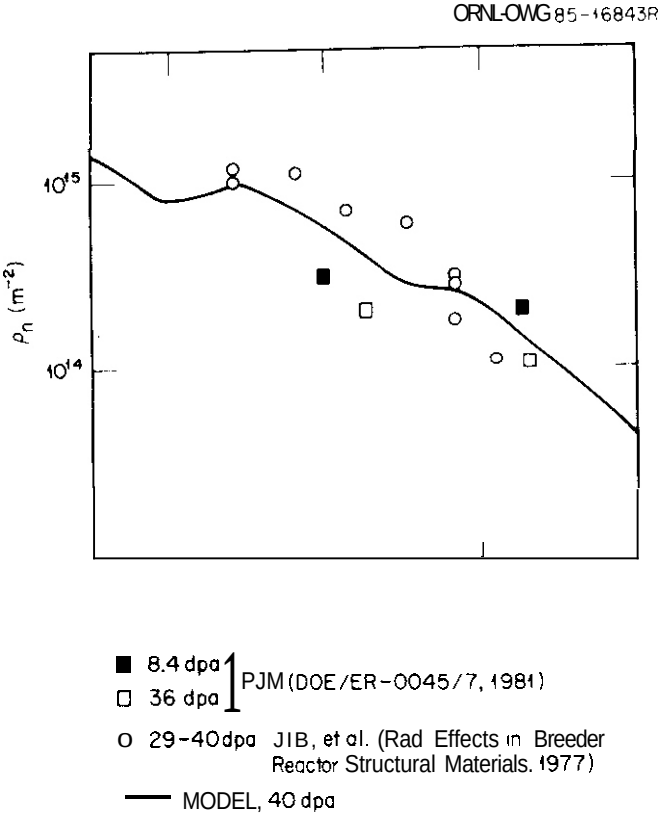

Fig. 2. Comparison of model predictions and network dislocation density measurements (20,23).

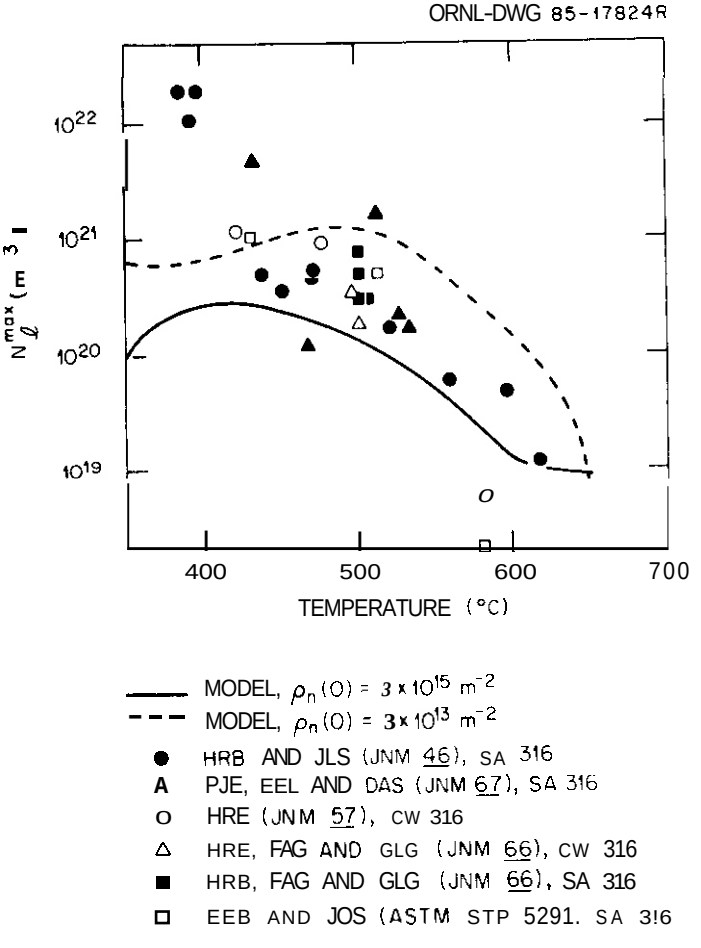

Fig. 3. Comparison of model predictions of peak faulted loop density and fast reactor data (18,24–27).

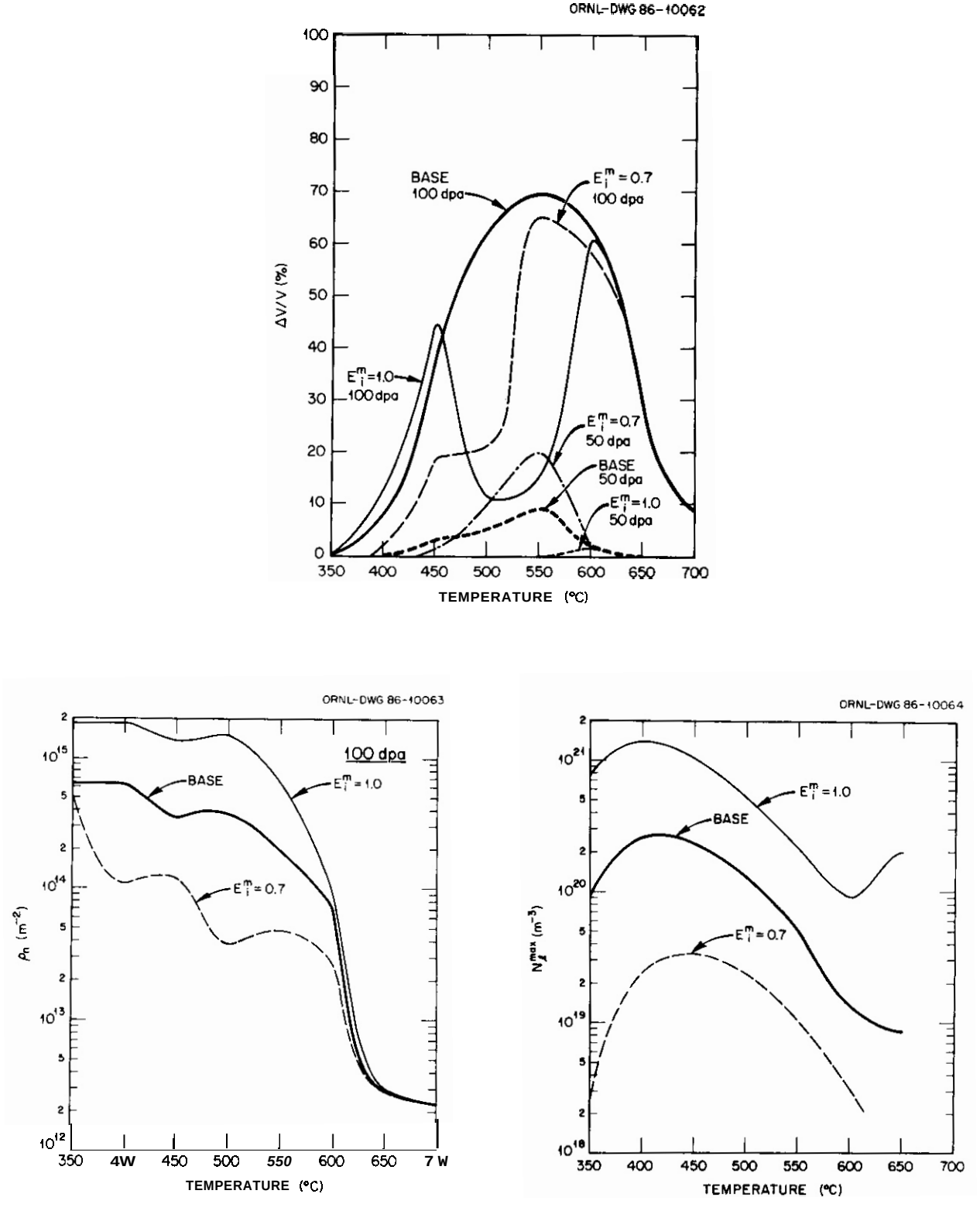

Fig. 4. Influence of interstitial migration energy (Em) on model predictions. Base case is from fast reactor calibration, $E_i^m = 0.85$.

Although the thermal dislocation evolution model was calibrated independently, the predictions of the comprehensive model for fast neutron irradiation are sensitive to the thermal dislocation model parameters. This sensitivity is shown in Fig. 6 where the thermal source density, S_D, has been varied from the nominal value which was determined during calibration (5.6). For temperatures greater than 550°C the curves labeled "Low S_D" and High S_D" in Fig. 6 were calculated with a 10% decrease and increase in this parameter. For 550°C and below the value was varied by a factor of 10. At the lower temperatures the results are insensitive to this variation. This is the temperature regime in which little thermal recovery occurs. However at about 575–625°C the predictions are quite sensitive to S_D. This is a temperature range in which the microstructure of the material begins to recover in the absence of irradiation. This occurs largely due to increased thermal vacancy diffusion. Under irradiation the vacancy supersaturation decreases in this temperature range for the same reason. Hence the behavior of the material under irradiation begins to appear more like the thermal behavior and the sensitivity of the model predictions in this transition regime is not surprising. The temperature range over which this transition occurs is known to he dependent on alloy composition *(20)*. Therefore the predictions of the present model at the higher temperatures reflect the specific heat (DO) which was used to calibrate the thermal dislocation evolution model. The sensitivity of the predicted swelling in Fig. 6 to the network dislocation density may explain in part the observations that swelling is fairly heterogeneous in cold-worked materials.

5.4 Model Extrapolation to Fusion Conditions

The calibrated model has been used to predict swelling in a DT fusion reactor first wall. The predictions were made for an increased He/dpa ratio of 10 appm He/dpa. The most systematically observed trend in the literature on helium effects is that higher He/dpa ratios promote cavity formation (34,35). The effect can he approximately described by a simple power dependence of the cavity density, N_c, on the He/dpa ratio

$$N_c \alpha (\text{He/dpa})^p \quad , \tag{10}$$

where p is typically in the range of 0.5–1 (34). Here we have scaled the initial bubble densities up from the fast reactor values using Eq. (10) with values of p reflecting weak ($p = 0.2$) to fairly strong ($p = 0.8$) dependence on the He/dpa ratio.

Figure 7 shows the predicted swelling and network dislocation density for an intermediate value of p. p = 0.5. The general trends include a reduced incubation time at all temperatures and enhanced swelling at both low and high temperatures at high doses for the fusion case. At intermediate temperatures and high doses the predicted swelling for fusion is less than the fast reactor value due to a reduced swelling rate. The dislocation density is generally somewhat lower than for the fusion He/dpa ratio. There is some support for this prediction in the reported dislocation densities for one heat of AISI 316 stainless steel which has been irradiated in both the EBR-II (~0.35 appm He/dpa) and the High Flux Isotope Reactor (~70 appm He/dpa) (36). The explicit dependence of swelling on cavity density is shown in Fig. 8. The details of the behavior are complex due to the interactions between the various defect types hut the trends observed in Fig. 6 are maintained.

The reduced incubation times and enhanced low temperature swelling have potentially significant implications for fusion reactor designs. Only a very limited amount of dimensional instability can be accommodated in typical reactor designs (37,38) hence the incubation time is perhaps a parameter of more engineering significance than the peak swelling rate. Further, recent conceptual designs using austenitic stainless steels have tended to move toward lower operating temperatures (37.38).

5.5 Summary

The use of a comprehensive rate-theory model of microstructural evolution under fast neutron irradiation has been described. The new features of this model include an explicit treatment of the dose dependence of both Frank faulted loops and network dislocations. The more complex model has been shown to provide a powerful analytical tool for data analysis and the evaluation of various theoretical concepts, e.g. the comparison of rate limited and diffusion limited point defect absorbtion at Frank faulted loops given above. Because the model includes additional physical mechanisms, it is more sensitive to arbitrary parameter changes. The dependence of the model predictions on the interstitial migration energy is one example of this sensitivity. This "stiffness" is believed to be physically meaningful.

The new model was calibrated using a well defined set of fast reactor swelling data. The calibrated model was then used to predict swelling in an austenitic stainless steel fusion reactor first wall. The predictions indicate that fast reactor swelling data may not provide an adequate representation of swelling in a fusion reactor. Specifically, low temperature swelling is enhanced and incubation times are reduced at all relevant temperatures for fusion reactor conditions. These results highlight the need for additional theoretical and experimental work to improve our understanding of helium effects in a fast neutron irradiation environment. A recently proposed set of experiments involving the use of isotopically tailored alloys to obtain a range of He/dpa ratios in a single reactor should be particularly useful (39,40).

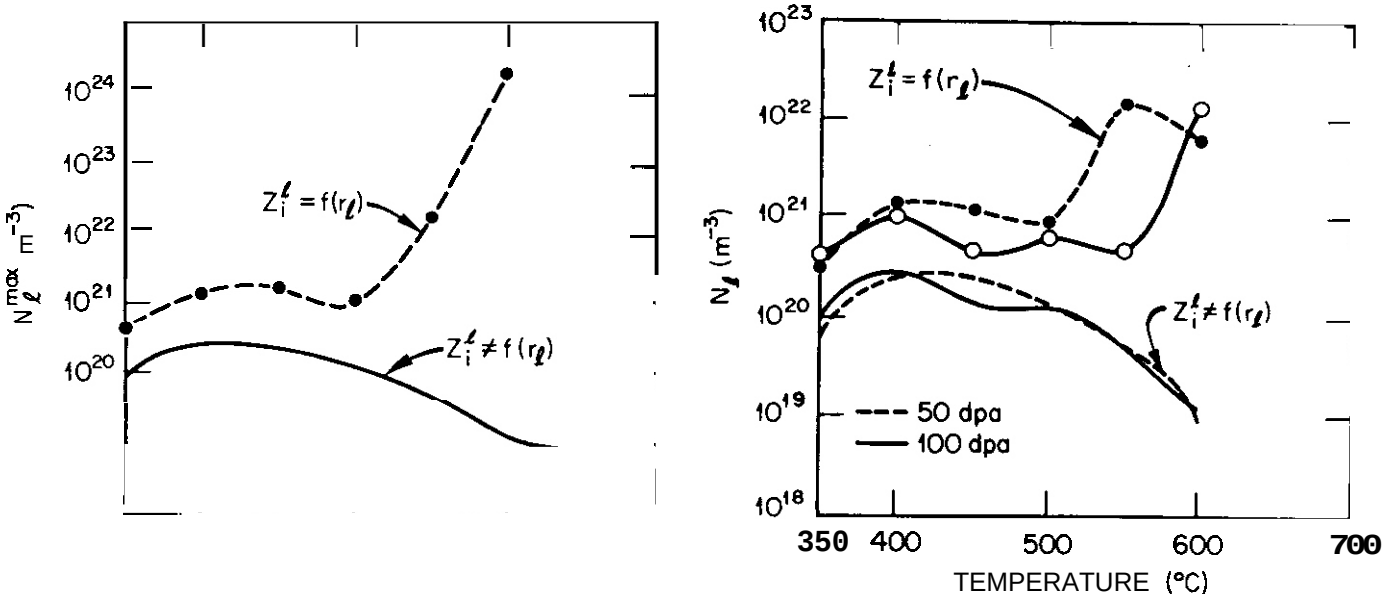

Fig. 5. Comparison of model predictions of faulted loop density using constant faulted loop/interstitial bias (Z_i^ℓ = 1.5) and a size dependent bias (32).

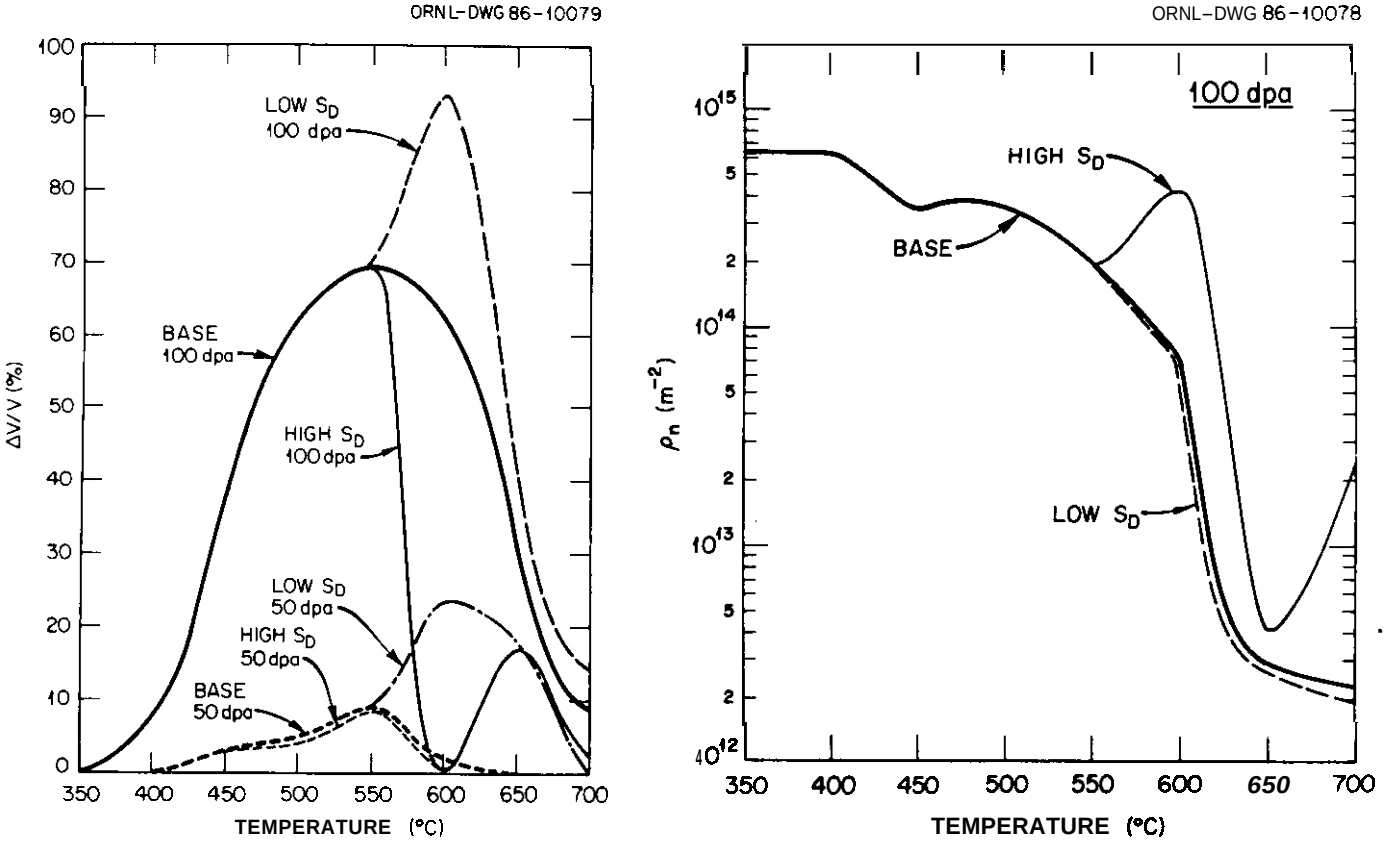

Fig. 6. Influence of thermal source density (S_D) on the predicted swelling and network dislocation density.

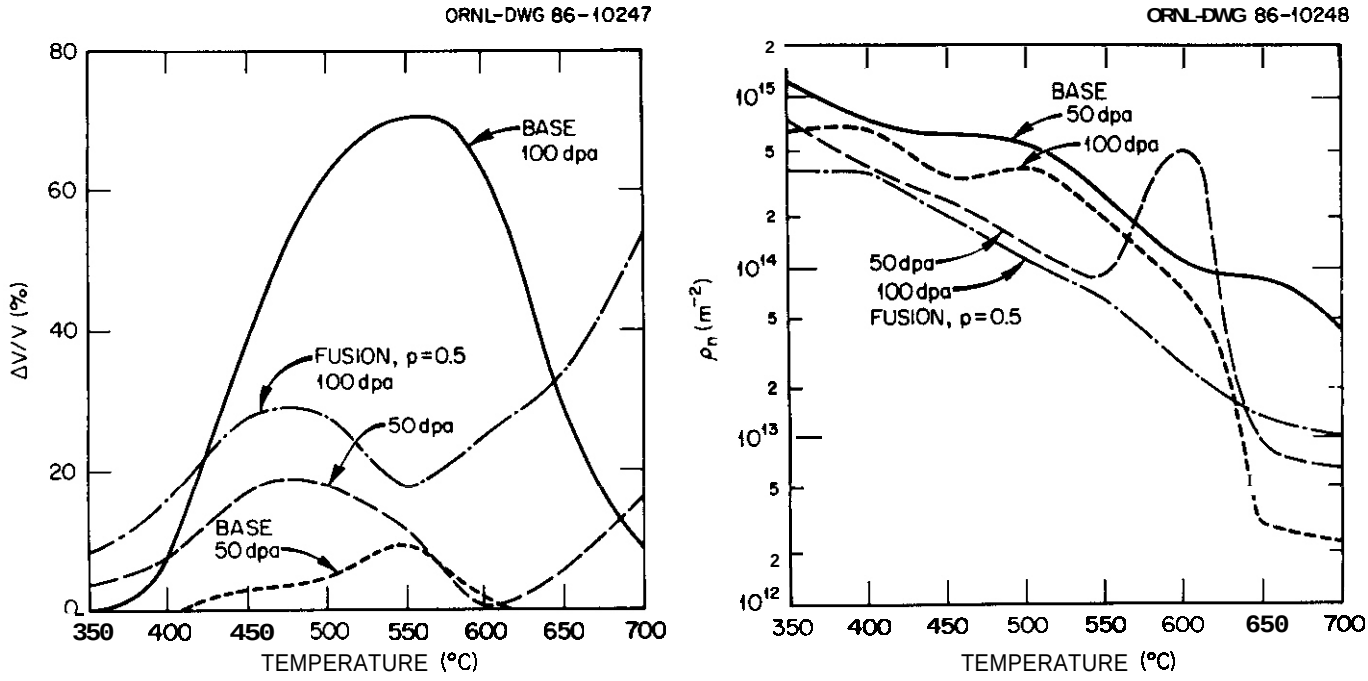

Fig. 7. Model predictions of swelling and network dislocation density for fusion at 50 and 100 dpa. Base case is from fast reactor calibration. p = 0.5.

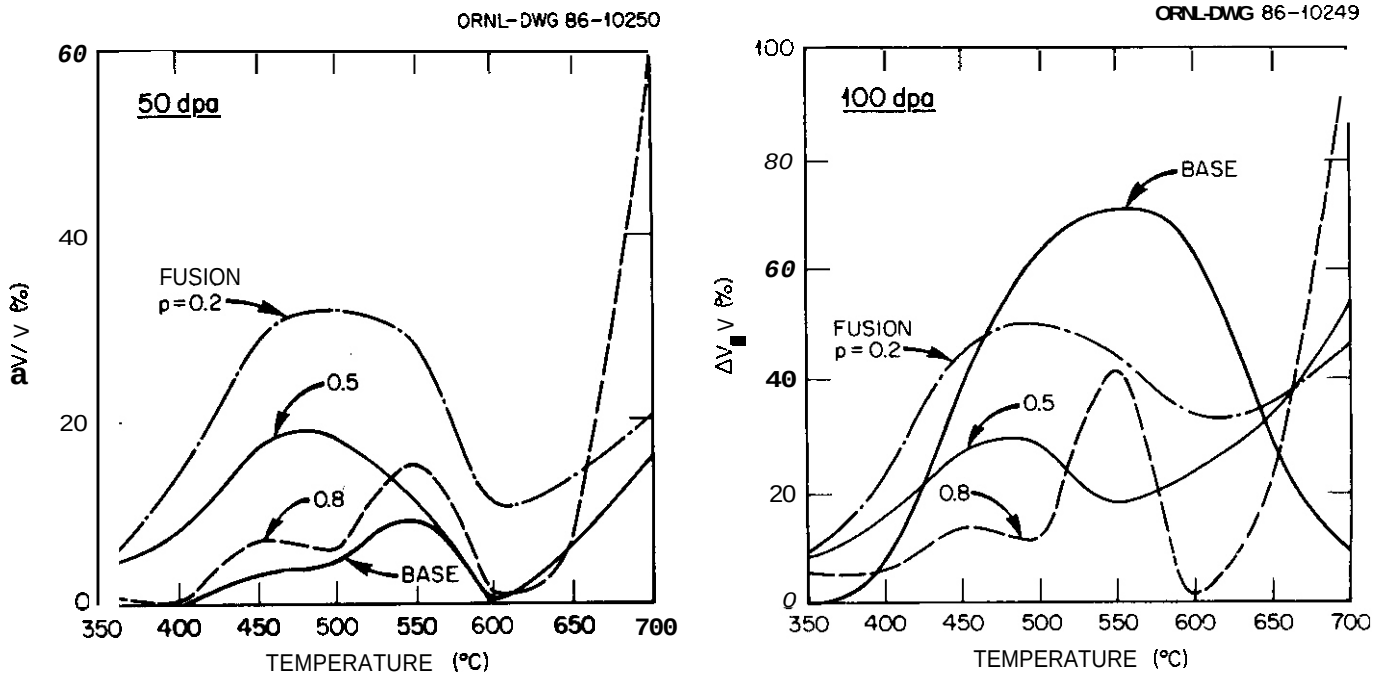

Fig. 8. Cavity density influence on model predictions for fusion. Base case is from fast reactor calibration.

6.0 References

1. G. R. Odette and S. C. Langley, Radiation Effects and Tritium Technology for Fusion Reactors, CONF-750989, 1975. I: 395–416.

2. R. E. Stoller and G. R. Odette, J. Nucl. Mater. 103–104 (1981) 1361–1365.

3. G. R. Odette and R. E. Stoller, J. Nucl. Mater. 122–123 (1984) 514-519.

4. R. E. Stoller and G. R. Odette, "The Effect of Helium on Swelling in Stainless Steel: Influence of Cavity Density and Morphology," Effects of Radiation on Materials: Eleventh Int. Symp., ASTM STP 782, ASTM, 1982, 275–294.

5. R. E. Stoller and G. R. Odette, "A Composite Model of Microstructural Evolution in Austenitic Stainless Steel Under Fast Neutron Irradiation," Effects of Radiation on Materials: Thirteen Int. Symp., Chicago, III., June 23–25, 1986, to be published by the American Society for Testing and Materials.

6. R. E. Stoller and G. R. Odette, Damage Analysis and Fundamental Studies, Quarterly Progress Report, DOE/ER-0046/23, November, 1985, 34–48.

7. R. E. Stoller and G. R. Odette, J. Nucl. Mater. 131 (1985) 118–125.

8. L. K. Mansur and U. A. Coghlan, J. Nucl. Mater. 119 (1983) 1-25.

9. M. R. Hayns, The Transition From Gas Bubble to Void Growth. AERE-R8806, U.K.A.E.A., 1977.

10. K. C. Russell, Acta Met. 26 (1978) 1615–1630.

11. A. D. Brailsford and R. Rullough. The Theory of Sink Strengths, AERE Harwell Report TP.854, 1980.

12. R. A. Johnson, J. Nucl. Mater. 83 (1979) 147–159.

13. F. R. N. Nabarro. Phil. Mag. 16 (1967) 231–237.

14. J. Gittus, Creep, Viscoelasticity and Creep Fracture in Solids, John Wiley and Sons, New York. 1975.

15. J. Bardeen and C. Herring, Imperfections in Nearly Perfect Crystals, W. Schockley (Ed.), John Wiley and Sons, New York, 1952.

16. W. D. Nix, R. Gasca-Neri, and J. P. Hirth, Phil. Mag. 23 (1971) 1339–1349.

17. G. B. Gibbs, Phil. Mag. 23 (1971) 771–780.

18. H. R. Brager, F. A. Garner, and G. L. Guthrie, J. Nucl. Mater. 66 (1977) 181–197.

19. D. Fahr, E. E. Bloom, and J. O. Stiegler, "Irradiation Embrittlement and Creep in Fuel Cladding and Core Components," Proc. of BNES Conf., London, 1972, 167–177.

20. P. J. Maziasz, Alloy Development for Irradiation Performance, Quarterly Progress Report, DOE/ER-0045/7, September, 1981, 54–97.

21. J. F. Bates and M. K. Korenko, Nucl. Tech. 48 (1980) 303–314.

22. F. A. Garner, "Overview of the Swelling Behavior of 316 Stainless Steel." Optimizing Materials for Nuclear Applications, Symp. Proc.. TMS AIME. New York, 1985.

23. J. I. Bramman, C. Brown, J. S. Watkin. C. Cawthorne. E J. Fulton, P. J. Barton, and E. A. Little, "Void Swelling and Microstructural Changes in Fuel Pin Cladding and Unstressed Specimens Irradiated in DFR," Radiation Effects in Breeder Reactor Structural Materials. Int. Conf. TMS AIME, New York, 1977, 479–507.

24. E. E. Bloom and J. O. Stiegler. Effects of Irradiation on Substructure and Mechanical Properties of Metals and Alloys, ASTM STP 529, ASM, 1973, 360–382.

25. H. R. Rrager and J. L. Straalsund, J. Nucl. Mater. 46 (1973) 124–158.

26. P. J. Barton, B. L. Eyre, and D. A. Stow, J. Nucl. Mater. 67 (1977) 181–197.

27. H. R. Rrager, J. Nucl. Mater. 57 (1975) 103–118.

28. L. K. Mansur, J. Nucl. Mater. 83 (1979) 109–127.

29. F. W. Young, J. Nucl. Mater. 69&70 (1978) 310–370.

30. O. Dimitrov and C. Dimitrov. J. Nucl. Mater. 105 (1982) 3947.

31. J. T. Stanley and J. R. Cost, J. Phys. F: Met. Phys. 14 (1984) 1801–1810.

32. W. G. Wolfer and M. Ashkin, J. Appl. Phys. 46 (1975) 547–557 and erratum.

33. M. H. Yoo and J. O. Stiegler, Phil. Mag. 36 (1977) 1305–1315.

34. G. R. Odette, P. J. Maziasz and J. A. Spitznagel, J. Nucl. Mater. 103&104 (1981) 1289–1304.

35. K. Farrell, P. J. Maziasz, E. H. Lee and L. K. Mansur, Rad. Eff. 78 (1983) 277–295.

36. P. J. Maziasz. ORNL-6121, Oak Ridge National Laboratory, 1985.

37. R. F. Mattas, F. A. Garner, M. L. Grossheck, P. J. Maziasz, G. R. Odette, and R. E. Stoller, J. Nucl. Mater. 122&123 (1984) 230–235.

38. M. A. Abdow, et al., Blanket Comparison and Selection Study, ANL/FPP-83-1, Argonne National Laboratory, 1983.

39. L. K. Mansur, A. F. Rowcliffe, M. L. Grossbeck, and R. E. Stoller, Damage Analysis and Fundamental Studies Quarterly Progress Report, DOE/ER-0046/22, August, 1985, 13-23.

4c. G. R. Odette, Oamage Analysis and Fundamental Studies Quarterly Progress Report, DOE/ER-0046/21, May, 1985, 23–33.

7.0 Publications

"Microstructural Evolution in an Austenitic Stainless Steel Fusion Reactor First Wall," R. E. Stoller and G. R. Odette, presented at the Second International Conference on Fusion Reactor Materials, Chicago, Illinois, April 13–17, 1986, to he published in the Journal of Nuclear Materials.

ION-INDUCE0 SPINODAL-LIKE COMPOSITIONAL MICRO-OSCILLATIONS IN Fe-35Ni AND ITS CONSEQUENCES ON PHASE STABILITY

R. A. Dodd (University of Wisconsin-Madison) and
F. A. Garner (Hanford Engineering Development Laboratory)

1.0 Objective

The object of this effort is to determine the origin and consequences of the radiation-induced micro-oscillations in composition observed in Fe-Ni-Cr alloys in the Invar regime.

2.0 Sumnary

When Fe-35Ni is irradiated with 5 MeV Ni+ nickel ions at 625, 675 or 725°C spinodal-like micro-oscillations in composition develop similar to those observed in Fe-35Ni-7Cr earlier at 675°C. Upon cooling down from the irradiation temperature, however, the low nickel areas (< 28%) of Fe-35Ni transform to a cellular form of martensite. This transformation allows the visualization— of the spacing and relationship of the low nickel areas.

3.0 Program

Title: Irradiation Effects Analysis
Principal Investigator: D. G. Doran
Affiliation: Hanford Engineering Development Laboratory

4.0 Relevant DAFS Program Plan Task/Subtask

Subtask II.C.l. Effect of Material Parameters on Microstructure

5.0 Accomplishments and Status

5.1 Introduction

In earlier reports it was shown that Fe-Ni-Cr alloys in the Invar compositional regime decompose in a spinodal-like manner at temperatures in the 450 to 675°C ranqe when irradiated with either neutrons or ions.[1-5] The nature of these oscillations can be assessed in terms of their impact on mechanical properties or by the use of EOX micro-analysis but heretofore they could not be observed directly since Fe, Cr and Ni are indistinguishable using conventional election diffraction or absorption contrast.

One insight gained from the earlier studies is that chromium appears to participate in the decomposition process as if it were only a surrogate for iron. Not only were its profiles similar to that of iron but there was no impact of chromium on the radiation-induced changes in yield strength. It was also shown that the micro-oscillations developed in ion-irradiated Fe-Ni alloys (Fe-35Ni and Fe-45Ni) in the absence of chromium.[2] In this report the results of the continued study of Fe-35Ni after Ni+ ion irradiation to 117 dpa at 625°C, 675°C and 725°C are presented.

5.2 Results

Since the compositional oscillations are effectively invisible in Fe-Cr-Ni specimens, one must determine their properties by blindly probing the composition along linear traces. A two dimensional matrix of such a probe is shown in Reference 5 for neutron-irradiated Fe-35.5Ni-7.5Cr. The random-direction linear traces used in earlier studies[1-4] showed that there is an irregularity in the profiles that suggests a not-completely periodic nature of the oscillations.

Figures 1 and 2 show that the oscillations can be either quite pronounced or not quite so pronounced about a given reference point, depending on both the starting point and the crystalline vector traversed. Note in Figure 1 that the maximum and minimum nickel concentrations observed are that of FeNi and Fe_3Ni, the same limits observed in neutron-irradiated specimens.[1] Once again, there appears to be an irregular structure in the compositional profile superimposed on the somewhat regular major oscillations. The reason for this irregularity became apparent in the Fe-35Ni specimen in a way that does not occur in Fe-45Ni or various Fe-Ni-Cr alloys. Figure 3 contains a micrograph which shows that relatively irregular martensitic regions have formed in a cellular fashion. There is a large amount of internal strain in these regions as illustrated in Figure 4, showing extensive twinning within the martensite. The lower portion of Figure 3 also shows almost out-of-contrast dislocation tangles within the martensite in another grain which does not place the martensite in a strongly diffracting condition. In each of the martensitic regions the composition was found to be less than 29% nickel. In every case checked, the low nickel areas were found to have transformed. The mean size of these regions is ~200 nm. The foil thickness ranges from 100 to 150 nm in Figures 3 and 4.

A survey of other ion-irradiated specimens (Fe-45Ni and Fe-7Cr-XNi, Fe-15Cr-XNi where x = 30, 35, 45) showed no evidence of martensite formation. However, the Fe-35Ni specimens irradiated at 675 and 725°C were also found to have developed cellular martensite, but the size and mean spacings of the martensitic regions increased with temperature.

Figure 3 also demonstrates in another way the effect of composition on the martensitic transformation. The grain boundary shown in Figure 3 has has been subjected to substantial segregation of nickel. This leads to a zone of ~0.8 μm on each side of the boundary which is free of martensite. Figure 5 shows that at another grain boundary the nickel concentration in the denuded zone is higher than the average of the bulk (35%) and also shows some indication of compositional variations parallel to the boundary. These variations become more pronounced as the distance from the boundary increases.

5.3 Discussion

As one raises either the chromium or nickel content of Fe-Cr-Ni alloys the martensitic start temperature (M_S) is depressed. For unirradiated chromium-free Fe-35Ni and Fe-45Ni Ms is below room temperature and the transformation should not occur. While Fe-45Ni does not decompose sufficiently during irradiation to place small volumes below M_S at room temperature, Fe-35Ni decomposes enough such that substantial microvolumes of material have an Ms above room temperature. When the experiment is terminated and cooling occurs the transformation then takes place.

This transformation may or may not be complete in these micrographs but it preserves in the microstructure a visible record of the micro-oscillations in composition. It also demonstrates the origin of both the local irregularity as well as the relatively periodic nature of the fluctuations.

Several ideas are suggested by this finding. First, even though chromium-bearing alloys have M_S temperatures below that of room temperature, it does not mean that such a transformation cannot be induced to study spatial relationships in the composition profiles. Plans are now being laid to cool Fe-Cr-Ni specimens using dry ice or various liquid gases. This will be done when all other examinations have been completed. Second, it may be possible to visualize the high nickel (45-55%) regions as well. Note in Figure 6 that low temperature irradiations with neutrons (and possibly electrons in an HVEM for our purposes) can be used to cause ordered FeNi to form. This will occur first in those regions with ~50% nickel. This phase can also be imaged using diffraction contrast. The possibility of HVEM irradiations of neutron-irradiated specimens at Argonne National Laboratory is now being explored. Finally, a similar process should occur in neutron-irradiated Fe-35Ni. Two specimens, one irradiated at 520°C to 14 dpa and another irradiated at 600°C to 14 dpa are available.[5] These specimen developed density increases of ~0.5%, indicating that decomposition has occurred but has not yet reached the maximum level observed earlier,[1,2] where density increases of ~1.0 percent are obtained. These specimens are now being prepared for examination.

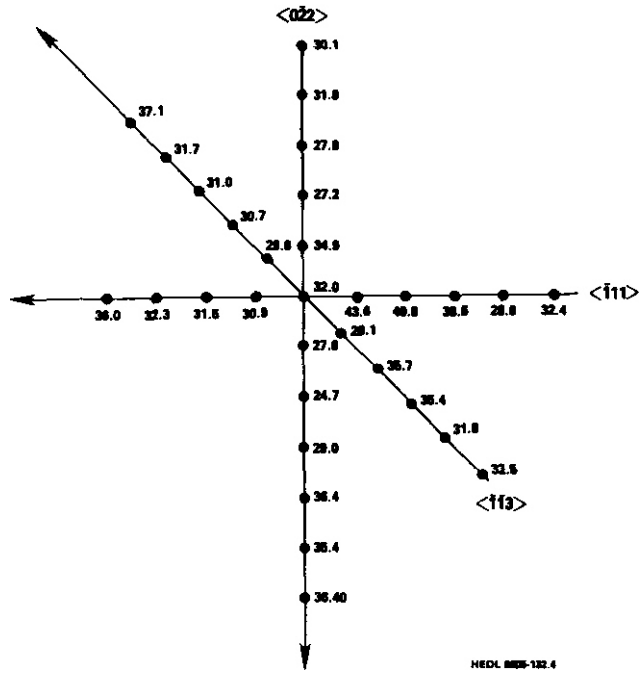

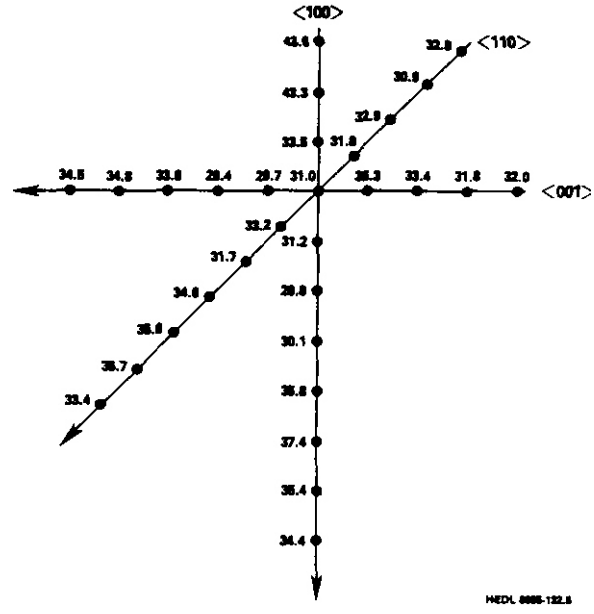

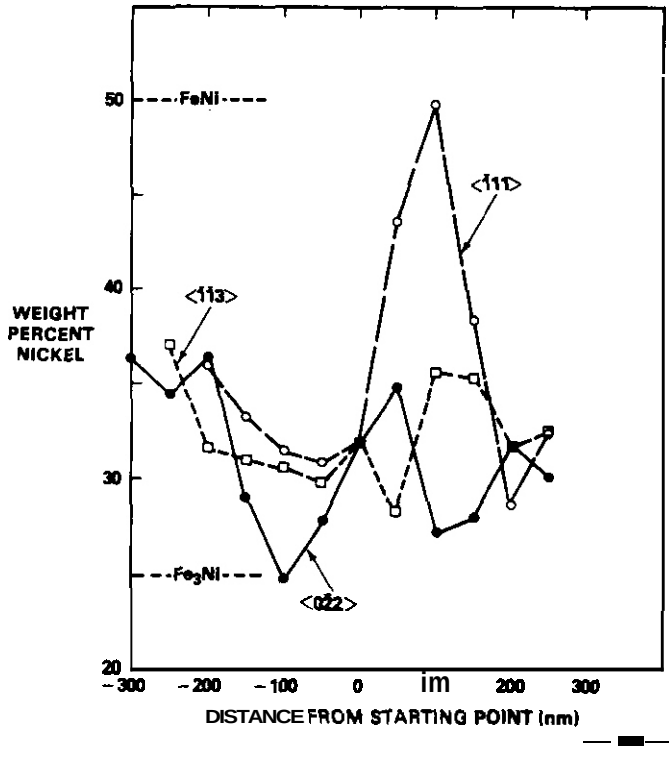

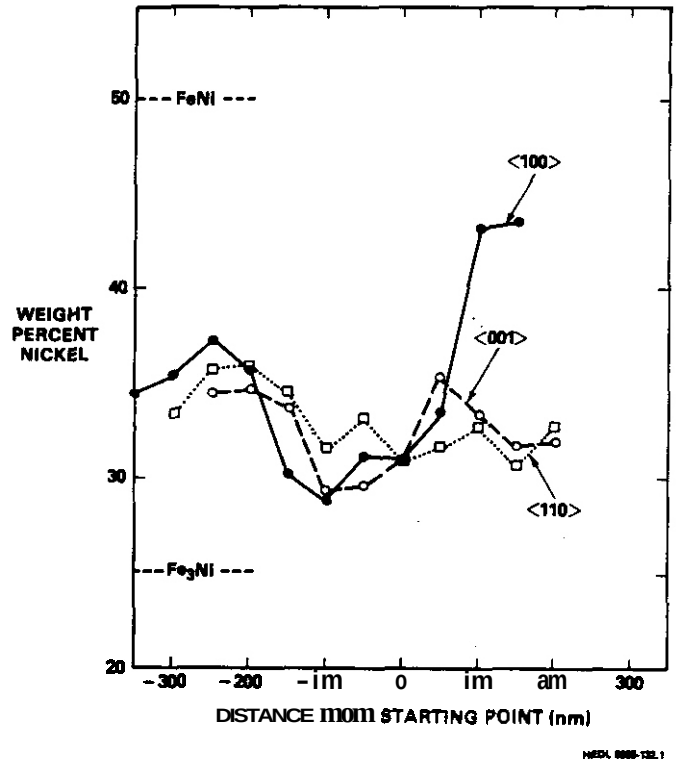

FIGURE 1. Compositional traces alona defined crystallographic directions in Fe-35Ni after Ni^+ irradiation to 117 dpa at 625°C.

FIGURE 2. Another example of compositional traces generated in'the ion-irradiated Fe-35Ni specimens shown in Figure 1.

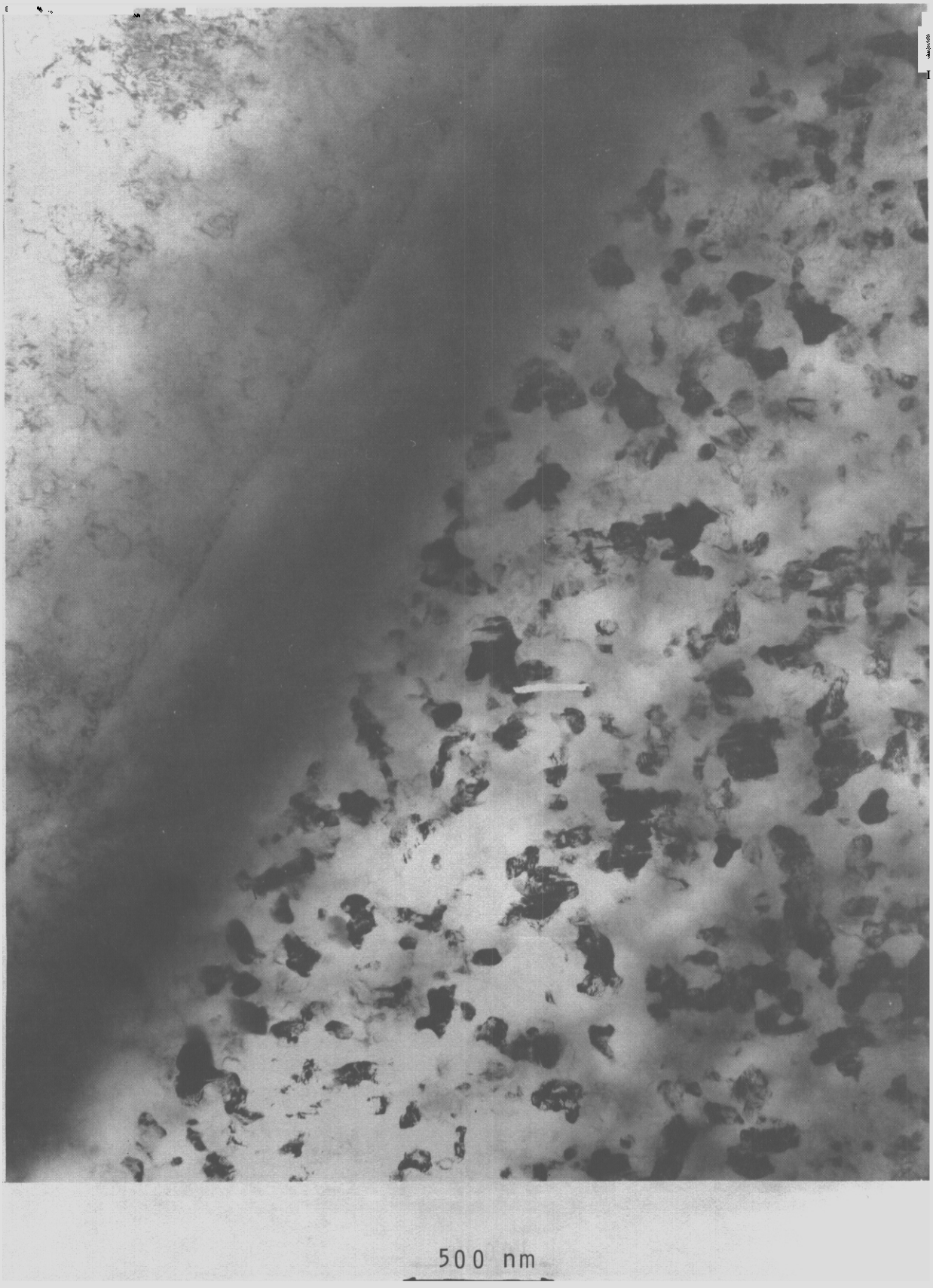

FIGURE 3. Micrograph showing formation of cellular martensite in Fe-35Ni after irradiation at 625°C. Note denuding of martensite along grain boundary where nickel segregates.

FIGURE **4.** **High magnification micrograph** of **cellular martensite region.**

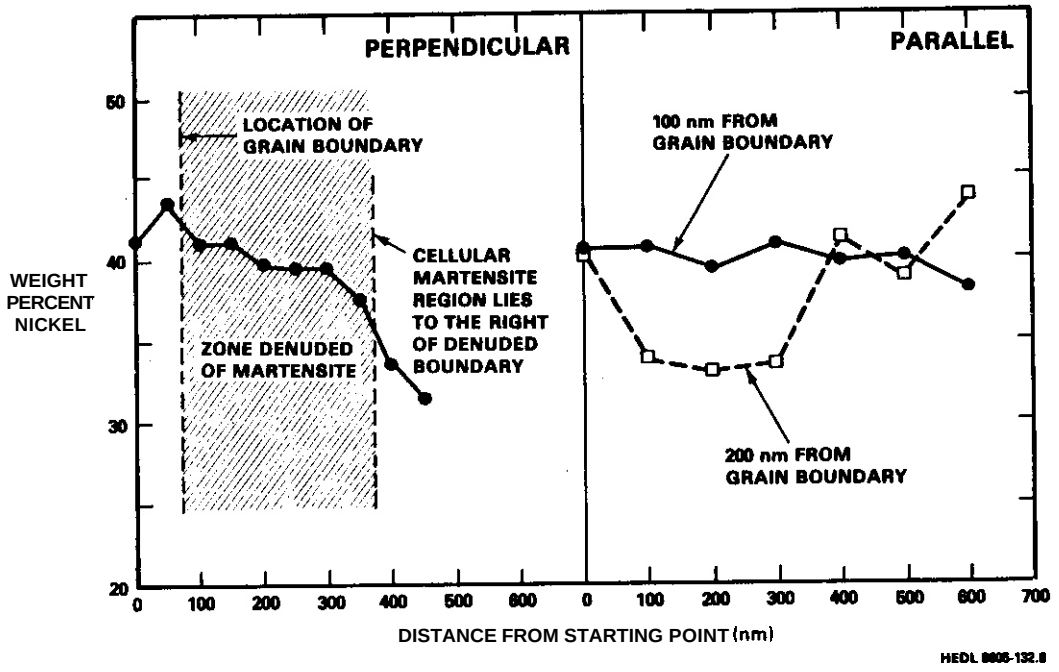

FIGURE 5. Compositional trace across the denuded zone, and two traces parallel to the grain boundary. The grain boundary studied here is different from that shown in Figure 3.

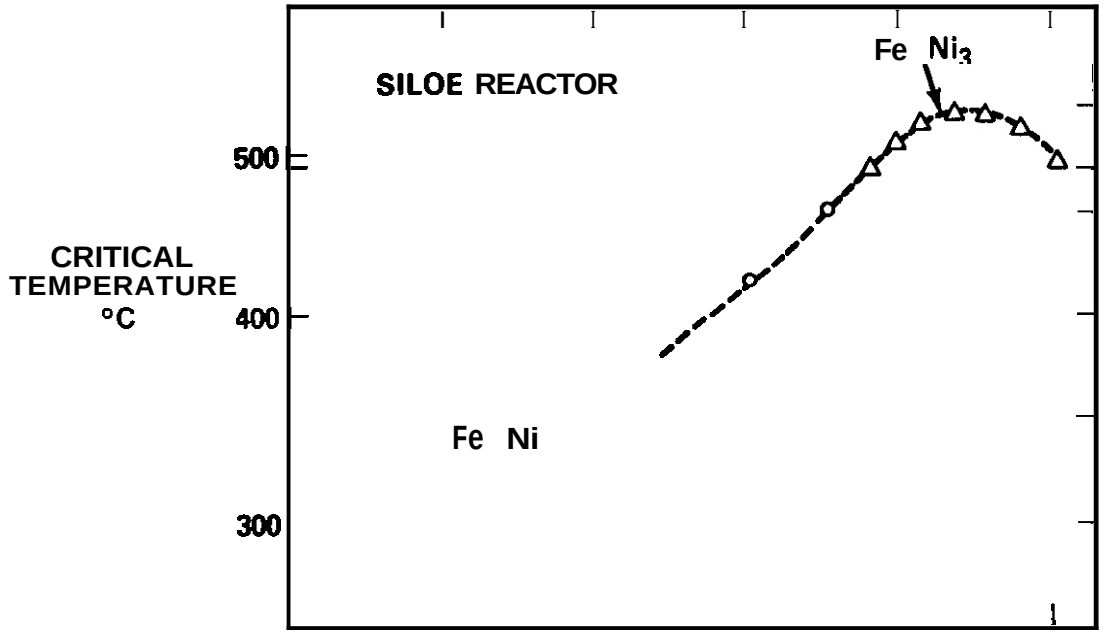

FIGURE 6. Critical temperatures for the order-disorder transformation of NiFe and Ni_3Fe in the Fe-XNi alloy system.(6)

5.4 Conclusions

Radiation-induced spinodal-like oscillations in composition in Fe-35Ni lead to the formation of cellular martensite in low nickel regions during cooling to room temperature. Examination of the spatial relationships of the transformed martensite allows us to visualize the size, spacing and nature of the compositional oscillations that develop during irradiation.

6.0 References

1. H. R. Brager and F. A. Garner in Optimizing Materials for Nuclear Applications, F. A. Garner, D. S. Gelles and F. W. Wiffen (Eds.); TMS-AIME, Warrendale, PA (1985) PP. 141-166.

2 F. A. Garner, H. R. Erager, R. A. Dodd and T. Lauritzen, Nuclear Instruments and Methods in Physics Research, to be published, also HEDL-SA-3280.

3. F. A. Garner, J. Nucl. Mater., 133/134 (1985) 113.

4. H. R. Erager, F. A. Garner, and M. L. Hamilton, J. Nucl. Mater., 1331134 (1985) 594.

5. F. A. Garner and H. R. Erager, OAFS Quarterly Progress Report DOE/ER-0046/24, February 1986, pp. 71-76.

6. J. Pauleve, A. Chamberod, K. Krebs and A. Marchand, "Transformations ordre-desorde et proprietes magnetiques des alliages fer-nickel," IEEE Transactions Magnetics, MAG-2, (3) (1966)pp. 475-478.

7.0 Future Work

Both ion and neutron-irradiated Fe-Cr-Ni and Fe-Ni soecimens will continue to be examined.

8.0 Publications

None.

STABILITY DURING THERMAL ANNEALING OF MICRO-OSCILLATIONS DEVELOPED IN Fe-35.5Ni-7.5Cr DURING NEUTRON IRRADIATION

F. A. Garner and J. M. McCarthy (Hanford Engineering Development Laboratory)

1.0 Objective

The object of this effort is to determine the nature of the mechanisms by which alloys decompose during irradiation.

2.0 Summary

Compositional micro-oscillations which form in Fe-35.5Ni-7.5Cr during neutron irradiation at 593°C are stable during thermal annealing at 600°C for 24 hours. For all practical purposes it does not matter whether the oscillations represent a srable or metastable state, since they cannot be relaxed easily by the limited thermal diffusion available at the temperatures of their formation.

3.0 Program

Title: Irradiation Effects Analysis
Principal Investigator: D. G. Doran
Affiliation: Hanford Engineering Development Laboratory

4.0 Relevant OAFS Program Plan Task/Subtask

Subtask II.C.1. Effect of Material Parameters on Microstructure

5.0 Accomplishments and Status

5.1 Introduction

The micro-oscillations in composition that develop during irradiation of Invar alloys are known to have consequences on void swelling and mechanical properties.[1-3] The mechanisms by which these oscillations develop has not yet been established, however.

The first requirement is to determine whether this phenomenon is merely an irradiation-accelerated version of a naturally occurring but sluggish process or whether radiation-produced point defects are necessary for the continued maintenance of the oscillations. The first of several experiments described earlier[4] which attempt to address this question is now complete.

A TEM specimen of Fe-35.5Ni-7.5Cr irradiated in ESR-II to 38 dpa at 593°C was annealed in vacuum at 600°C for 24 hours. This time was chosen to simulate a typical reactor down-time, addressing the question of whether the oscillations are unstable enough to dissolve during periods of reduced neutron flux or whether they are "frozen-in" due to the low level of diffusion at 600°C. The specimen was then rethinned to avoid potential surface effects on microsegregation and its relaxation upon annealing. This specimen had been examined prior to annealing and shown to have developed substantial oscillations in composition.[1,2,4]

5.2 Results

After annealing the specimen was reexamined using the EDX techniques employed in earlier studies. As shown in Figure 1, the oscillations are preserved after annealing. The compositional profiles shown in Figure 1 are quite similar to those of the pre-annealing examination, as shown in Figures 2 and 3.

5.3 Discussion

One may question whether 24 hours is a sufficient annealing time by which to judge the stability or metastability of the oscillations. If we estimate the relaxation time by solving the equation $x^2 = 2Dt$ assuming $x = 500$ nm[14] and the diffusivity $D \sim 10^{-18}$ $cm^2 sec^{-1}$[5] at 600°C we find that $t = 1.2 \times 10^9$ sec = 3.3×10^5 hours. This means that we would not expect to have relaxed the compositional profiles very much in 24 hours.

We now face a dilemma; to answer the question about the stability at 600°C we must anneal for at least 10^5 hours or we must raise the temperature of the anneal to 750-800°C. If a miscibility gap exists as suggested by Tanji and coworkers[6] we will exceed it at some temperature and thus not be addressing the question of stability at 600°C. Since the wavelength of the decomposition process appears to be sensitive to temperature, we also may not be able to distinguish between relaxation to the new longer wavelength or partial dissolution of the oscillations.

We can partially solve the dilemma by redefining the question. Is the micro-oscillation development a natural but accelerated consequence of an inherent tendency toward segregation, an unstable state maintained by irradiation or a radiation-produced unstable state that for all practical purposes is stable due to the low diffusion coefficient inherent in the absence of radiation? While we can now dismiss the second possibility, the first and latter choices are still possibilities allowed by the results of this experiment. Other studies now in progress are designed to address this question further.

5.4 Conclusions

Micro-oscillations developed in Fe-35.5Ni-7.5Cr during neutron irradiation at 600°C cannot be relaxed by annealing at 600°C for 24 hours. For all practical purposes it does not matter whether the oscillations represent a stable or unstable state, since they cannot be relaxed easily by the limited thermal diffusion available at the temperatures of their formation. The time required to form these oscillations has been determined by other studies to be on the order of thousands of hours and the developing oscillations are most likely "frozen-in" during periods of thermal annealing during reactor outages.

6.0 References

1. H. R. Brager and F. A. Garner in Optimizing Materials for Nuclear Applications, F. A. Garner, D. S. Gelles and F. W. Wiffen, (Eds.), TMS-AIME, Warrendale, PA (1985) pp. 141-166.

2. F. A. Garner, H. R. Brager, R. A. Dodd and T. Lauritzen, Nuclear Instruments and Methods in Physics Research, to be published, also HEDL-SA-3280.

3. H. R. Brager, F. A. Garner and M. L. Hamilton, J. Nucl. Mater., 133 & 134 (1985) p. 594.

4. F. A. Garner and H. R. Brager in OAFS Quarterly Progress Report DOE/ER-0046/24, February 1986, pp. 71-76.

5. S. J. Rothman, L. J. Nowicki and G. E. Murch, J. of Physics F, 10 (1980) pp. 383-398.

6. Y. Tanji, Y. Nakagawa, Y. Saito, K. Nishimura and K. Nakatsuka, Physica Status Solidi A, 56 (1979) pp. 513-519.

7.0 Future Work

EDX and annealing experiments will continue on Fe-35Ni and Fe-45Ni binary alloys irradiated at 420, 520 and 600°C in FFTF.

8.0 Publications

None.

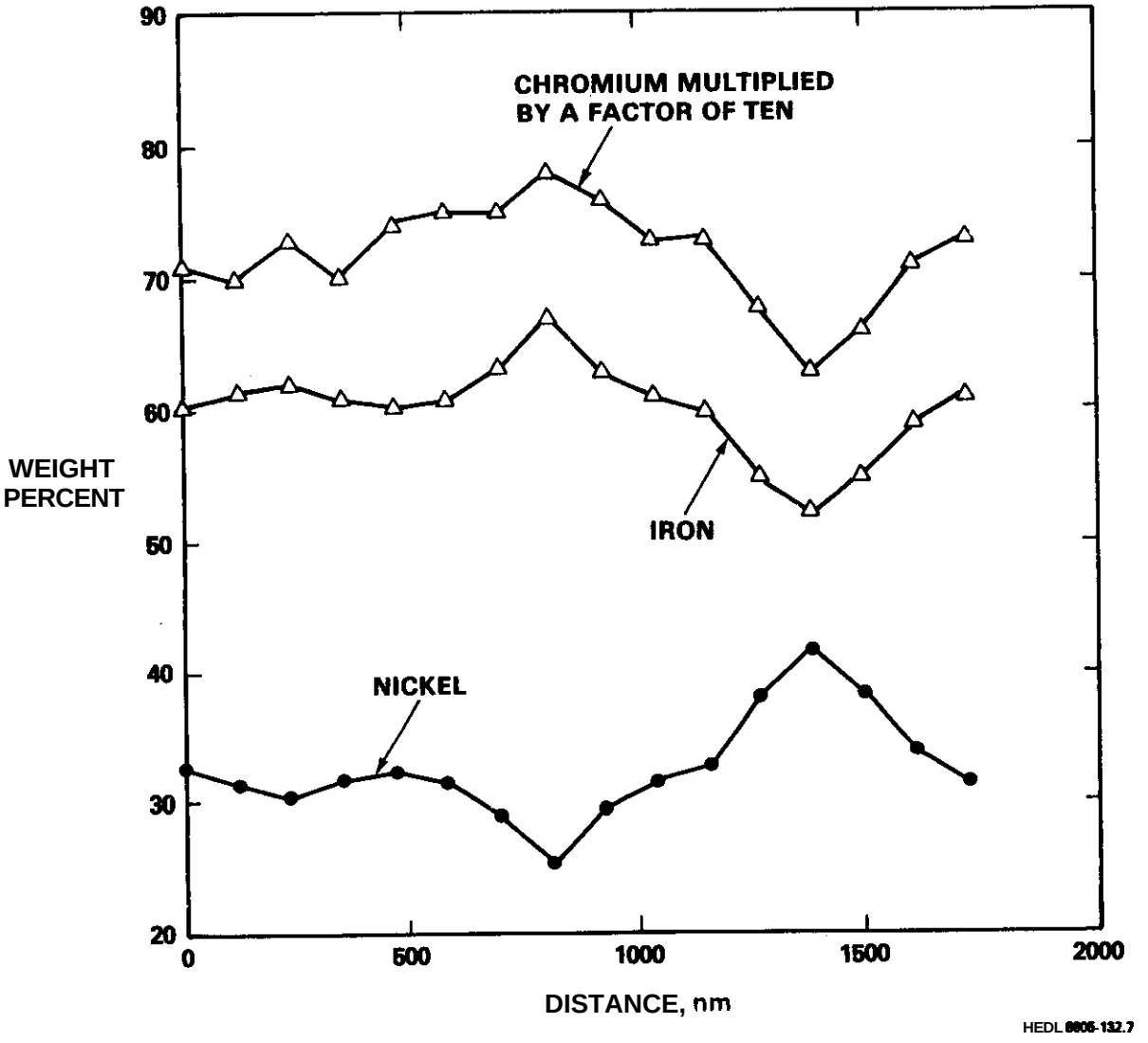

FIGURE 1. Random direction compositional trace taken after annealing of Fe-35.5Ni-7.5Cr at 600°C for 24 hours.

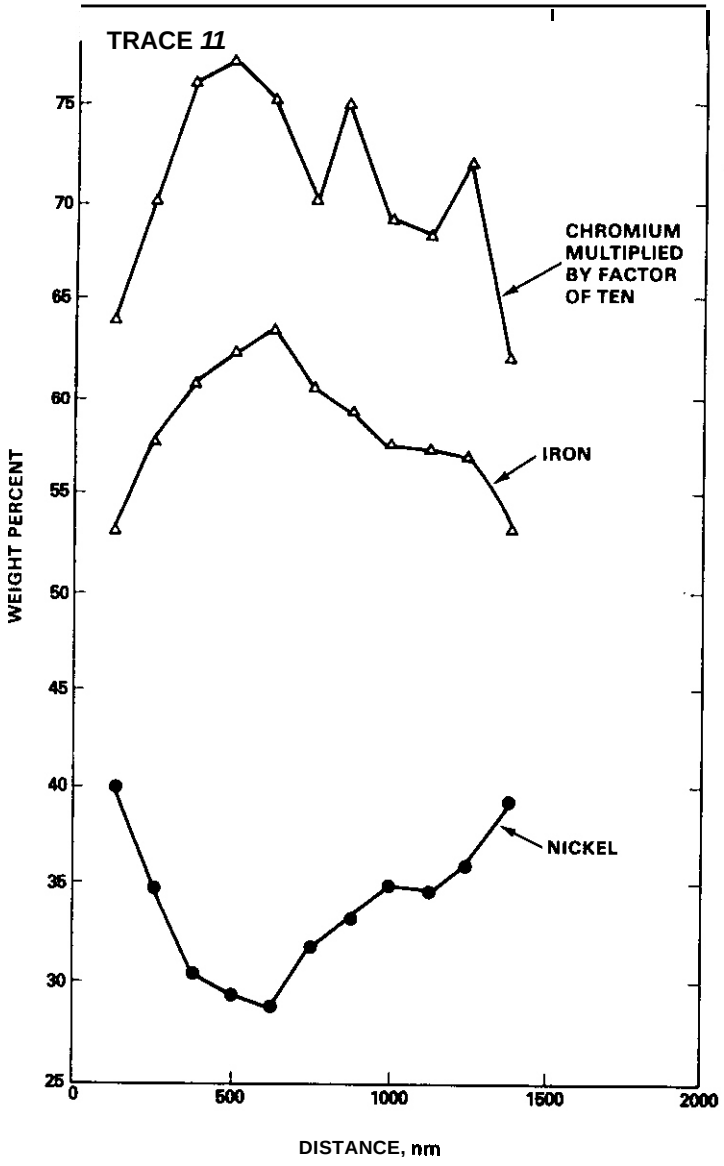

FIGURE 2. Compositional trace along <100> direction in the pre-annealed condition.

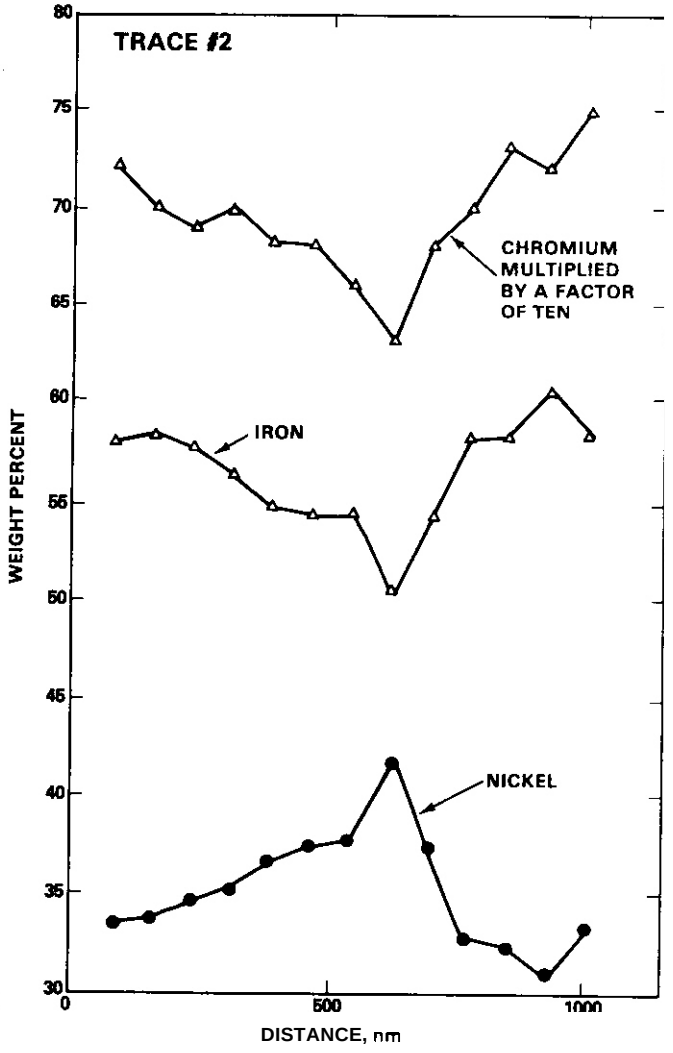

FIGURE 3. Another compositional trace in the pre-annealed condition.

CHAPTER 6

FUNDAMENTAL STUDIES OF SPECIAL PURPOSE MATERIALS

SWELLING OF COPPER-ALUMINUM AND COPPER-NICKEL ALLOYS IN FFTF-MOTA AT 450°C

F. A. Garner and H. R. Brager (Hanford Engineering Oevelopment Laboratory)

1.0 Objective

The object of this effort is to provide data on the response of copper alloys to neutron irradiation in order to determine damage mechanisms and to provide model-based predictions of the behavior of copper alloys in fusion environments.

2.0 *Summary*

Pure copper appears to swell with an S-shaped behavior at 450°C, tending to saturate at higher fluence levels. The addition of solutes such as aluminum and nickel at 5 weight percent leads to an extended transient regime and thereby a reduction in swelling at low to moderate fast neutron exposures. The addition of these elements also leads to an increase in the saturation level of swelling, however, resulting in an increase in swelling relative to that of pure copper at high fluence.

3.0

Title: Irradiation Effects Analysis (AKJ)
Principal Investigator: D. G. Doran
Affiliation: Hanford Engineering Development Laboratory

4.0 Relevant DAFS Program Plan Task/Subtask

Subtask II.C.l. Effects of Material Parameters on Microstructure

5.0 Accomplishments and Status

5.1 Introduction

In an earlier report the swelling at ~450°C was described for various copper alloys during neutron irradiation in FFTF-MOTA.(1) As shown in Figure 1 the higher swelling alloys often exhibit an S-shaped behavior with accumulating fluence. Also included in the same irradiation experiment were Cu-5Al and Cu-5Ni (weight percent). Density change data are now becoming available for these two alloys as part of a fundamental study of the compositional dependence of swelling during neutron irradiation.

5.2 Results

The density change data for these alloys are incomplete at present (see Table I) but are sufficient to demonstrate the major impact of nickel and aluminum on swelling. Note that at the higher fluences there are often 2 or 3 separate specimens, providing some idea of the variability of swelling.

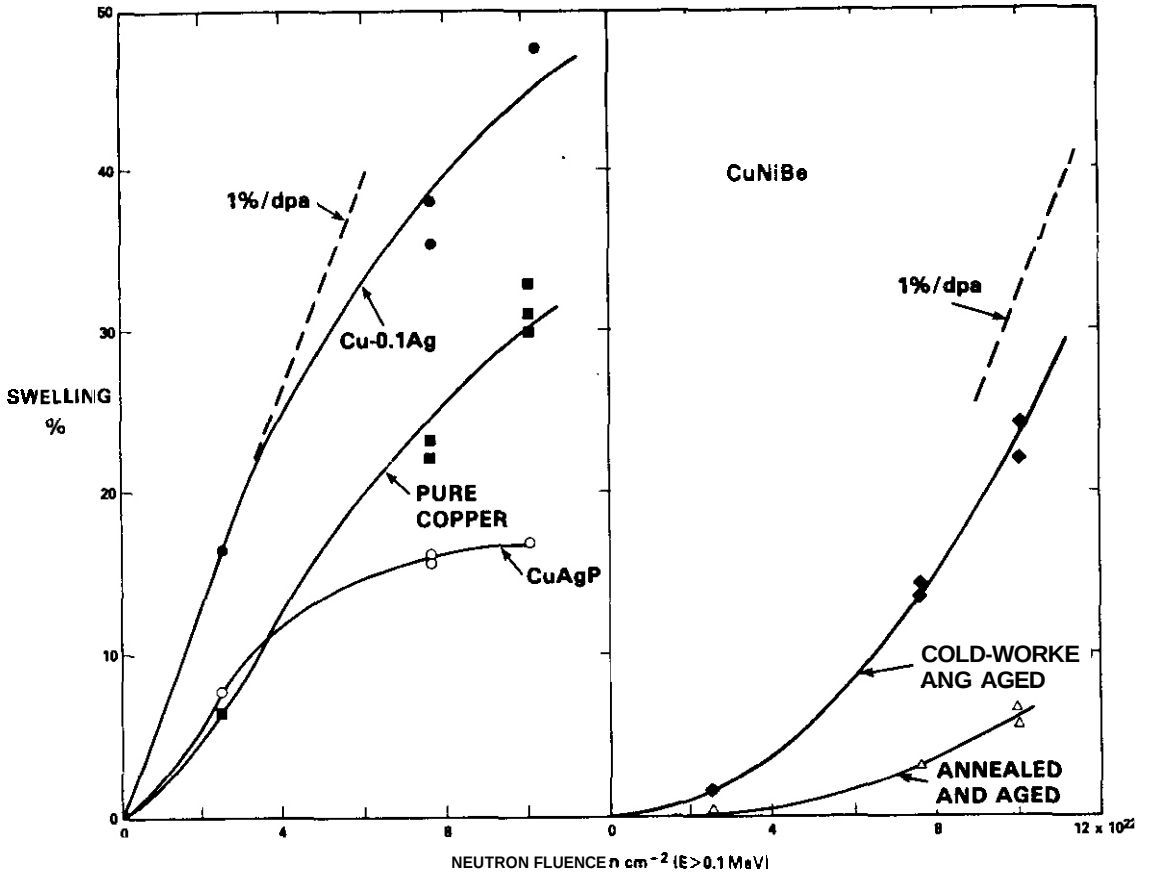

FIGURE 1. Swelling observed in pure copper and several copper-base alloys after irradiation in FFTF-MOTA at ~450°C. The data at 16.2 dpa were derived from miniature tensile specimens, those at higher fluence were derived from TEM disks.

TABLE 1

Percent Swelling of Annealed Copper Alloys at ~450°C in FFTF

	16.2 dpa	47.2 dpa	63.3 dpa
Cu (MARZ)	6.5	23.3. 22.2	31.3, 30.1, 33.2
Cu-5 Ni	2.15	--	27.7, 31.8
Cu-5Al	--	--	46.8, 45.8, 39.4

These data are plotted in Figure 2. Whereas Cu-5Ni clearly exhibits a delay in swelling prior to the onset of accelerated swelling, the lack of low fluence data on Cu-5Al do not allow the unqualified assumption of delayed swelling. In both cases, however, the swelling at 63.3 dpa is comparable to or greater than that of pure copper. It also appears that the saturation level of both alloys will be greater than that of pure copper.

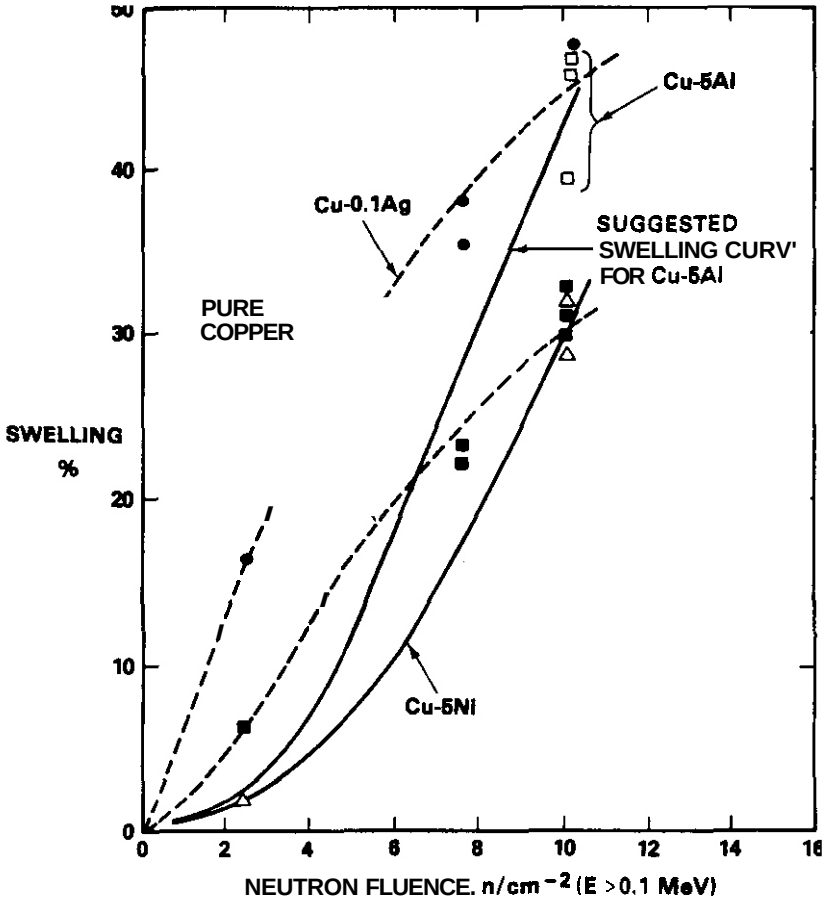

FIGURE 2. Comparison of Swelling of Cu-5Al and Cu-5Ni with that of Pure Copper and Cu-0.1Ag.

5.3 Discussion

Brimhall and Kissinger[2] have shown that addition of either 2 or *20* atomic percent nickel suppresses void swelling in copper after neutron irradiation at 285°C to 0.01 dpa. The addition of nickel to copper also suppresses void formation during electron irradiation[3-8] and ion irradiation.[9-10] Aluminum additions (1-7 atomic percent) have also been shown to lead to reductions in swelling of copper during neutron irradiation in the range 250-350°C.[11,12] Eased on these observations, it appears reasonable to assume that a delay of swelling will occur at 450°C, as shown in Figure 2. A similar delay of swelling is shown for Cu-1.8Ni-0.3Be (weight percent) in Figure lb.

5.4 Conclusions

The addition of elements such as Ni, Al and Be can delay the onset of swelling in copper, but at higher fluences this may lead to an increased amount of swelling relative to that of pure copper.

6.0 References

1. F. A. Garner and H. R. Erager, "Swelling of Pure Copper and Copper Alloys After High Fluence Irradiation in FFTF at ~450°C, DAFS Quarterly Progress Report DOE/ER-0046/24, February 1986, pp. 89-93.

2. J. L. Brimhall and H. E. Kissinger, Radiation Effects 15 (1972) 259-272.

3. M. J. Makin in Voids Formed by Irradiation of Reactor Materials, S. F. Pugh (Ed.), British Nuclear Engineering Society (1971) pp. 269-274.

4. T. Takeyama in New Trends in Electron Microscopy in Atom Resolution, Materials Science and Biology, H. Hashimoto et al. (Eds.), Dalien, China (July 1981), Science Press, Beijing, China (1982) pp. 78-86.

5. P. Barlow, "Radiation Damage in Pure FCC Metals and Alloys in HVEM," Ph. D. Thesis, University of Sussex, England, 1977.

6. T. Leffers, E. N. Singh, and P. Barlow, Risø-M-1937, Research Establishment Risø, Roskilde, Denmark, May 1977.

7. P. Barlow, T. Leffers and B. N. Singh, Risø-M-2129, Research Establishment Risø, Roskilde, Denmark, August 1978.

8. B. N. Singh, T. Leffers and P. Barlow in Proc. Fifth International Conference on High Voltage Electron Microscopy, Kyoto, Japan, August 29 - September 1, 1977, pp. 581-584.

9. D. J. Mazey and F. Menzinger, J. Nucl. Mater. 48 (1973) pp. 15-20.

10. K-H Leister, "Influence of Solutes on Heavy Ion Induced Void Swelling in Binary Copper alloys," Ph.D., Thesis, Kernforschungszentrum Karlsruhe, (May 1983) KFK Report 3499.

11. Y. Adda, in Radiation-Induced Voids in Metals, J. W. Corbett and L. C. Ianiello (Eds.), AEC Symposium Series No. 26 (1972) pp. 31-81.

12. M. Labbe and J. P. Poirier, J. Nucl. Mater., 46 (1973) pp. 86-98.

7.0 Future Work

Density change measurements on Cu-5Ni and Cu-5Al will continue. Data at 100 dpa will be available later in CY1986.

8.0 Publications

None.

THE EFFECTS OF LOW DOSES OF 14 MeV NEUTRONS ON THE TENSILE PROPERTIES OF VARIOUS COMMERCIAL COPPER ALLOYS

H. L. Heinisch and C. Martinez (Hanford Engineering Development Laboratory)

1.0 Objective

The objective of this experiment is to determine the effect of 14 MeV neutrons on radiation-induced changes in mechanical properties of representative commercial copper alloys, and to compare the effects of 14 MeV and fission reactor neutrons.

2.0 *Summary*

Miniature tensile specimens of high purity copper and five copper alloys were irradiated with D-T fusion neutrons in the RTNS-II to fluences up to 2.5 x 10^{18} n/cm^2 at 90°C and 290°C. The series of alloys includes solution-strengthened, precipitate strengthened and dispersion strengthened alloys. TO compare fission and fusion neutron effects, some of the alloys were also irradiated at the same temperatures to similar damage levels in the Omega West Reactor. Tensile tests were performed at room temperature, and the radiation-induced changes in tensile properties are examined as functions of fluence and displacements per atom (dpa). All the alloys sustain less irradiation-induced strengthening than pure copper. In contrast to pure copper, the effects of fission and fusion neutrons on the yield stress changes in the copper alloys correlate well on the basis of dpa.

3.0

Title: Irradiation Effects Analysis
Principal Investigator: 0. G. Doran
Affiliation: Westinghouse Hanford Company

4.0 Relevant DAFS Program Plan Task/Subtask

Subtask II.8.3.2 Experimental Characterization of Primary Damage State; Studies of Metals
Subtask II.C.6.3 Effects of Damage Rate and Cascade Structure on Microstructure; Low-Energy/High Energy Neutron Correlations
Subtask II.C.16.1 14-MeV Neutron Damage Correlation

5.0 Accomplishments and Status

5.1 Introduction

Copper alloys are being considered for service in fusion reactors, especially in magnet and high heat flux applications. Over the years many studies of irradiation effects in copper and copper alloys have been done, most oriented toward understanding some fundamental aspects of irradiation effects. Interest in copper alloys as potential fusion reactor materials has spurred interest in further experiments; some of which are discussed in a recent review [1].

The objectives of the present experiment are to determine the effects of D-T fusion neutrons on the tensile properties of some commercial copper alloys and to investigate the correlation of low dose fusion and fission neutron effects. The alloys tested here are some of the same alloys being irradiated to high fluences in the Fast Flux Test Facility [2]. In pure copper it has been found[3] that displacements per atom (dpa) is not an effective correlation parameter for low dose fission and fusion effects on tensile properties. We are interested to see if this extends to the commercial copper alloys as well.

5.2 Irradiations

Flat miniature tensile specimens were irradiated at the Rotating Target Neutron Source (RTNS-II) at Lawrence Livermore National Laboratory, currently the highest source of D-T fusion neutrons available. Irradiation temperatures were 90°C and 290°C, and the copper specimens were exposed to neutron fluences up to 2.5 x 10^{18} n/cm^2. Companion irradiations to similar damage levels were performed at 90°C and 290°C to four fluences from 5.2 x 10^{18} to 1.3 x 10^{20} total n/cm^2 in the Omega West Reactor (OWR) at Los Alamos National Laboratory. Damage rates are a minimum of 30 times higher in OWR than in the highest fluence RTNS-II copper alloy specimens. Tensile tests were performed on the specimens at room temperature. The specimens were included in irradiations for the Low Exposure Spectral Effects Experiment, described elswhere in the proceedings of this conference [3]. Details of the RTNS-II and OWR irradiations and the tensile testing are contained in that paper.

The materials consist of Marz-grade copper and five commercial copper alloys listed in Table 1. As indicated in the table, the materials represent several categories of alloys, including solution-strengthened, precipitation-strengthened, and dispersion-strengthened alloys.

TABLE 1

COPPER ALLOYS

Alloy	Composition (wt%)	Condition
Cu(MARZ)	Cu (99.999%)	annealed (15 m at 450°C)
Solution-strengthened		
CuAgP	Cu -0.3 Ag -0.06 P -0.08 Mg	20% CW and aged (1 h at 427°C)
Precipitation-strengthened		
CuNiBe (½HT)	Cu -1.8 Ni -0.3 Be	20% CW and aged (3 h at 480°C)
CuBeNi (AT)	Cu -1.8 Ni -0.3 Be	annealed (15 m at 955°C) and aged (3 h at 480°C)
MZC	Cu -0.9 Cr -0.1 Zr -0.05 Mg	90% CW and aged (30 m at 475°C)
Dispersion-strengthened		
Cu-A125	Cu -0.25 Al [as Al_2O_3]	annealed (1 h at 982°C)

5.3 Results

Figure 1 shows the 0.2% offset yield stress as a function of D-T fusion neutron fluence for copper and the copper alloys. A curve linear in the fourth root of the fluence is fitted to the pure copper data. For the alloys the lines were drawn simply to show the trends in the data. Figure 1 illustrates the large range in strengths of the materials considered in this study. Because of the range of values in this figure, the amount of irradiation hardening appears small, even for annealed copper. The copper, however, increases in yield strength by a factor of three in this fluence range.

In Fig 2 the yield stress is plotted as a function of fluence for RTNS-II irradiations at 290°C. There is little strengthening of pure copper in this fluence range. Only Cu8eNi(AT) shows a modest increase in yield stress with fluence, while the other alloys either remain relatively unaffected or they soften.

In Figs 3 and 4 the irradiation-induced change in yield stress is shown as a function of neutron fluence for the copper alloys in comparison to pure copper. The data and fitted curve for pure copper are plotted for reference in both figures. The irradiation-induced changes in yield stress of the high strength alloys are small differences of large numbers, with maximum changes in this fluence range being as little as 15% of the absolute yield stress (for the CuBeNi alloys). Uncertainties in the measurement of yield stress are a percentage of the yield stress value. Hence, the larger the yield stress, the greater the absolute uncertainty in the determination of the change in yield stress. This is indicated by error bars on selected points in Figs 3 and 4 representing an uncertainty of 25% in the absolute yield stress measurement.

Although uncertainties are large in the data for the precipitation strengthened alloys, Fig 3, there are systematic differences between them and the data for pure copper that imply a difference in behavior. MZC clearly sustains less irradiation-induced strengthening than pure capper at these fluences. The yield stress changes in the alloys appear to have about the same fluence dependence as pure copper, but shifted to higher fluences for the same amount of change.

The solution-strengthened alloy CuAgP, Fig 4, initially undergoes less strengthening than pure copper. but it appears to strengthen at a faster rate. The dispersion-strengthened alloy CuAl25 also shows less change than pure copper.

The load-displacement curves generated during the tests on pure copper differ qualitatively with increasing neutron fluence. For specimens irradiated at 90°C in RTNS-II the total elongation decreases as the yield stress increases. At the highest fluence the elongation is about half of the unirradiated value. In addition, for fluences above about 4×10^{17} n/cm^2 in RTNS-II at 90°C the curves display a yield point phenomenon. The elongation of the OWR-irradiated specimens is also less (by a half to a third) than for unirradiated specimens, but there is considerable scatter. Yield points also occur, but at fluences where the irradiation strengthening is comparable to that in the RTNS-II specimens that display yield points. That is, in pure copper the appearance of yield points corresponds to a minimum level of irradiation strengthening, independent of the spectrum. At 290°C there were no yield points and little change in total elongation in either spectrum.

For the alloys the load-displacement curves show no yield points at either temperature or in either spectrum. In the alloys the amounts of elongation are much less than in pure copper, and the elongation tends to decrease with increasing fluence. Elongations will be discussed quantitatively in a future report.

Three of the copper alloys, CuBeNi(AT), MZC, and CuAl25 were also irradiated in OWR along with pure copper. Figure 5 shows the change in yield stress as a function of OWR total neutron fluence at 90°C for these materials. As with the D-T fusion neutrons. the MZC and CuAl25 show significantly less strengthening than pure copper in the fission reactor irradiations. The CuBeNi(AT), on the other hand, responded about the same as copper in the fission spectrum.

In Figs 6-9 the irradiation effects on the yield stress of pure copper and the alloys irradiated in RTNS-II and OWR are compared. The changes in yield stress are plotted as a functon of displacements per atom (dpa). The dpa values were determined using spectral-averaged displacement crass sections obtained with the NJOY nuclear data code[4]. Cross sections for pure copper were used in all cases; the values are 293 b and 3699 b for OWR and RTNS-II, respectively. Error bars in the figures denote an estimated uncertainty of 25% in the absolute yield stress measurements. In pure copper, Fig. 6, three times as many dpa are needed in OWR to produce the same yield stress change as in RTNS-II. However, in all three alloys, CuBeNi(AT), CuAl25, and MZC, the effects of fission and fusion neutrons on the yield stress correlate well on the basis of dpa in the fluence regions where the data overlap.

5.4 Discussion and Conclusions

In RTNS-II and OWR at 90°C and 290°C the radiation-induced changes in 0.2% offset yield stress in the copper alloys are less than those in pure copper irradiated to the same fluence. The decreased irradiation strengthening in the alloys is probably a result of the increased concentration of defect sinks in the alloys. Even at 90°C, point defects in copper are considerably mobile and would tend to interact with the existing sinks at the expense of forming additional clusters. One should expect to see the same phenomenon in cold-worked pure copper. It is also possible that less strengthening occurs because of cascade-induced dissolution of precipitates, although this effect may be quite small at such low fluences. Examination of the microstructures may reveal information pertinent to this phenomenon.

The irradiations at 290°C had relatively little effect on the pure copper or the alloys. Some softening occurred, most dramatically in the cold worked alloys, CuBeNi(1/2HT) and CuAgP. At 290°C the effects of temperature evidently dominate over irradiation effects. For pure copper 290°C is within the range of Stage V recovery temperatures in annealing experiments[5], during which the operant mechanism is dissolution of vacancy clusters. In the RTNS-II all specimens were held at temperature ostensibly only while the neutron source was operating, which was about 2900 hours (ideally in 120 h. shifts) spread over about 7 months. In practice, there were several times as long as an hour when the beam was off while the furnace was at temperature. In OWR, where fluences are determined by time rather than position, the highest fluence run was done for 200 hours in 5 eight hour shifts per week. The In-core Reactor Furnace takes about 15 min to heat up and cool down at the beginning and end of each shift.

Unlike in pure copper, the yield stress changes in the copper alloys for fission and fusion neutron irradiations can be correlated well on the basis of dpa. No clear evidence was found for the existence of additional spectral effects.

5.9 Acknowledgments

The authors gratefully acknowledge the contributions of many others who aided in the performance of this experiment, In particular we are indebted to J. S. Pintler and M. D. Jones for performing tensile tests, and to the staffs of the RTNS-II and the OWR for their enthusiastic and able assistance in performing the irradiations. The RTNS-II irradiations were performed under the US-Japan Collaborative Program for Operation and Utilization of the RTNS-II. This work was sponsored by the USDOE, Office of Energy Research, Office of Fusion Energy, under Contract No. DE-AC06-76FF02170.

6.0 References

1. S. J. Zinkle and R. W. Knoll, "A Literature Review of Radiation Damage data for Copper and Copper Alloys," University of Wisconsin Fusion Technoloyy Institute Report UWFDM-578, June 1984.

2. H. R. Brager, H. L. Heinisch and F. A. Garner, J. Nucl. Mater. 133 & 134, 676 (1985).

3. H. L. Heinisch, S. O. Atkin and C. Martinez, Proceedings of the Second International Conference on Fusion Reactor Materials, Chicago, April 13-17, 1986.

4. R. E. MacFarlane, R. J. Barrett, D. W. Muir and R. B. Boccourt, The NJOY Nuclear Data Processing System, Vol I: User's Manual, LA-7584-M, Los Alamos National Laboratory (1978).

7.0 Publications

A report on this work will be presented at the Second International Conference on Fusion Reactor Materials in Chicago, April 13-17. *1986.*

8.0 Future Work

Tensile tests will be done on specimens now available from the 290°C irradiations in OWR and on specimens from the 200/450°C RTNS-II irradiation soon to be completed.

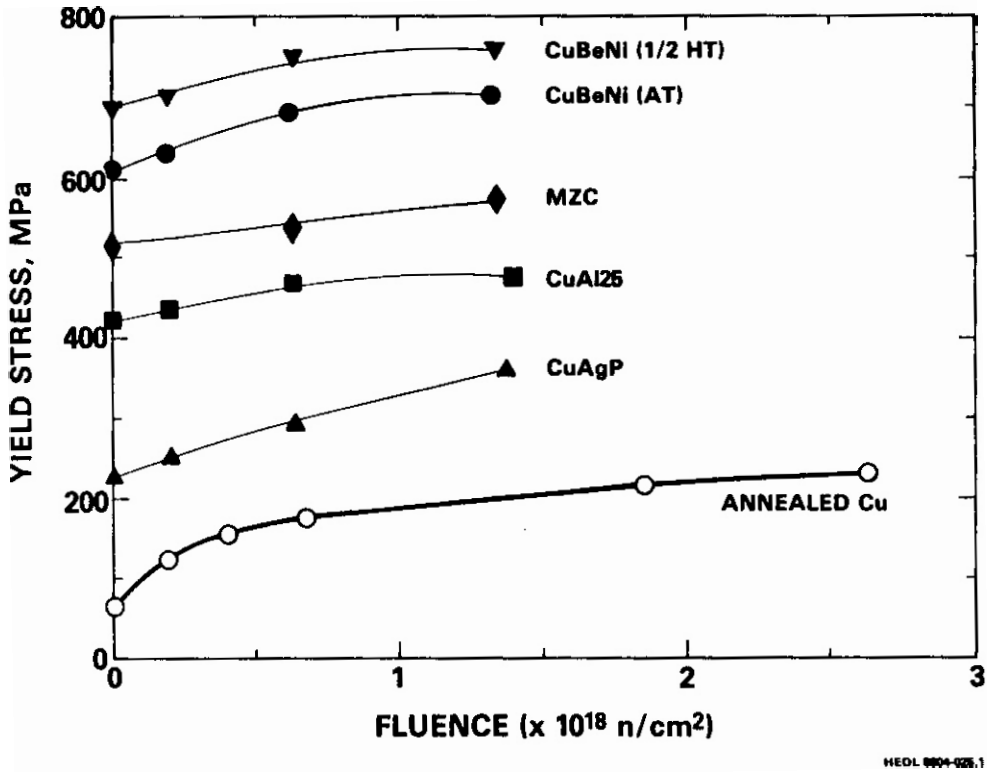

FIGURE 1. The 0.2% offset yield stress as a function of 14 MeV neutron fluence for high purity copper and commercial copper alloys irradiated at 90°C in RTNS-II.

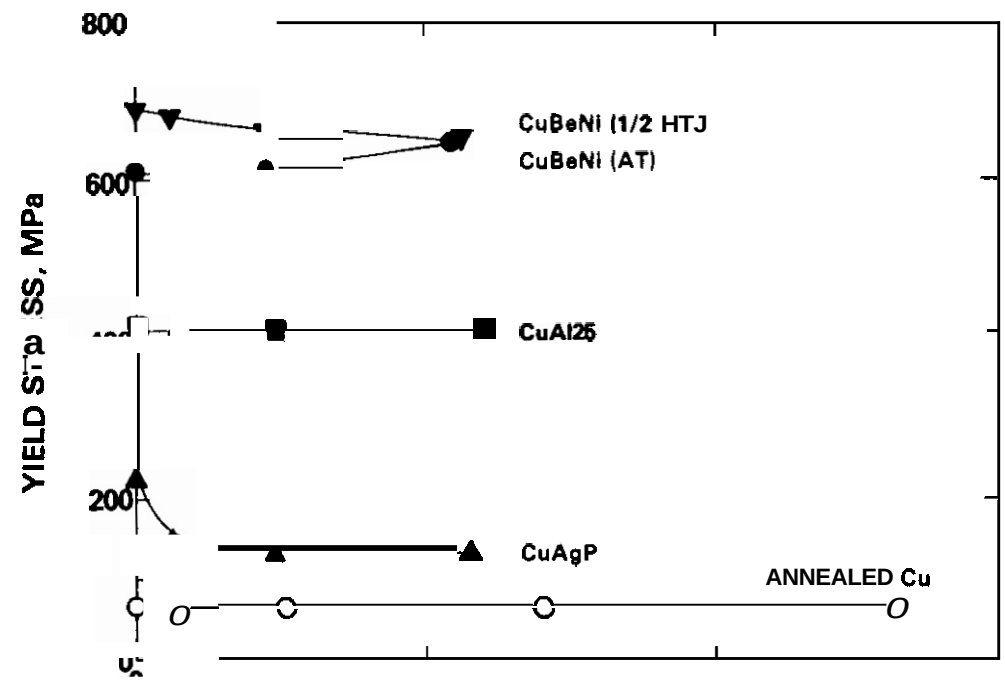

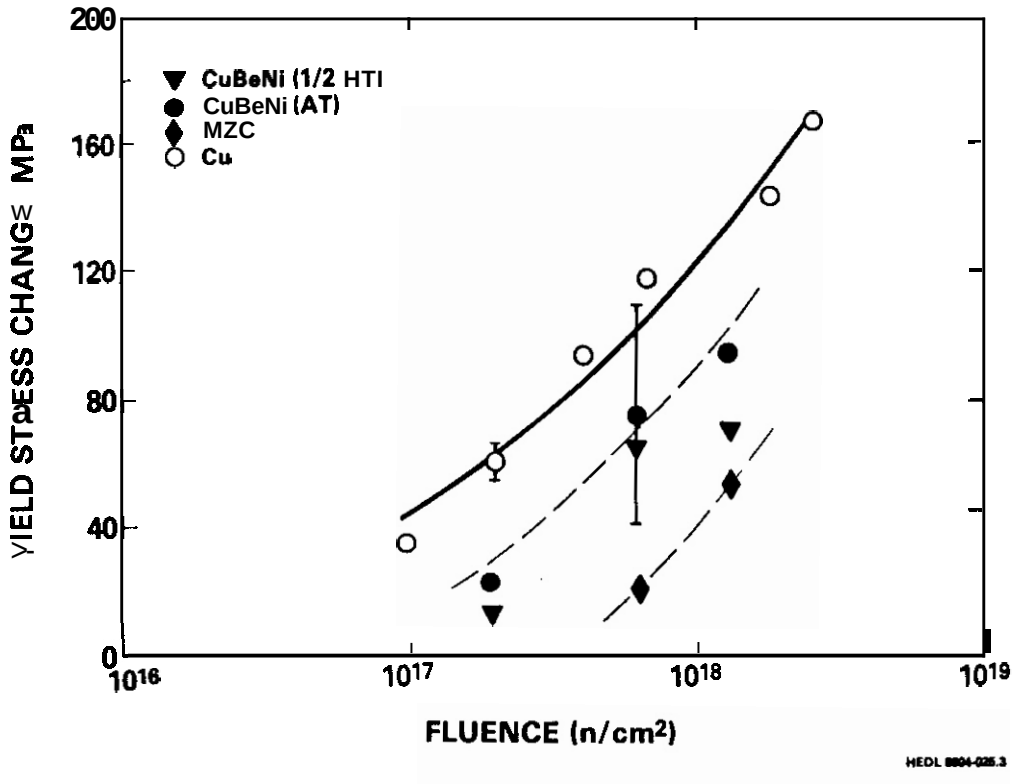

FIGURE 3. The change in yield stress as a function of 14 MeV neutron fluence for pure Cu, CuBeNi in two conditions, and MZC. The error bar represents an uncertainty of ±5% in the value of the absolute yield stress of CuBeNi (AT).

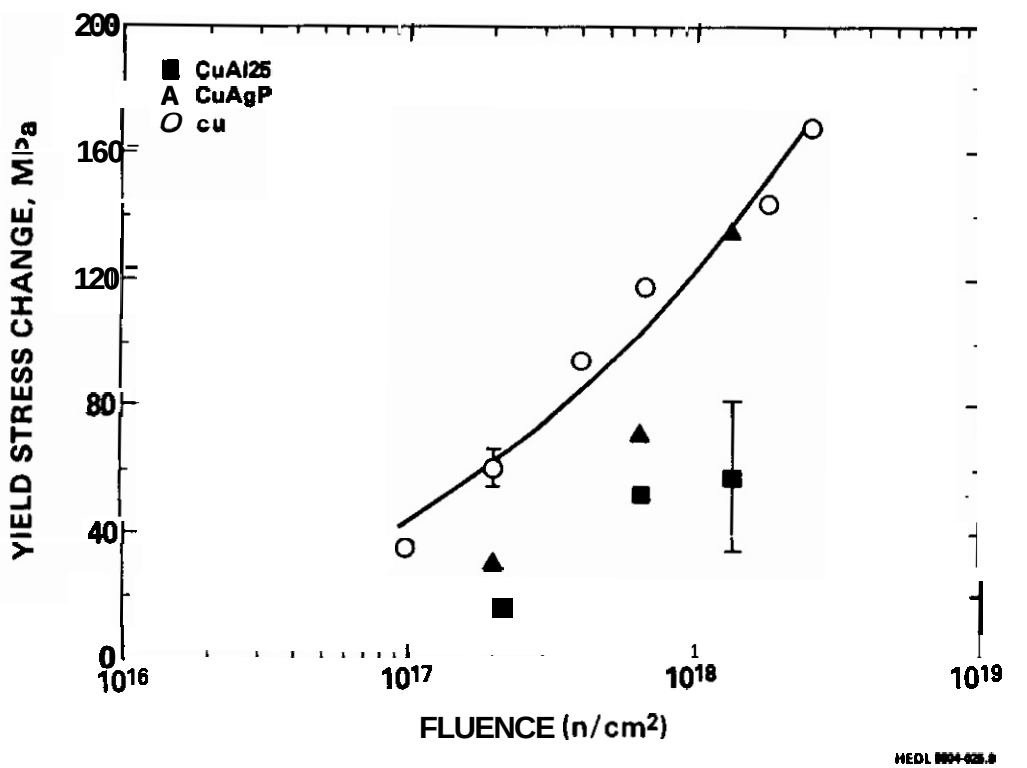

FIGURE 4. The change in yield stress as a function of 14 MeV neutron fluence for pure Cu, CuAgP, and CuAl25. The error bar represents an uncertainty of ±5% in the value of the absolute yield stress of CuAl25.

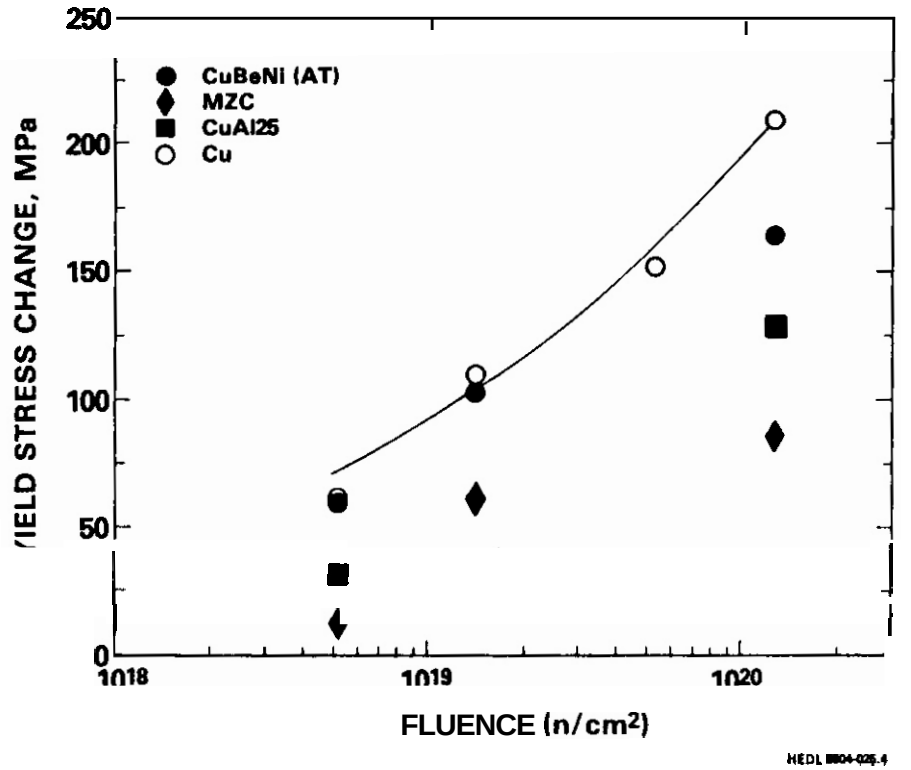

FIGURE 5. The change in yield stress as a function of total neutron fluence for pure copper and copper alloys irradiated in the Omega West Reactor at 90°C.

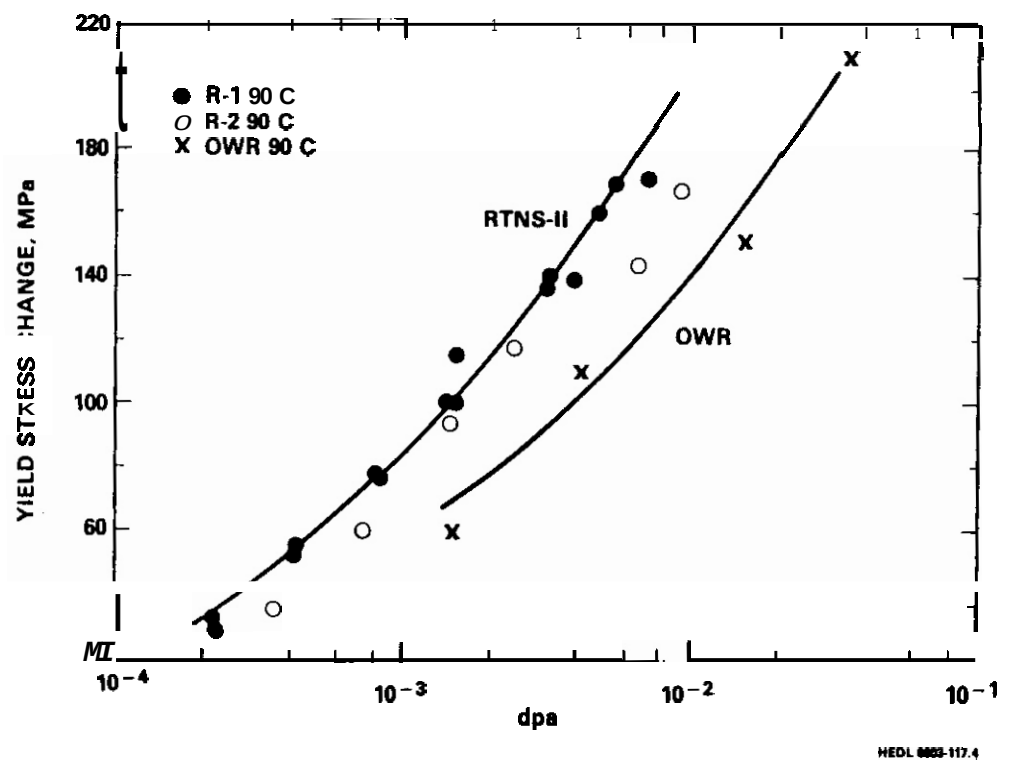

FIGURE 6. The change in yield stress as a function of dpa for annealed pure copper irradiated in RTNS-II and OWR at 90°C.

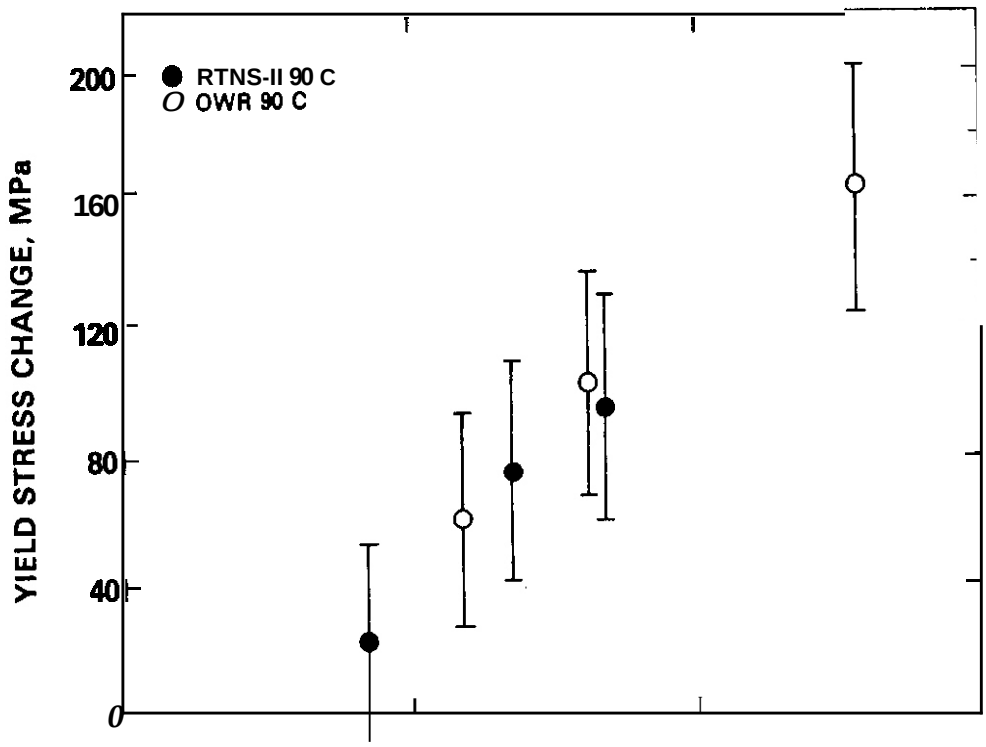

FIGURE 7. The change in yield stress as a function of dpa for CuBeNi (AT) irradiated at 90°C in RTNS-II and OWR.

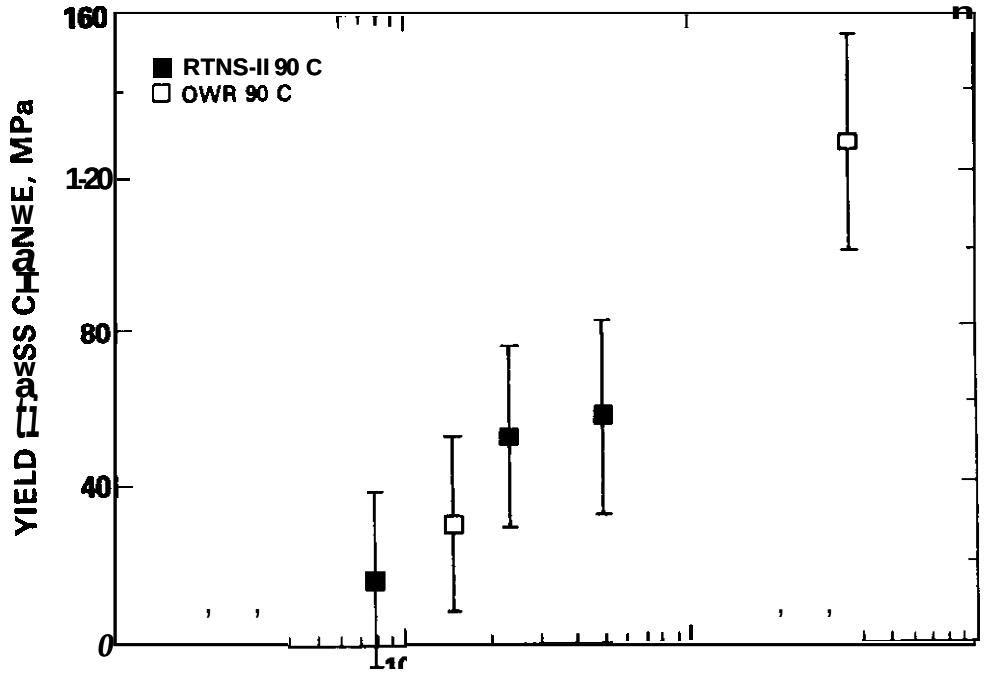

FIGURE 8. The change in yield stress as a function of dpa for alumina dispersion-strengthened copper (CuAl25) irradiated at 90°C in RTNS-II and OWR.

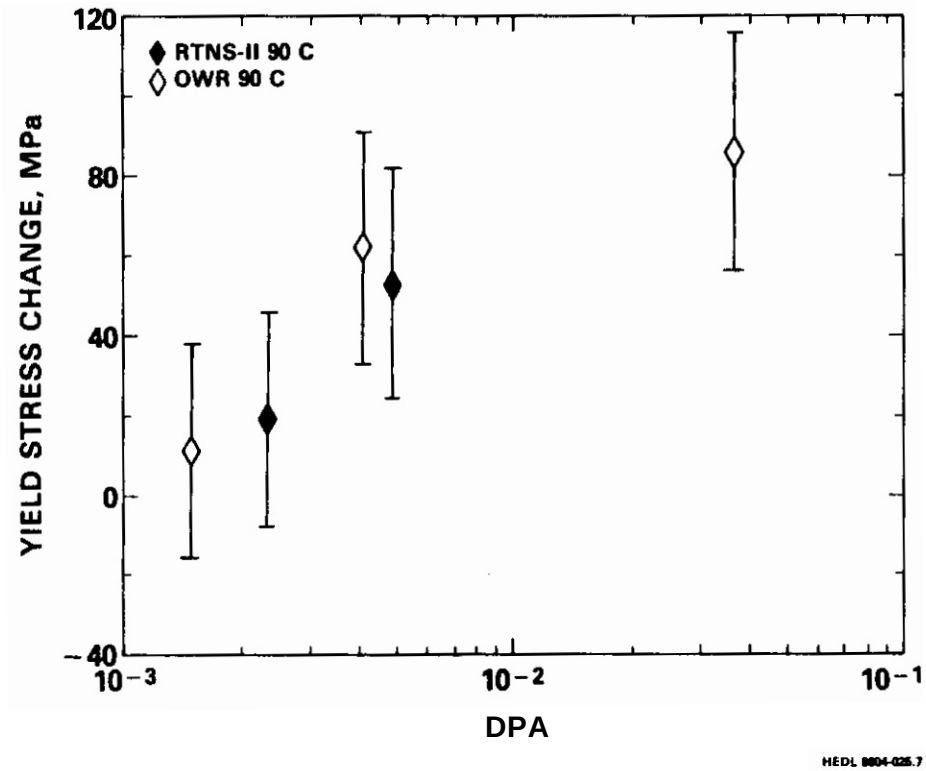

FIGURE 9. The change in yield stress as a function of dpa for MZC copper alloy irradiated at 90°C in RTNS-II and OWR.

EXTERNAL DISTRIBUTION

UC-20 (108), 20c (56)

DOE-HQ/Office of Fusion Energy
ER-62
Washington, DC 20545

SE Parket

DOE-HQ/Office of
International Security Affairs
DP-33, Mail Stop 4C-024
Washington, DC 20585

DW Dorn

Argonne National Laboratory (3)
9700 South Cass Avenue
Argonne, IL 60439

LR Greenwood, CMT-205
A. Taylor, MST-212
BA Loomis, MST-212

Argonne National Laboratory
EBR-II Division
Reactor Materials Section
P.O. Box 2528
Idaho Falls, ID 83403-2528

DL Porter

Battelle
Pacific Northwest Laboratory (2)
P.O. BOX 999
Richland, WA 99352

JL Brimhall 306W/210
TD Chikalla PSL/1277

Carnegie-Mellon University
Metallurgical Engineering
3325 Science Hall
Pittsburgh, PA 15213

WM Garrison Jr

Centre d'Etudes de Chimie Metallorgique
15, Rue Georges-Urbain
Yitry-sur-Seine
94400 Vitry, France

G. Martin

Columbia University
School of Engineering & Applied Science
New York, NY 10027

RA Gross

Commission of the European Communities
Kue de la Loi 200
B-1049 Bruxelles, Belgium

J. Darvas

Commission of the European Communities (2)
Joint Research Center
I-21020 Ispra, Varese, Italia

R. Dierckx, Physics Division
P. Schiller, Materials Science Division

Department of the Navy
Naval Research Laborator (2)
Washington

JA Sprague, Code 6395
LE Steele, Code 6330

Energieonderzoek Centrum Neaerland (2)
Netherlands Energy Research Foundation
Westerduinweg 3, Postbus 1
NL-1755 ZG, Petten (NH), The Netherlands

B. vanderSchaaf
W. vanWitzenburg, Materials Dept

GA Technologies Inc (3)
P.O. Box 85608
San Diego, CA 92138

JR Gilleland
GR Hopkins
T. Lechtenberg

General Dynamics/Convair
P.O. BOX 85377
San Diego, CA 92138

H. Gurol, MZ 92-1072

General Electric
Advanced Nuclear Technology Operation (2)
310 DeGuign Drive
Sunnyvale, CA 94088

ANTO Library, M/C F-02
S. Vaidyanathan, M/C 5-53

Hahn-Meitner Institut fur Kernforschung Berlin GmbH
Arbeitsgruppe C2
Glienickerstrasse 100
D-1000 Berlin 39, Federal Republic of Germany

H. Wollenberger

Hokkaido University (2)
Facility of Engineering
Kita-hu, Sapporo, 060 japan

Michio Kiritani, Precision Engineering
Taro Takeyama, Metals Research Institute

Institiit fiir Festkorperforschung der
Kernforschungsanlage Jiilich GmbH
Postfach 1913
D-5170 Jiilich 1, Federal Republic of Germany

P. Jung

EXTERNAL DISTRIBUTION (Cont'd)

Japan Atomic Energy Research Institute (2)
Physical Metallurgy Laboratory
Tokai Research Establishment
Tokai-mura, Naka-gun, Ibaraki-ken, 319-11 Japan

Tadao Iwata, Physics
Kensuke Shiraishi, Fuels Materials Research

Kernforschungszentrum Karlsruhe GmbH
Institüt fur Material und Festkorperforschung II
Postfach 3640
D-7500 Karlsruhe 1, Federal Republic of Germany

K. Ehrlich

Kyushu University
Research Institute for Applied Mechanics
6 Kasuga-Koen, Kasuga-shi
Fukuoka, 816 Japan

Kazunori Kitajima

Lawrence Livermore National Laboratory (2)
P.O. BOX 808
Livermore, CA 94550

MW Guinan, L-396
OW Heikkinen, L-397

Lawrence Livermore National Laboratory
P.O. Box 5511
Livermore, CA 94550

EC Dalder, L-643

Los Alamos National Laboratory
P.O. Box 1663
Los Alamos, NM 87544

DJ Dudziak, S-41F611

Massachusetts Institute of Technology (2)
77 Massachusetts Avenue
Cambridge, MA 02139

I-Wei Chen, 13-5118
NJ Grant, 8-407

Massachusetts Institute of Technology
Nuclear Reactor Laboratory
138 Albany St
Cambridge, MA 02139

OK Harling, NW12-204

Max-Planck-Institut fur Plasma Physik (2)
The NET Team, IPP/NET
D-8046 Garching bei München,
Federal Republic of Germany

DR Harries
R. Toschi

McDonnell-Douglas Astronautics Co
P.O. Box 516
St. Louis, MO 63166

JW Davis

Nagoya University
Institute of Plasma Phvsics
Furo-chyo, Chikusa-ku,
Nagoya, 464 Japan

Taijiro Uchida

National Research Institute for Metals
Tsukuba Laboratories
1-2-1 Sengen, Sakura-mura,
Nihari-qun, Ibaraki, 305 Japan

H. Shiraishi

North Carolina State University
Box 7907
Materials Engineering Department
Raleigh, NC 27695-7907

JR Beeler Jr

Oak Ridge National Laboratory (6)
P.O. Box X
Oak Ridge, TN 37831

ML Grossbeck NH Packan
LK Mansur RE Stoller
PJ Maziasz SJ Zinkle

Oak Ridge National Laboratory (2)
P.O. Box Y
Oak Ridge, TN 37831

LA Berry
MW Wiffen, FEDC Bldg

Osaka University
2-1 Yamada-oka., Suita,
Osaka, 565 Japan

Kenji Sumita, Nuclear Engineering

Osaka University
8-1 Mihogaoka
Ibaraki, Osaka, 567 Japan

Toichi Okada, Institute of
Scientific & Industrial Research

Pacific Sierra Research Corp
1048 Camino Del Mar
Del Mar, CA 92014

RD Stevenson

EXTERNAL DISTRIBUTION (Cont'd)

Princeton University (2)
Plasma Physics Laboratory
Forrestal Campus
P.O. Box 451
Princeton, NJ 08544

JPF Conrads
Long-poe Ku

Risø National Laboratory
Portfach 49
OK14000 Roskilde, Denmark

BN Singh

Rockwell International Corp
Rocketdyne Division
6633 Canoga Avenue
Canoga Park, CA 91304

DW Kneff, NA02

Sandia National Laboratories
Livermore, CA 94550

WG Wolfer

Science University of Tokyo
Faculty of Engineering
Kagurazaka, Shinjuku-ku,
Tokyo, 162 Japan

RR Hasiguti

Studiecentrum voor Kernenergie
Centre d'Etude de l'Energie Nucleaire
Boeretang 200
B-2400 Mol, Belgium

J. Nihoul

Swiss Federal Institute
for Reactor Research (2)
CH-5303 Würenlingen, Switzerland

WV Green
M. Victoria

Tohoku University (2)
Research Institute for Iron,
Steel and Other Metals
2-1-1 Katahira, Sendai, 980 Japan

Katunori Abe
Hideki Matsui

Tokyo Institute of Technology
Research Laboratory for Nuclear Reactors
12-1, 2-chome, O-Okayama
Meguro-ku, Tokyo, 152 Japan

Kazutaka Kawamura

United Kingdom Atomic Energy Authority
Atomic Energy Research Establishment (2)
Oxfordshire OX11 ORA, UK

R. Bullough, Theoretical Physics

United Kingdom Atomic Energy Authority
Culham Laboratory
Applied Physics & Technology Division
Abingdon, Oxfordshire OX14 3DB, UK

GJ Butterworth

University of California (2)
School of Engineering and Applied Science
Boelter Hall
Los Angeles, CA 90024

RW Conn, KL-98
NM Ghoniem, KH-01

University of Michigan
Nuclear Engineering
Ann Arbor, MI 48109

T. Kammash

University of Missouri
Dept of Nuclear Engineering
Rolla, MO 65401

A. Kumar

University of Tokyo (3)
3-1, Hongo 7-chome,
Bunkyo-ku, Tokyo, 113 Japan

Naohira Igata, Met & Materials Science
Shiori Ishino, Nuclear Engineering
Shuichi Iwata, Nuclear Engineering

University of Virginia
Dept of Materials Science
Thornton Hall
Charlottesville. VA 22901

WA Jesser

Westinahouse
Advanced Energy Systems Division
Fuels Materials Technology
P.O. Box 10864
Pittsburgh, PA 15236

A. Boltax, Manager

Westinghouse
Research and Development Center
1310 Beulah Road
Pittsburgh, PA 15235

JA Spitznagel

INTERNAL DISTRIBUTION

DOE-RL/AMF
Site & Laboratory Management Division (SMD)
Laboratory Manaqement & Technoloqy
Services Branch-
FED/513

KR Absher, Chief

HEDL (24)

HR Brager	W/A-58	FM Mann	W/A-58
LL Carter	W/B-47	WN McElroy	W/C-39
DG Doran (5)	W/A-57	RW Powell	W/A-58
FA Garner	W/A-58	RJ Puigh	W/A-58
DS Gelles	W/A-58	FA Schmittroth	W/A-58
R. Gold	W/C-39	WF Sheely	W/C-20
ML Hamilton	W/A-65	RL Simons	W/A-65
HL Heinisch	W/A-58	HH Yoshikawa/MJ Korenko	W/C-44
GD Johnson	W/A-65	Central Files	W/C-110
NE Kenny	W/C-115	Documentation Services	W/C-123